UNIVERSITY OF CAPE COAST

# *IN VIVO* TRANSIT DOSIMETRY WITH ELECTRONIC PORTAL IMAGING DEVICES (EPID) FOR EXTERNAL BEAM CANCER TREATMENTS

MARK POKOO-AIKINS

2019

University of Cape Coast

UNIVERSITY OF CAPE COAST

# *IN VIVO* TRANSIT DOSIMETRY WITH ELECTRONIC PORTAL IMAGING DEVICES (EPID) FOR EXTERNAL BEAM CANCER TREATMENTS

BY

MARK POKOO-AIKINS

Thesis submitted to the Department of Physics of the School of Physical Sciences, College of Agriculture and Natural Science, University of Cape Coast, in partial fulfillment of the requirements for the award of Doctor of Philosophy degree in Physics

JULY, 2019

# DECLARATION

**Candidate's Declaration**

I hereby declare that this thesis is the result of my own original research and that no part of it has been presented for another degree in this university or elsewhere.

Candidate's Signature:..... Date:.....

Name: Mark Pokoo-Aikins

**Supervisors' Declaration**

We hereby declare that the preparation and presentation of the thesis were supervised in accordance with the guidelines on supervision of thesis laid down by the University of Cape Coast.

Principal Supervisor's Signature:..... Date:.....

Name: Prof. Augustine Kwame Kyere

Co-Supervisor's Signature: ..... Date:.....

Name: Prof. Moses Jojo Eghan

## ABSTRACT

According to the Radiotherapy Risk Profile report by the World Health Organization (WHO), the major causes of severe radiotherapy incidents are due to human errors. The real danger is when the error in administration goes undetected during cancer treatments. This may lead to radiation damage to normal tissues, and may be lethal to the patient. The aim of this work was to develop a transit dosimetry calculation model using C++ and vb.net codes for verifying patient radiation doses using amorphous silicon electronic portal imaging devices (aSi EPID), which could be fast, simple and accurate to be employed in routine clinical work. The model was tested with heterogeneous phantom by comparing the calculations from the developed model with measurements from thermoluminescent dosimeters (TLDs). The transit dosimetry model developed in this study offers satisfying results for square defined fields in real-time treatment of a tissue–mimicking phantom (anthropomorphic phantom). A comparison of absorbed dose measurements between the developed model and TLDs indicate a maximum and a minimum deviations of 3.93% and 1.02% respectively. The calculated absorbed doses from the developed model was therefore in concurrence with TLD measurements within ±5%, and was within the prescribed International Atomic Energy Agency (IAEA) reference level. The model presented therefore satisfied the accuracy requirements for clinical use. The model may therefore be used for *in vivo* dosimetry of radiation therapy.

KEY WORDS

ASi EPID

Dose delivery

Dose verification

*In vivo* dosimetry

Radiotherapy

Transit dosimetry

ACKNOWLEDGEMENTS

I wish to thank my supervisors Prof. Augustine Kwame Kyere and Prof. Moses Jojo Eagan for their patience, ideas, support and belief in my work. I would also like to thank Dr. Samuel Nii Tagoe and Dr. Shirazu Issahaku for their help and constructive criticisms during all stages of my work. I am grateful to my parents for all the financial and logistical support given to me for my research works.

To my friends who proof-read my thesis write-up (Dr. Theresa Dery and Miss Abigail Kuntu-Blankson), I appreciate your help in the herculean task of correcting my grammar and atrocious bad spelling. I proudly claim all remaining mistakes as my very own.

I wish to offer special thanks to my fellow medical physicists, George Felix Acquah and Philip Oppong Kyeremeh, who shared the best and worst moments of my research work, weathered my despair, and gave unreservedly of their time and friendship.

All my many friends deserve my gratitude for their patience and understanding: I have not been the best of friends during the last one year.

Finally, I wish to express my sincere thanks to the Ghana Education Trust Fund (GETFund) for supporting me financially throughout my entire PhD programme. I am also grateful to my brother and sisters, who have shared a lifetime of exploration, and who will always be my greatest friends. If I never said it before, then I say thank you, I love you all.

DEDICATION

To my family who have meant and continue to mean so much to me.

TABLE OF CONTENTS

# LIST OF TABLES

# LIST OF FIGURES

# LIST OF ACRONYMS

| | |
|---|---|
| 3D-CRT | Three-dimensional conformal radiotherapy |
| AAPM | American Association of Physicists in Medicine |
| ACS | American Cancer Society |
| ADCs | Analogue to Digital Converters |
| aSi | Amorphous Silicon |
| BBC | British Broadcasting Corporation |
| CRT | Conformal Radiation Therapy |
| CT | Computed Tomography |
| DF | Dose Correction Factor |
| EPID | Electronic Portal Imaging Device |
| eV | Electron-Volts |
| FS | Field Size |
| $FS_x$ | Field Size Side |
| GB | Gigabyte |
| GHz | Gigahertz |
| GLOBOCAN | Global Cancer Data |
| GUI | Graphical User Interface |
| Gy | Gray |
| IAEA | International Atomic Energy Agency |
| IARC | International Agency for Research on Cancer |
| IBA | Ion Beam Applications |
| IC | Ionization Chamber |
| ICRU | International Commission on Radiation Units and Measurements |

| | |
|---|---|
| IMRT | Intensity Moderated Radiation Therapy |
| iViewGT™ | iView Guided Therapy |
| LET | Linear Energy Transfer |
| LINAC | Linear Accelerator |
| MeV | Mega Electron Volt |
| mGy | Milligray |
| MHz | Megahertz |
| MLC | Multileaf Collimator |
| MoH | Ministry of Health |
| MoH | Ministry of Health |
| MOSFET | Metal–Oxide–Semiconductor Field-Effect Transistor |
| MRI | Magnetic Resonance Imaging |
| mSv | Millisievert |
| MU | Monitor Unit |
| MV | Megavoltage |
| nC | Nano-Coulomb |
| OD | Optical Density |
| PCI | Peripheral Component Interconnect |
| PET | Positron Emission Tomography |
| PMMA | Polymethyl Methacrylate |
| PSF | Pixel Scaling Factor |
| PTW | Physikalisch - Technische Werkstätten |
| QA | Quality Assurance |
| QC | Quality Control |
| Rad | Radiation Absorbed Dose |

| | |
|---|---|
| SAD | Source to Axis Distance |
| SDD | Source to Detector Distance |
| SED | Source to EPID Distance |
| SSD | Source to Surface Distance |
| SSDL | Standard Dosimetry Laboratory |
| Sv | Sieverts |
| TFT | Tin Film Transistor |
| TG | Task Group |
| TIFF | Tagged Image File Format |
| TPS | Treatment Planning System |
| TRS | Technical Report Series |
| WHO | World Health Organization |

# LIST OF CONSTANTS AND SYMBOLS

| | |
|---|---|
| $\varepsilon$ | Effective Dose |
| $S_{EPID}$ | EPID Signal |
| $CF_t$ | Thickness Correction Factor. |
| $S_{EPID\_normalized}$ | Normalized EPID Signal |
| D | Absorbed Dose |
| $\nabla$ | Gradient |
| $D_{w,Q}$ | Absorbed Dose in Water |
| $H_T$ | Equivalent Dose |
| $k_{Q_0}$ | Photon Radiation Quality Factor |
| $k_{TP}$ | Temperature-Pressure Correction Factor |
| $M_Q$ | Measured Ionization Chamber |
| $Q_0$ | Reference Radiation Quality Factor |
| $W_R$ | Radiation Weighting Factor |
| $W_T$ | Tissue Weighting Factor |
| X | Exposure |

# CHAPTER ONE

# INTRODUCTION

This chapter outlines the need for accurate delivery of radiation doses to patients during cancer treatments. It provides several incidents of dose misadministration in radiotherapy, which could have been prevented if proper measures had been put in place. The chapter further provides the need for *in vivo* dosimetry including quality checks of absorbed doses to patients during radiation treatment. In addition, Chapter One provides information on the current situation of *in vivo* dosimetry practices in Ghana, whiles outlining major challenges in determining absorbed doses to patients during cancer treatments. Moreover, the chapter gives information on the main objective of this study, which seeks to provide a solution to major challenges of *in vivo* dosimetry.

## Background to the Study

Cancer, which occurs as a result of abnormal growth of human cells, has been one of the major health challenges over the past years. In recent years, several treatment options such as surgery, chemotherapy and radiation therapy (radiotherapy), have been recommended for cancer treatments. One of these options mostly recommended by oncologists is the external beam radiotherapy option (Liauw et al., 2013). The external beam radiotherapy treatment option uses high-energy beams of radiation to shrink tumours and destroy cancerous cells. These kill cancer cells, or stop cancerous cells from multiplying (Baskar et al., 2012; Kondo, 2018).

Radiotherapy has developed as one of the comprehensive and effective modalities for cancer care. It aims to eradicate cancerous cells with the utilization of ionizing radiation. It utilizes high-energy radiation such as photons and charged particles to destroy cancerous cells and shrink tumours (Lemoigne & Caner, 2007). The radiation may be delivered externally by a machine situated outside the human body, or it may be produced from a radioactive source placed in the body inside the cancerous tissue, or close to the cancerous tissues.

In reports by the World Health Organization (WHO) (Plummer et al., 2016), International Agency for Research on Cancer (IARC) (Ferlay et al., 2018), and European Society for Medical Oncology (IARC, 2014), cancer is understood to be one of the reasons for high levels of mortality and morbidity globally, with about 14 million new cases and 8.8 million cancer related deaths in the year 2015. In 2008, it was predicted that annual cancer cases would increase from 14 million in 2012 to 22 million by 2030 (American Cancer Society, 2007). The report further indicated that more than 60% of annual cancer incidences worldwide occur in Africa, Asia and Central and Southern America. These regions are responsible for 70% of the world's cancer deaths.

In 2008, about 681,000 new cancer cases and 512,400 cancer deaths were recorded in Africa, with the numbers projected to double by 2030 as a result of aging and growth of the population (Ferlay et al., 2018; Torre et al., 2015), and a potential to be even higher because of the adoption of behaviors associated with western lifestyles, such as smoking, insalubrious diet, and physical inactivity.

Global cancer data (GLOBOCAN) has estimated that 16,600 cancer cases occur yearly in Ghana, yielding an age standardized rate of 109.5 cancer cases per 100,000 persons (Ministy of Health, 2016).

In the WHO technical manual (Gantchew, 2010; WHO, 2008), it is reported that according to available practices, 52% of patients should receive radiotherapy at least once during the treatment of their cancer either as part of their primary treatment or in connection with recurrences or palliation. When combined with other treatment modalities such as surgery and chemotherapy, radiotherapy plays a huge role in the treatment of 40% of those patients who are cured of their cancer (Gantchew, 2010).

The WHO further reports that between the years 1976 and 2007, 3125 patients were reported to be affected by errors in radiotherapy treatments which led to adverse effects (Gantchew, 2010; WHO, 2008). From the report, thirty-eight (1.2%) of the affected patients died due to radiation overdose toxicity. Only two reports assessed the number of deaths as a result of radiation under-dosage. Between the years 1992 and 2007, over 4500 near misses (out of 4616) were reported in the literature and publicly existing databases (Gantchew, 2010). Regular quality assurance (QA) programmes are therefore required to ensure accurate dose delivery to tumour cells and to have an exact knowledge of dose delivered to patients.

It is an important practice that the right dose of radiation is delivered to the correct anatomical site in radiotherapy. As such, several studies have mentioned the need for comprehensive QA programme at radiotherapy centres

(Baily et al., 1994; Herman et al., 2001; Klein et al., 2009; Lemoigne & Caner, 2007; Slosarek et al., 2010; van Elmpt et al., 2008).

A major area of concern in QA is the exact knowledge of the dose delivered to the patient during treatment. QA assumes a significant role of verifying such doses delivered during actual treatment delivery to the patient, and therefore plays a vital role of ensuring that the actually planned treatment has been precisely replicated on the patient (Huq et al., 2016; IAEA, 2013)

With new advancements in radiotherapy treatments emerging, the requirements for accuracy and exact dose delivery are increased. Among others, the use of imaging systems to verify patient setups during radiotherapy procedures is key to achieve the desired accuracies in treatment (Glide-Hurst & Chetty, 2014; Malicki, 2012). Until recently, radiographic films had been the traditional means of verifying patient's anatomical position (Williamson, 2014). Structurally, these films have light-sensitive emulsion coated on both sides, and are normally sandwiched between two metals or fluorescent screens during treatment positioning verification. Typical conventional metal screen combinations include two sheets of lead of thickness 0.15 mm and 0.3 mm for the front and back screens respectively, or a 1.0 mm thick copper front screen in conjunction with a 0.25 mm lead back screen (Mayles et al., 2007). The front screen absorbs the electrons from the patient and the intervening air column to reduce blurring in the image while generating recoil electrons through photon interactions that directly expose the film. A lead back screen is usually used to intensify the fluence of the back-scattered electrons. The back screen has been

reported to reduce the dose or exposure per given density by up to 50% (Lemoigne & Caner, 2007).

The use of radiographic film is effectively a non-real-time imaging technique. Some radiotherapy centres will wait for the few minutes to develop and read the film; this is especially true in difficult cases. Most of the time, it is used retrospectively. It is not possible to continuously monitor the patient's position throughout the treatment. Similarly, gross errors such as missing blocks, inverted wedges, or wrongly set collimators will not be detected until it is too late. Film cannot be used to check the dynamically-varying beam parameters such as found in rotation therapy, dynamic wedges, or moving multileaf-collimator blades (Mayles et al., 2007). In order to provide an instantaneous verification of the patient setup, electronic portal imaging devices (EPIDs) have been developed and are attached to the gantry of linear accelerators (LINACs).

In radiotherapy treatments, it is necessary that correct dose is delivered to the intended target. Portal dosimetry aims to verify the actual dose delivered to a patient during treatment. There are several potential error sources in a radiotherapy treatment which can lead to overexposure and underexposure of patients (Mayles et al., 2007). Potential error sources may arise as a result of errors in the data transfer from treatment planning system (TPS) to treatment equipment, errors in the functioning of the treatment equipment, and errors that are patient related due to set-up errors or organ motion (International Atomic Energy Agency, 2001). Several QA procedures have been employed to detect and correct such errors. EPIDs are employed for this task because they are not

only useful for imaging and position verification but are also suited for dosimetry, both pre-treatment and during treatment (Nijsten, 2009).

**Statement of the Problem**

The effective use of radiotherapy relies on the accuracy of dose delivery. The real danger is when the error in administration goes undetected. This may result in healthy tissues being exposed to unnecessarily high levels of radiation doses, or that the tumour site may not receive the full effect of therapy due to under-dosage. Several cases of dose misadministration have been reported in recent years. For instance, a prostate cancer patient was irradiated in the wrong spot during 32 of 38 treatment fractions, while another prostate patient at the same institution received 19 misguided fractions (Bogdanich, 2010; Crook et al., 1995) . Due to this, *in vivo* dosimetry has been considered as an important part of quality management of every radiotherapy department (International Atomic Energy Agency (IAEA), 2013). In vivo refers to measurements of dose received by the patient or phantom during radiation therapy.

The current *in vivo* dosimetry technique used at the Sweden Ghana Medical Centre (SGMC), as well the National Centre for Radiotherapy and Nuclear Medicine Department at Korle-Bu and Komfo-Anokye Radiotherapy Directorate at Kumasi, is where diodes are placed on the crosswire at the central beam with adhesive tapes over patients for support, after satisfactory patient set up. The following are the drawbacks of this technique:

1. The diode is difficult to place correctly. A slight displacement of the diode from the isocentre of the beam may lead to false positive/ negative results. Several factors may contribute to the displacement of the diode, including

the movement of patients during treatment delivery, and the loosening of the adhesive tapes.

2. The placement of diodes on patients is time consuming during radiotherapy treatments, requiring much time for each patient.

Additionally, the current growing trend in radiotherapy treatment options such as the introduction of Intensity Moderated Radiation Therapy (IMRT) has increased the need for high accuracy in the dose delivery to patients. For these purposes, a comprehensive QA programme that addresses these issues, is needed to verify the actual doses given to patients during radiotherapy treatment delivery.

**Objectives**

The main objective of this study was to develop an in-house transit dosimetry calculation model for verifying patient dose using aSi EPID, and which could be fast, adequate and accurate to be employed in clinical routine. The model will be applicable to 3-dimensional conformal radiotherapy (3D-CRT) fields.

Other specific objectives are

1. To develop VB.net and C++ codes to help reconstruct doses from real time EPID images acquired during radiotherapy external beam treatments.
2. To use the model for actual treatment verification, to ensure safe treatment delivery in different phases of the external beam radiation therapy.

**Scope of Study**

The scope of this study was confined to:

Acquisition of patient images during radiotherapy treatments using EPID. The study was based on vb.net and C++ modelling of data obtained from measurements related to portal dosimetry. It was further based on the linking of EPIDs with TPS using radiation transit dosimetry.

**Relevance and Justification**

Studies have shown that, an extreme misadministration of radiation doses may lead to radiation necrosis to critical organs or structures and could be fatal. Recently, a report from the Scottish government said a cancer patient was given a radiation overdose of 100% more than the intended prescribed dose during radiation treatment (British Broadcasting Corporation, 2016). With the numerous reported cases of radiation accidents worldwide, it is increasingly becoming incumbent that a dose verification method is necessarily practiced in radiotherapy departments to improve accuracy in dose delivery, and reduce radiation misadministration.

Institutional protocols and treatment techniques are becoming more important, as more precise treatment delivery limits the tolerance for error. During radiotherapy planning and dose delivery process, in which many variables influence the intended dose delivery, the benefits of improved treatment technology and 3D conformal radiation therapy could only be achieved if the cancerous tumour and normal tissues are given the correct radiation dose prescribed in the treatment plan. It is, therefore, necessary to have a technique and an "end-to-end" test to check the performance of the total treatment chain. This technique and test should evaluate the complete process from dose calculation, through image-based treatment design, to dose delivery.

For this purpose, EPID dosimetry would play an important role. Additionally, the recent sequence of severe accidents and dose misadministration in radiotherapy could have been prevented if *in vivo* dosimetry systems were in place. This has given credence for arguments in favour of *in vivo* dosimetry (Bogdanich, 2010; Derreumaux et al., 2008; IAEA, 2001; Mans et al., 2010). In other words, *in vivo* dosimetric tests before and during treatments should avoid significant over-dosages and undesirable under-dosages.

**Organization of the Study**

Chapter One of this thesis gives a general overview of the research topic, and problems to be investigated. The chapter gives an insight of radiotherapy dosimetry, and provides the motivation and aims of this work.

Chapter Two focuses on the physics of portal imaging and other dosimeters used in this work, as well as the conceptual basics of aSi EPID, and provides an insight of physics of radiotherapy dosimetry. The Chapter further provides the literature review of the dosimetric studies that have been conducted using EPIDs. The chapter finally provides information on the general concept of modelling.

Chapter Three addresses materials and methods employed in the study. The chapter describes all experimental setups and procedures implemented in this study. The development of the vb.net and C++ code and measured parameters are all presented.

Chapter Four provides findings of this work including correction factors for transit dosimetry.

Chapter Five presents a comprehensive summary of the major findings in this study. This chapter provides the concluding summary of this work and recommendations to relevant stakeholders.

**Chapter Summary**

In Chapter One, the need for accurate delivery of radiation doses to the targeted tissues, and accurate determination of absorbed doses to patients during cancer treatments was provided. The chapter outlined radiotherapy risks, and provided several cases of radiotherapy misadministration of doses, while indicating the vital role of QA in radiotherapy procedures. The chapter further provided information on the current situation of *in vivo* dosimetry in Ghana, whiles providing the need for EPID as a preferred QA tool among the different types of radiation measuring devices. Additionally, Chapter One provided an insight of the current challenges associated with the determination of exact radiation doses to patients during radiation treatments, indicating the need for a routinely clinically applicable, and an efficient way to carry out dose verifications. A technique which could be simple, adequate and accurate to be employed in the clinical routine, was therefore indicated as the main objective of this work.

# CHAPTER TWO

# LITERATURE REVIEW

## Introduction

In this chapter, the physics of portal imaging and all dosimetric devices used in this work is provided, as well as the description of various works done on EPIDs for the purpose of dosimetry. The chapter also presents the conceptual basics of aSi EPID, and provides literature review and an insight on *in vivo* dosimetry with various dosimetric devices. Finally, the chapter provides information on the general concept of modelling.

## External Beam Radiation Treatment

In radiotherapy, the ultimate goal is to eradicate or reduce cancerous cell volume without causing significant complications to the normal surrounding tissues. Radiotherapy originated after the discovery of X-rays by Wilhelm Conrad Roentgen in 1895 (Khan, 2010; Mould, 1993; Reynolds & Tansey, 2006). Many scientific discoveries and approaches have since been developed in radiotherapy over the past decades.

The most frequently used radiotherapy technique is an external beam treatment with photons using the linear accelerator (LINAC). In LINAC, electrons are generated and accelerated to high energies of 4 MeV to 25 MeV (Dokholyan et al., 2012; Thwaites & Tuohy, 2006). The accelerated electrons produce X-rays when they collide with a tungsten target and the resulting photon beam can be used for treatment after additional filtering, collimation and shielding of the beam in the treatment head (Khan, 2010). Beam shielding is a

prerequisite in high dose-high precision radiotherapy in order to obtain dose distributions that conform to the tumor volume while sparing neighbouring healthy tissue.

A multileaf collimator (MLC) can be used for beam shielding. The MLC is located inside the treatment head of a LINAC and consists typically of a series of 80 to 160 metallic leaves which can be positioned individually to shape the beam aperture (Dokholyan et al., 2012; Khan, 2010). Furthermore, modern LINACs are usually equipped with an EPID which allows imaging of the high energetic MV photon beam that exits the patient during treatment. These images can be used for patient set-up verification or detection of organ motion but also for dosimetric verification of a treatment which is called portal dosimetry.

Figure 1 shows a schematic diagram of a LINAC. Before the treatment can be applied to a patient, an individual treatment plan is generated using a TPS. This system uses three-dimensional (3D) imaging information of a patient to model the position and shape of both tumor and healthy tissues (Barrett et al., 2009). Based on this localization, an optimum beam configuration including photon beam energies, field sizes, shielding, beam directions and relative beam weighting can be determined. The end result is a definition of beam parameters that is needed to set-up the LINAC and the 3D dose distribution inside the patient that documents the prescribed radiotherapy treatment.

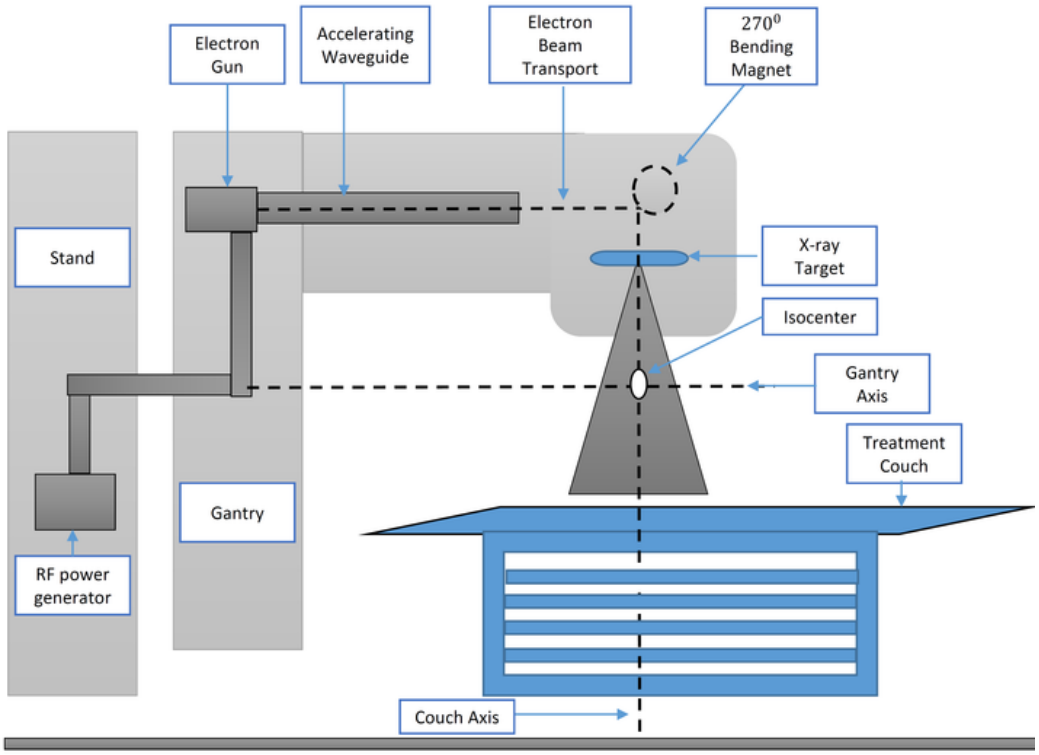


Figure 1: Schematic diagram of a LINAC (Thwaites & Tuohy, 2006)

With the introduction of computed technology over the past years, several advancements have been made in external beam radiotherapy towards a more precise treatment. Among these techniques are the intensity-modulated radiation therapy (IMRT) and the conformal radiation therapy (CRT). CRT utilizes computed tomography images and advanced computers to precisely map locations of cancerous tumours in 3D. In this technique, the patient is kept immobile through the use of plastic molds to achieve positional reproducibility in all treatments. The radiation beams are planned to match the shape of the tumour, and the radiation doses are delivered to the tumour from several directions (Barrett et al., 2009; Rush, 2014).

Similar to the CRT, intensity-modulated radiation therapy (IMRT) also aims at matching radiation beams to conform to the shape of cancerous tumours. However, IMRT utilizes a rather advanced technology to manipulate photon and proton beams of radiation to conform to the shape of a tumour. This provides better control by increasing doses to targets while avoiding or reducing exposure of healthy tissues to limit the side effects of treatment (Mayo, 2018; Taylor & Powell, 2004).

**Linear Accelerator**

LINAC as designed for radiotherapy, customizes high energy X-rays and electron beams to conform to a tumour's shape and destroys cancer cells while sparing surrounding normal tissues. It uses high radio-frequency (RF) electromagnet direct current waves to accelerate electrons to high energies in a linear path, inside a structure called the accelerator waveguide (Mayles et al., 2007).

Bunches of electrons generated in the LINAC's gun are injected into the guide in synchronism with pulsed microwave radiation. LINAC uses microwave technology to accelerate the high energy electrons (6 MeV or above) through straight trajectories in specialized evacuated structures called accelerating waveguides. The accelerated electrons then collide with a heavy metal target. Due to these collisions, megavoltage (MV) X-rays are produced from the target. These MV photons would be shaped as they exit the LINAC to conform to the tumour's shape, and would be directed to the patient's tumour.

Radiation can be delivered to the tumour from different angles by moving the treatment couch and rotating the gantry (Khan, 2010).

Electron from LINAC unit are accelerated to higher energies and are allowed to exit the LINAC unit as electron beam, and are used for the treatment of superficial lesions up to about 70 mm deep. However, for more deep-seated tumours, it is better to use photon beams. If the electron beam is to be used for therapy, the originally narrow beam of electrons must be broadened by scattering the electrons (Khan, 2010).

Various types of LINAC are available for clinical use. Some provide X-rays only in the low MV range (4 or 6 MV), while others provide both X-rays and electrons at various MV energies. A typical modern high energy LINAC would provide two photon energies (6 and 18 MV) and several electron energies (6, 9, 12, 16 and 22 MeV) (Lemoigne & Caner, 2007).

The LINAC unit has source to surface distance (SSD) of 80-100 cm, and this relatively large SSD allows treatment of large fields. Treatments of large volume tumours are also done more uniformly due to the depth dose characteristics. The relatively small focal spot limits the penumbra of the beam, and results in a relatively sharper edge to the treatment field. Additionally, high output from the LINAC machine shortens the treatment time for individual patients and allows treatment of a larger number of patients per day (Mayles et al., 2007).

**External Beam Production**

In the treatment of skin lesions, it is preferable to use kilovoltage X-ray beams (orthovoltage radiotherapy), unlike deep-seated tumours which require MV beams (MV radiotherapy). MV beams range from 1 MV to 25 MV, and are not only more penetrating, but they deposit maximum dose beneath the skin surface thereby providing skin-sparing effect. Basically, photons traverse the entire tissue thickness, but deposit less dose as the depth increases. Moreover, due to the fact that the principal interaction of radiation with tissue is through the Compton effect, the locally absorbed dose is independent on the atomic number of the tissue, and the dose to bone is not enhanced (Mehta et al., 2010).

Orthovoltage radiation beam on the other hand, is a relatively low energy, typically ranging from 200-500 kV. Orthovoltage beam deposits its maximum dose at the skin surface and eventually the dose decreases to 90% at approximately 2 cm of depth in the tissue. This results in acute effects to the patient's skin. It is also practically impossible to treat deep-seated tumours due to the limitations of the tolerance levels of the overlying tissues (Podgorsak, 2005). With orthovoltage beams, the skin dose becomes prohibitively large when adequate doses are to be delivered to deep-seated tumours. Moreover, there is differential absorption of dose in bone as against soft tissue, which could lead to bone damage or necrosis (Podgorsak, 2005).

The LINAC is currently the principal means of generating MV beams. Space constraints limit the maximum electron energy achievable to about 22 MeV. However, in practice, this energy is sufficient for satisfactory treatments (Mayles et al., 2007). The electron beams from LINACs can be converted to X-

rays or can alternatively be directly used for patient treatment. LINACs have the advantage of more penetrating beams, the versatility of the choice of beam energy, a smaller penumbra at the edge of the beam, and the delivery of a higher dose rate (Mayles et al., 2007). However, several modern LINACs are also capable of producing electrons, which could be used for treatment situations where the limited depth penetration of electrons is useful.

Photon beams emitted by Cobalt units have two distinct energies (1.173 MeV and 1.332 MeV). In contradiction to LINAC and orthovoltage units, the $^{60}$Co source emits radiation constantly, and must be shielded when the machine is in use or not (Cherry & Duxbury, 2009). Compton emission generated in the $^{60}$Co source results in the beam incident on the patient having a continuum of energies, with a mean energy less than 1 MeV. At $^{60}$Co energies the Compton effect is the principal interaction mechanism in the patient, which generates further low-energy scattered radiation. A $^{60}$Co photon beam has a greater penetrability for more deeply seated tumours due to their higher energy. There is uniform dose deposition in bone and soft tissue (unlike orthovoltage). In the $^{60}$Co unit, there is a dose build-up region which allows the maximum dose to be deposited at a depth of 0.5 cm underneath the skin surface, and hence providing skin-sparing effect (Cherry & Duxbury, 2009).

**Beam Interaction Process**

There are several interaction processes that occur when ionizing radiation interacts with matter. These are dependent on the nature and energy of the primary radiation beam and the structure of the medium of propagation.

*Elastic Scattering*

Elastic scattering involves a collision interaction between the incident photon and an electron orbiting the nucleus of an atom in the attenuating medium. The interacting photon has energy considered insignificant when compared with the binding energies of the electrons. This inhibits the transfer of energy from the incident photon to the electron. Consequently, the incident photon continues to travel through the medium but is scattered in a different direction. In this interaction, there is no resultant loss of energy from the X-ray beam, and the interaction process normally occurs at very low photon energies (Khan, 2010; Podgorsak, 2005).

*Photoelectric Absorption*

Photoelectric absorption occurs when a photon is totally absorbed by an inner-shell electron and the electron (photoelectron) is ejected. Photoelectric absorption normally occurs at X-ray energies utilized for diagnostic imaging, radiotherapy, kilovolt imaging, and superficial and orthovoltage radiation therapy. Here, the energy of the incident photon is equal to or slightly greater than the binding energy of the inner orbital electrons of the atoms of propagation. During this interaction, the incident photon interacts with an inner shell electron, transferring all of its energy to that electron. The incident photon is then absorbed, transferring all its energy to overcome the binding energy of the orbiting electron causing it to be ejected from the atom. The ejected electrons (photoelectrons) are then emitted at all angles. The higher the energy of the incident photon, the smaller the angle of photoelectron emission in order to

conserve momentum and energy in the interaction (Lemoigne & Caner, 2007; Mayles et al., 2007).

*Compton Scattering*

The Compton interaction involves a collision interaction between the incident photon and a 'free electron', resulting in both absorption (transfer of energy from the X-ray beam to the atoms of the attenuating medium) and scattering (path of the incident photon is altered) (Khan, 2010). As the energy of the incident photon increases, the binding energy of the orbital electrons in the attenuating material becomes almost insignificant in comparison. The electron is no longer bound and is considered to be a 'free electron'.

*Pair Production*

Pair production occurs when a high-energy photon is absorbed by an atomic nucleus, and is converted to matter and antimatter. Here, the photon disappears, and the energy is converted into an electron and a positron. The positron eventually combines with an electron, producing two 511 keV photons that are emitted at 180 degrees to each other, resulting in annihilation radiation. Pair production has a photon energy threshold of 1.02 MeV, below which pair production cannot occur (Khan, 2010; Williams & Thwaites, 2000). The 1.02 MeV is the sum of the rest mass energies of an electron and a positron, and is thus the energy required to produce an electron (511 keV) and positron (511 keV) pair (Smallwood et al., 1999).

## Phantoms

*Polymethyl Methacrylate (PMMA) Slab Phantoms*

PMMA slab phantoms (Figure 2) are square blocks of varying thicknesses which may be build out of different materials. The most commonly used material is a water equivalent solid, but other phantoms representing lung, bone and metal may be used. PMMA slab phantoms may be placed within a beam to simulate various conditions. Ionization chambers may be placed within pre-hollowed holes to measure dose rates, or film may be placed between two slabs to measure beam profile and isodose distributions. PMMA slab phantoms are particularly useful as they are solid and easy to position, requiring minimal efforts to setup (OzRadOnc, 2017a; Physikalisch-Technische Werkstätten (PTW), 2016a).

Figure 2: PMMA slab phantoms used for absolute dosimetry (Ion Beam Applications (IBA), 2013)

*Water Phantoms*

Water phantoms are the primary tools used for absolute dosimetry. They consist of a transparent plastic tub (about 60 cm in all dimensions) filled with water. A waterproof ionization chamber (IC) can be placed on a movable arm within the phantom. This can accurately manoeuvre the IC to a number of positions to measure dose rate. Water phantoms are useful for absolute dosimetry as they are homogenous and water equivalent, a close substitute for soft tissue and muscle (OzRadOnc, 2017a).

*Anthropomorphic Phantoms*

Anthropomorphic phantoms are constructed to mimic human tissues, including internal inhomogeneities. These phantoms are typically formed by

multiple slabs arranged in the axial plane. This allows film to be placed between the slabs. The slabs also contain holes for insertion of IC and Thermoluminescent dosimeters (TLD). In Figure 3, an image of an anthropomorphic phantom is shown mimicking the human pelvic tissues.

Figure 3: Image of a male pelvic anthropomorphic phantom (MediTron, 2012)

**Radiation Therapy Dosimetry**

In defining the quantity of dose or radiation exposure, the word 'dosimetry' is used. Exposure is a measure of radiation on the foundation of its ability to produce ionization in air under standard conditions of temperature and pressure. The expression 'dose' refers to the amount of energy absorbed per unit of mass at a site of interest (Khan, 2010).

*Exposure, X*

Exposure is an index of the ability of radiation to ionize air, and is only applicable to photon beams in air. It expresses the intensity, strength, or amount of radiation in an X-ray beam based on the ability of radiation to ionize air. According to the International Commission on Radiation Units and Measurements (ICRU) (ICRU, 1998), exposure is defined as the quotient of ΔQ by Δm:

$$X = \frac{\Delta Q}{\Delta m} \qquad (1)$$

In Equation 1, ΔQ denotes the the total charge of the ions of one sign produced in air when all the electrons liberated by photons in air of mass, Δm are completely stopped in air. Exposure is only defined for photons with energies less than 3 MeV and cannot be used for electrons, neutrons, or protons. The SI unit of exposure is Coulomb per kilogram (C/kg) or in roentgens (R) in non-SI units: 1 R = $2.58 \times 10^{-4}$ C/kg.

*Absorbed Dose*, D

Absorbed dose measures the amount of any type of ionizing radiation energy absorbed per unit mass of a medium, and is defined for types of radiations (ie charged and uncharged particles). Absorbed dose is defined as the total energy imparted to matter, ΔE per unit mass, Δm when an ionizing radiation field interacts with matter. Absorbed dose is specified in units of J/kg or grays (Gy) (Alaei, 2008; Khan, 2010).

$$D = \frac{\Delta E}{\Delta m} \qquad (2)$$

The expression "energy imparted" as used to define absorbed dose, is the radiation energy absorbed in a volume. Therefore, the term "absorbed dose" refers to an exactly defined volume and only to the volume. The energy imparted (E) by the ionizing radiation to matter, as expressed by the ICRU (Wambersie, Zoetelief, Menzel, & Paretzke, 2005), is given by:

$$E = R_{IN} - R_{OUT} + \Sigma Q \qquad (3)$$

where $R_{IN}$ in equation (3), denotes the sum of the energies (without rest mass energies) of all the ionizing particles that are incident on the volume, $R_{OUT}$ denotes the sum of the energies (without rest mass energies) of all the ionizing particles that leave the volume. ∑Q represents the sum of all changes (decreases: positive sign, increases: negative sign) of the rest mass energy of nuclei and elementary particles in any nuclear transformations that occur in the volume. Traditionally, the unit of absorbed dose is the rad (radiation absorbed dose), where 1 Gy equals 100 rads.

**Absorbed Dose Determination in PMMA Solid Water Phantom**

In determining absorbed doses to PMMA phantoms, a number of factors in addition to the calibration factor of the IC have to be taken into account. In this study, the determination of absorbed doses in the PMMA phantoms with Farmer-Type PTW IC 30010 (of a calibration factor $N_{D,w,Q_0}$ ) was done at a reference radiation quality factor $Q_0$. The IC was positioned according to the reference conditions and the absorbed dose ($D_{w,Q}$) calculation was given by equation 4 (IAEA, 2000).

$$D_{w,Q} = M_Q \times N_{D,w,Q_0} \times k_{Q_0} \times k_{TP} \qquad (4)$$

In equation 4, $k_{Q_0}$ denotes the radiation quality factor for photons, $M_Q$ is measured IC values (in coulomb), $N_{D,w,Q_0}$ is calibration factor for the Farmer-type IC IBA used in this study, and $k_{TP}$ is the temperature-pressure correction factor expressed in equation 4.

*Equivalent Dose, $H_T$*

For the same absorbed dose to a tissue or volume, different forms of ionizing radiation can have different biological effects. Equivalent dose is therefore used to compare the biologic effects of the various types of ionizing radiation on a tissue or organ. In particular, high-linear energy transfer radiation such as electrons, are more damaging to tissue than low- linear energy transfer radiation (e.g. X-rays). Equivalent dose attempts to normalize these differences, and is calculated as the product of the absorbed dose, D averaged over a tissue or organ and the radiation-weighting factor, $W_R$:

$$H_T = D \times W_R \tag{5}$$

where $W_R$ in equation 5 expresses the relative biological effectiveness of different types of radiation, and depends on the radiation linear energy transfer (LET) value (Khan, 2010; Podgorsak, 2005). Equivalent dose is expressed as sieverts (Sv) in the SI system and as rems (roentgen equivalent man) in non-SI units. One sievert equals 100 rem.

*Effective Dose, $\varepsilon$*

Usually, most medical radiologic exposures result in a non-uniform dose distribution within the patient. The effective dose adds the dose of all exposed

organs to give an estimate of the total risk to a patient exposed during a radiographic procedure. In other words, effective dose is used to estimate the risk in humans, and is expressed as the sum of the products of the equivalent dose to each organ or tissue ($H_T$) and the tissue weighting factor ($W_T$) (Khan, 2010; Mayles et al., 2007):

$$\varepsilon = \sum W_T \times H_T \qquad (6)$$

Effective doses are expressed in terms of equivalent dose and use mSv, which are numerically equal to mGy.

**Clinical Radiation Dosimetry**

In radiotherapy, the most significant job of a medical physicist is to ensure that the TPS prescribed doses are accurately delivered to the patient. Till date, verifying that each prescribed dose being delivered is as intended remains a critical issue as a result of a number of complicating factors (Larry, 2002). For instance, a tumour position may vary from treatment sessions to treatment sessions, and may affect dose deliveries if care is not taken. Additionally, other influences such as patient breathing, as well as changes in patient positioning during treatments may affect accuracy of dose (Baily et al., 1994; IAEA, 2013). For these purposes, it is recommended that appropriate methods be used to verify intended radiotherapy doses.

The measurement of exact delivered doses to patients requires several steps, and remains a key concern of medical physicists and radiation therapists. As such, an appropriate quality control (QC) measure is important to ensure that

prescribed radiation doses to patients are accurately delivered to patients during radiotherapy procedures.

Concerns about radiotherapy dosimetry are highly important as there is a clinical requirement to accurately deliver doses to patients during treatments. During radiotherapy procedures, maximum doses are given to the tumour while minimizing doses to the surrounding normal tissues. A small discrepancy in the intended (planned) dose to tumour may shift treatment from proper tumour eradication to a fatal tissue injury resulting from over-dosage, as well as failure to control the tumour due to under-dosage. According to IAEA Human Health Reports No. 8 (IAEA, 2013), and ICRU report No. 83 (Menzel, 2010), a 5% discrepancy in doses delivered to target volumes in radiotherapy is required. In order to ensure that the prescribed dose is accurately delivered to target volumes, efficient devices are required to carry out radiotherapy dosimetry. *In vivo* dose verification is used to uncover and avoid major deviations between the intended (prescribed) radiation dose and the actual dose received by the patient. This method is normally performed by putting radiation dosimeters such as diodes, TLDs, Metal–Oxide–Semiconductor Field-Effect Transistors (MOSFETs) and radiochromic films on the skin or inside the patient to measure doses at specific points in the patient.

In this section, description of various dosimetric techniques and devices used in this work including IC, TLDs, and EPIDs, are all presented.

**Portal imaging Dosimetry**

In recent years, the use of external beam radiotherapy to treat cancer has been characterized by a variety of significant technical advances such as the introduction of advanced imaging modalities including magnetic resonance imaging (MRI), computed tomography (CT), ultrasound, positron emission tomography (PET) among others. Additional advances are the introduction of gantry-mounted LINACs that have the ability of performing treatments at isocentre with mega beam X-rays. These advanced technologies have made it possible to obtain useful anatomical and functional information for radiotherapy treatment planning purposes (Herman et al., 2001; Pai et al., 2007; Slosarek et al., 2010).

In general, these advanced technologies have further assisted in achieving the ultimate goal of radiotherapy, by improving accuracy of dose delivery to targets during radiotherapy procedures. In achieving this objective, the targeted tumour is generally irradiated in different directions from several radiation fields.

In spite of all these advanced technologies, verifying that all radiation fields deliver exactly the prescribed doses remain a critical issue as a result of several factors. For instance, the position of the tumour in the patient may vary from treatment to treatment, or even during treatment, due to such influences as breathing, the degree of extension of the bladder and changes in patient positioning (Rush, 2014). Moreover, errors in the set-up of the patient, and of the beam collimators are also possible. For these purposes, it has long been acknowledged that the usage of the therapeutic X-ray beam to create portal

images could be of significant benefit in assuring exact delivery of the radiation dose (IAEA, 2013).

Until recently, portal imaging has been used primarily for verifying patient positions in radiotherapy. The image quality, although constrained by the nature of the radiotherapy application, is sufficient to provide significant, useful information for target localization and dose verifications (Mayles et al., 2007).

The first portal images were acquired using a radiographic film (Pai et al., 2007). A radiographic film basically comprises a radiation sensitive emulsion that is coated on a transparent polyester base. The emulsion is composed of halide crystals. The specific emulsion composition and processes involved in manufacturing varies with the manufacturer, and are mostly not disclosed by manufacturers (Pai et al., 2007). In principle, as the emulsion is exposed to ionizing radiation, ionization takes place in the silver halide crystals, which then result in the formation of a latent image.

However, recent advances in technology have allowed for the digital acquisition of these images using EPIDs. For electronic portal imaging rather than a radiographic film, images of an EPID are acquired by placing the EPID in the exit radiation beams from the patient. The images are acquired and displayed digitally on a video screen instantly during radiotherapy irradiations. The images are then processed on the computer.

**EPID Dosimetry**

As discussed in the previous section, EPIDs were initially considered as a substitution for radiographic film for patient positional check during radiation treatments. EPIDs have been developed to acquire and display portal images in as short a time as possible, and have exhibited several advantages over radiographic films. For instance, images from EPIDs could be analyzed instantly for on-line verification, or more images could be acquired per treatment field without the need to enter the treatment room (Herman et al., 2001). Additionally, EPID images are in digital format, which assists direct image processing, contrast improvement and image matching. Moreover, digital archiving saves space and allows for rapid recall of images through a computerized network (Slosarek et al., 2010).

EPIDs are two dimensional radiation detectors attached to a LINAC. EPIDs are capable of detecting the intensity of the exit radiation beam from a patient during radiotherapy treatments. They appear in digital formats, and provide several advantages over radiographic films. For instance, unlike radiographic films, data acquired from EPID require no time for development, and are readily accessible from any computer for quick performance of quantitative analysis. Additionally, the integration of EPIDs with the LINAC enables image acquisitions to be done faster and accurately. Moreover, EPID also possesses an advantage of allowing image contrast adjustments to be done even after image acquisitions, thereby reducing the necessity of repeating films in order to highlight specific anatomical details.

In principle, the intensity variations in the portal image signal are the result of differences in anatomical structures such as bone, lung, and soft tissues (Greer & Popescu, 2003). In their study, Van Elmpt et al. (2008) have extensively depicted two basic classes of EPID dosimetry; EPID transit dosimetry, and EPID non-transit dosimetry. In non-transit dosimetry, planned irradiations are delivered with no patient in the beam path, whilst the signals from the EPID are acquired. The latter (transit dosimetry) also termed as *in vivo* dosimetry however involves acquisition of EPID signals as the radiation beam traverses through a patient.

Over the past decades, a number of EPIDs have been constructed and several studies have been conducted whilst utilizing EPIDS for dosimetric purposes. One of such early studies performed in the early 1990s (van Herk, 1991) involved the development and use of the scanning liquid-filled IC EPID by van Herk. The scanning liquid-filled IC EPID which had an active area of 32 × 32 $cm^2$ comprised an IC filled with an organic liquid (isooctane). Since then, several researchers have conducted various investigations on the dose response characteristics of the scanning liquid-filled IC EPID (Louwe et al., 2004; Mohammadi & Bezak, 2005; Tateoka et al., 2006).

One of the early studies was done by Boellaard et. al. in the mid-1990s (Boellaard et al., 1996). Boellaard et al. undertook a study on the scanning liquid-filled IC EPID by investigating the amount of build-up material needed for electron equilibrium (Boellaard et al., 1996). In their study, Boellaard et al. concluded that an extra thickness of 28 mm polystyrene was required when using a 25 MV beam. This extra thickness however increased the whole mass

of the EPID panel by an amount of 4.5 kg. As such, some artifacts were observed which resulted in the reduction of image quality.

In the early 1990s, a new type of EPID was developed for MV radiotherapy beams; the scintillation crystal-photodiode detector. The scintillation crystal-photodiode detector was developed at the Royal Marsden Hospital in the United Kingdom (UK) by Morton et al. (Morton et al., 1991), and is a linear scanning array imager. In 1996, the dosimetric properties of the scintillation crystal-photodiode detector was investigated by Hansen et al. (1996). In their study, they showed the linear response of the scintillation crystal-photodiode detector with doses.

While there are reports of dosimetric studies on scintillation crystal-photodiode EPIDs and on liquid filled IC EPIDs as stated earlier, there is very little on the relatively new amorphous silicon (aSi) based EPID systems. The amorphous silicon EPID (aSi EPID) comprises a scattering metal plate to produce Compton electrons and a phosphor layer to absorb the high energy electrons and emit light photons that are detected by the large-area photodiode array (as shown in Figure 4**)**. In operation, the Compton electrons are produced in the metal plate (usually made of copper). Light photons are then produced as the generated Compton electrons interact with the phosphor material which is usually made of gadolinium oxysulphide ($Gd_2O_2S$) and thallium-doped caesium iodide ($CsI:T_1$). The aSi EPID panel also embodies light sensor detector pixels with the composition of photodiodes and thin-film transistor (TFT) that are connected to the computer readouts. In the course of irradiations, the thin-film transistors are non-conducting, the light photons produced from the phosphor

material discharge the diodes. However, on computer readouts, the thin-film transistors become conducting, and hence recharge the diodes. The charging is done row by row, and the charge required to re-bias the diodes is proportional to the light reaching the photodiode (Mayles et al., 2007).

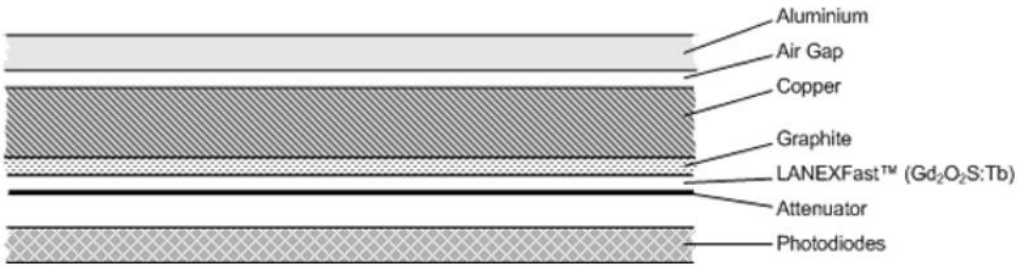


Figure 4: Schematic Diagram of the components of aSi EPID (Elekta, 2010)

In recent years, the aSi EPID, also known as the flat panel imager, has become most popular and common type of EPIDs, and is used worldwide by several radiotherapy centres (van Elmpt et al., 2008). The aSi EPID is currently available commercially with different manufacturing systems such as Elekta iView GT system, Siemens OptiVue system, and the Varian aSi PortalVision **(**aS500/aS1000) system (van Elmpt et al., 2008). With the new aSi EPID, the dosimetric properties of EPIDs have greatly been enhanced, as image read-out times are now faster. Few works have however been reported on dosimetric investigations of aSi EPIDs.

In 1998, Munro and Bouius (El-Mohri et al., 1999) performed a dosimetric investigation of a small aSi EPID of active area 96 × 96 $mm^2$. In their study, they measured the spatial resolution, signal-to-noise, glare and dose linearity characteristics of an aSi EPID with the presence of a phosphor layer in the EPID panel. The EPID configuration is considered as indirect aSi

configuration, as the radiation would have to interact with the phosphorous layer before reaching the photodiode detectors in the panel. They concluded that the sensitivity of the indirect EPID system was noticeably higher than the sensitivity of direct EPID system which had no phosphor layer in the panel (Munro & Bouius, 1998). A similar study was conducted by El-Mohri et al. (El-Mohri et al., 1999) by investigating dosimetric characteristics of an aSi EPID flat panel imager in two ways. The first was done with phosphor layer in the panel (indirect system), whilst the second was done without a phosphor layer in the panel (direct system). They also demonstrated that the sensitivity of the indirect EPID system had a higher sensitivity as compared to the results of the direct EPID system. However, their study showed that the direct system showed a dosimetric behaviour that was similar to data acquired with an IC, whilst the indirect system showed a vast difference in its measurements as compared to that of an IC readings.

In another study conducted by Greer and Popescu (Greer & Popescu, 2003), dosimetric studies were performed on an aSi EPID utilizing a 6 MV radiation beam and a continuous frame-averaging acquisition mode. The study concluded that aSi EPIDs showed promising results (with field size dependence of less than 5% relative to $d_{max)}$ by proving to be an efficient tool for verifying dose deliveries in radiotherapy.

The use of mathematical approaches for the determination of absorbed doses in EPID dosimetry have also been reported for several types of EPIDs by Pasma et. al. (1999). In their report, a kernel based deconvolution method was developed to convert pixel values of fluoroscopic EPID into absolute dose.

Additionally, a convolution based technique of calibration was developed and then modified for an aSi EPID for accurate verification of doses. The primary fluence map that was obtained using EPID, was convolved using a Monte Carlo based kernel to determine the absorbed dose in a homogeneous phantom.

In another study reported by Boellaard et al., (1997), a report was made for which a deconvolution algorithm was implemented to convert EPID pixel values to exit doses was made. However, although the algorithm proved accurate enough, the procedure involved requires much labour, making it unsuitable for use in daily radiotherapy routine works.

**Ionization Chamber (IC) Dosimetry**

On a fundamental level, any effect of ionizing radiation, could be utilized to obtain absorbed dose to a medium. The effects include ionization of gas molecules in the air-cavity chamber of an IC. An IC air cavity is usually enclosed by a layer of material known as chamber wall to provide electron equilibrium. The electrons are generated in the chamber wall, which subsequently enter the cavity, producing ionization effects. The ions produced in the air cavity are collected and read out through an electrometer.

Generally two different designs are used in clinical dosimetry to form these two electrodes: parallel or cylindrical. A plane parallel chamber consists of two separated electrodes parallel to each other and perpendicular to the primary beam direction, leaving an air-filled gap in between, which serves as the sensitive volume (Mayles et al., 2007). This type of chamber is usually recommended for high energy electron dosimetry. In photon dosimetry,

cylindrically shaped ICs usually referred as thimble chambers are utilized. They comprise a cylindrical air cavity with a central electrode inside, encompassed by a cylindrical wall perpendicular to the direction of primary beam (Abaza, 2019). In this study, a farmer-type IC was utilized throughout the investigations.

**Thermoluminescent Dosimetry**

Thermoluminescent dosimetry is centered on imperfections in crystal lattice structures and their capacity to capture electrons that are discharged by ionizing radiation. The most regularly utilized crystal lattice for dosimetric purposes is lithium fluoride, doped with titanium and magnesium (LiF:Mg,Ti) (OzRadOnc, 2017b).

Typically, personal dosimeters make use of calcium sulfate crystals which are more sensitive to lower doses. As ionizing radiation interacts with the crystal, electrons may be ejected from the structure. These electrons are 'trapped' by the magnesium impurity, and the number of trapped electrons is proportional to the amount of ionizing radiation that is absorbed in the crystal. The electron may remain trapped over long period of time (OzRadOnc, 2017b).

As the crystal gets heated, electrons are ejected from the magnesium impurity, and are absorbed by the titanium impurity. If the electrons are absorbed by the titanium, they release excess energies in the form of light photon, which are captured by a photoamplifier. The photoamplifier amplifies the energy in the light photon to readable levels, which are displayed by an electrometer. The TLD has the ability to calculate the amount of light emitted during the heating of the crystal. The calculated values are then related to known

values to determine the absorbed dose received by the TLD (OzRadOnc, 2017b).

**Radiotherapy Treatment Planning**

Treatment planning emerged from the early use of radiation for therapy, and has a bedrock of the present-day planning techniques that rely on complex computer modelling of the dose distribution from patient data and external radiation beam parameters. Treatment planning has its ultimate aim of translating the therapeutic requirements of the oncologist into a set of treatment instructions that would enable the patient to be treated accurately. Here, the treatment plan does not only provide a set of instructions for the radiographer but also provides information on dose distribution.

**Treatment Verification**

Treatment verification has been an essential part of the radiotherapy treatment procedure. With the increasing complex treatment techniques (such as 3D conformal radiotherapy, IMRT, etc.) emerging, treatment verification plays a vital role in ensuring that the ultimate aim of radiotherapy is achieved. In this verification process, both geometric and dosimetric verification could be performed. Traditionally, treatment verification techniques have relied on the use of two-dimensional (2D) images acquired using portal film and more recently the use of EPID, at MV energies (Lemoigne & Caner, 2007).

**Modelling**

*Mathematical Modelling*

Scientifically, the relationship between various parameters and variables are best described with the help of mathematical formulae. These mathematical formulae plainly set up relationships between different parameters, and are referred to as models to express relationships (Barbosa, 2003). In general, mathematical models can take many forms, and depict a system utilizing mathematical concepts and language to facilitate proper explanation of a system, or to examine the effects of different components and to make predictions on patterns of behavior .

In many cases, the quality of a scientific field relies on how well the mathematical models developed on the theoretical side agree with results of repeatable experimental measurements. Lack of agreement between theoretical mathematical models and experimental measurements often leads to important advances as better theories are developed (Barbosa, 2003; Marion et al., 2008).

Nakano et al. (2013) define a mathematical model as a triplet (*S*, *Q*, *M*) where *S* is a system, *Q* is a question relating to *S*, and *M* is a set of mathematical statements $M = \{1, 2, \ldots, n\}$ which can be used to answer *Q* (Nakano et al., 2013). Suppose, for instance, that *S* is the set of natural numbers and our question *Q* relating to *S* is whether there are infinitely many prime numbers or not. Then, a set (*S*, *Q*, *M*) is a mathematical model in the sense that if *M* contains the statement "There are infinitely many prime numbers" along with other statements which prove this statement. In this sense, the entire mathematical theory can be viewed as a collection of mathematical models (Nakano et al., 2013).

*Modelling Procedures and Stages*

The modelling procedure could be divided into four general classification of activities; building, studying, testing and use (Barbosa, 2003). Any defects found at the studying and testing stages are corrected by returning to the building stage. Moreover Barbosa reports that, in the modelling process, if any progressions are made to the model, then studying and testing stages must be repeated. In 5, a pictorial portrayal of the stages of modelling is shown.

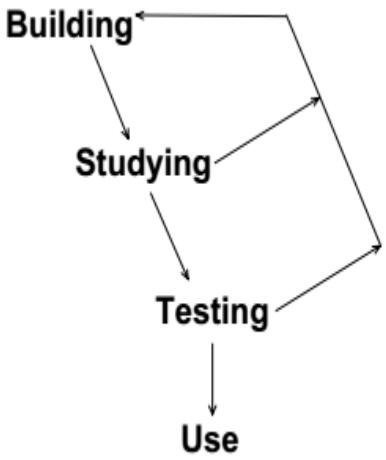


Figure 5: A pictorial representation of potential routes through the stages of modelling (Barbosa, 2003).

**Chapter Summary**

In Chapter Two, previous studies done to overcome the dosimetric challenges of EPID have been documented. The chapter reported that these previous studies have revealed several methods that have been implemented over the past years to determine exact delivered radiation doses to patients during radiation treatments. The studies showed that these methods are generally labour-intensive, requiring much time to execute, and hence are not

easily applicable in the daily routine radiotherapy procedure. Additionally, the chapter provided an insight of the physics of portal dosimetry, and all dosimetric devices used in this work. It further briefly explained the concept of mathematical modelling, and indicated a recommended 5% accuracy of dose delivery to patients (IAEA, 2013; Menzel, 2010).

# CHAPTER THREE

# MATERIALS AND METHODS

## Introduction

This chapter gives significant account on the materials and the techniques used to obtain the transit dosimetric model in this work. It begins by writing the materials and methods that were implemented to study the reliance of EPID signal on varying doses, radiation treatment field sizes, patient thicknesses, and the treatment couch. Furthermore, it incorporates a discussion of the various processes and protocols used to obtain doses to the isocentre of a beam in a phantom utilizing the Farmer-type IC. It includes modeling techniques using the Minitab Statistical tool v18.1, C++ and Visual Basic programming environment. The chapter further provides techniques for evaluating the developed dosimetric model, to ascertain its clinical feasibly. It ends with an information on the limitations of this work (during and after the measurements), and a discussion on the clinical feasibility of the transit dosimetric model obtained.

## Materials

The measurements and modeling requirements were done with appropriate materials and procedures. The details of the Elekta Synergy Platform LINAC machines utilized are exhibited in Table 1.

**Table 1: Specifications of Elekta Synergy Platform LINAC machine at SGMC.**

| Machine | Model | Manufacturer | Energy Range |
|---|---|---|---|
| LINAC | Synergy | Elekta | • 6 and 15 MV Photon Energies<br>• 6, 10 and 15 MeV Electron Energies |

Source: Field Work, 2015

**Treatment unit and setup**

All radiotherapy measurements in this study were obtained with an Elekta Synergy Platform LINAC (Figure 6) equipped with an amorphous silicon flat panel-type imager (aSi EPID). The LINAC is calibrated to produce 1 cGy absorbed dose to water per monitor unit (MU), at a 10 cm depth along the central axis in isocentric reference conditions, for a field size area of 10 cm × 10 cm.

The aSi EPID panel mounted on a robotic arm at a constant source to EPID distance (SED) of 159 cm, comprises an image detector unit with an active MV detector area of 41 x 41 $cm^2$ (approximately 26 × 26 $cm^2$ at isocentre ) and a resolution of 1024 x 1024 16-bit pixels images. It has a 1 mm Cu layer to serve two purposes; to act as a buildup layer converting high energy photons to secondary electrons, and to filter out contamination electrons from the head of the LINAC treatment unit. Additionally, the aSi EPID panel has a phosphor screen layer and a layer of hydrogenated aSi:H photodiode array (Larry, 2002; Rottmann et al., 2016; Seng, 2008). During patient irradiations, the transit MeV photon beam first hits the copper layer, and is converted from MeV photons into X-ray photons through Compton Effect with the emission of Compton electrons. The X-ray photons are

subsequently converted into visible light in the phosphor screen layer, and in turn, electron-hole pairs are produced in the photodiode layer. The number of electron-hole pairs produced is proportional to the intensity of the light emitted from the phosphor in the particular region close to the pixel. The electron-hole pairs are stored in the photodiodes, and read out as current. Each photodiode is connected to a tin film transistor (TFT), and the electron-hole pair charges are converted to digital format by analogue to digital converters (ADCs). The digital data are transmitted to the data acquisition unit. The acquisition unit utilizes the peripheral component interconnect (PCI) bus for direct image acquisition into the PCI's main memory and imager control functions. The acquired images are displayed on PC monitor (Agarwal et al., 2017).

LINACs produce clinical electron and photon beams precisely shaped by the MLC. The Elekta Synergy Platform LINAC used in this study produces photon energies of 6 and 15 MV, and produces electrons with energies of 6, 10 and 15 MeV.

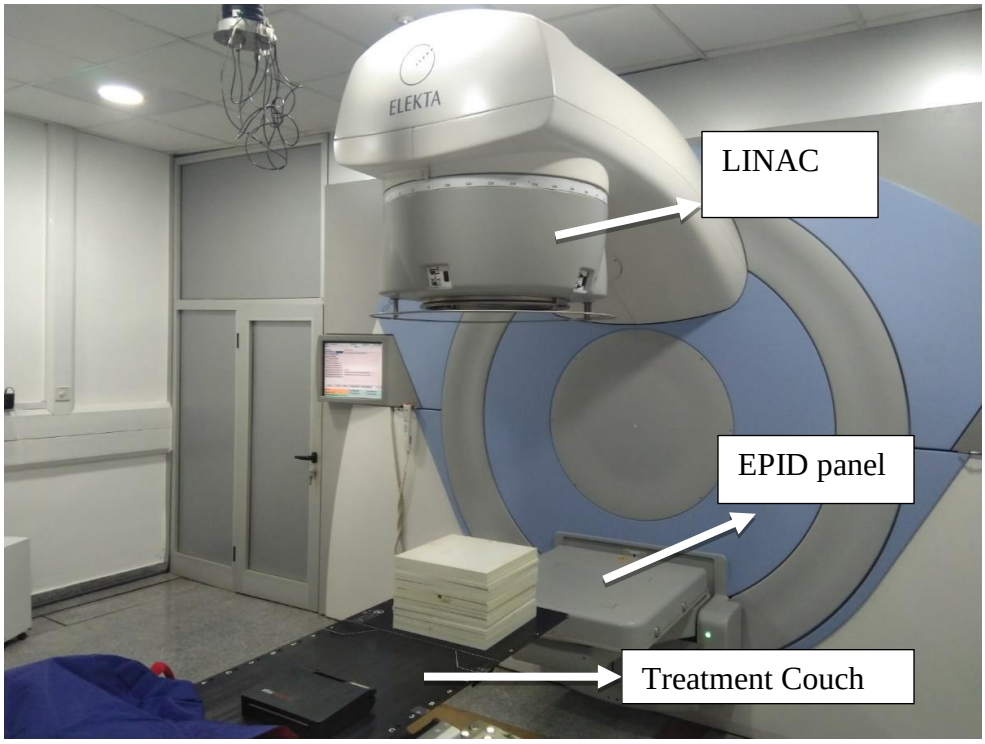


Figure 6: The Elekta Synergy Platform LINAC at the SGMC, equipped with EPID (manufactured by Elekta) (Field work, 2017)

In this work, only 6 MV and 15 MV photon beams were used. The Elekta LINAC is equipped with MLCs with round leaf ends, and 1 cm leaf width at the isocentre. All irradiations were done at a gantry angle of 0º (International Electrotechnical Commission (IEC) scale) and a 0º collimator position. In Figure 6**,** the Elekta Synergy Platform LINAC at the SGMC, equipped with EPID manufactured by Elekta is shown. The LINAC produces clinical electron and photon beams precisely shaped by the MLC.

**Image acquisition**

All EPID images in Tagged Image File Format (TIFF) were obtained in integrated mode using iViewGT™ software (Figure 7) combined with the MOSAIQ system (Elekta Medical Systems, Sunnyvale, CA). This system provides

synchronization between the EPID detector and the LINAC machine, i.e., image data are read between the radiation pulses. Additionally, the system automatically applies a set of corrections to all images measured, including offset and gain correction as well as a bad pixel map correction.

The iViewGT™ provides 2-dimensional MV planar images in few seconds, and helps in achieving excellent clearance and superior field of view (Elekta, 2010).

Data analysis was done with the aid of a java-based image processing program, IMAGEJ software (Figure 8), Minitab statistical software and Microsoft excel. Images were acquired by placing the EPID in the central position with respect to the beam.

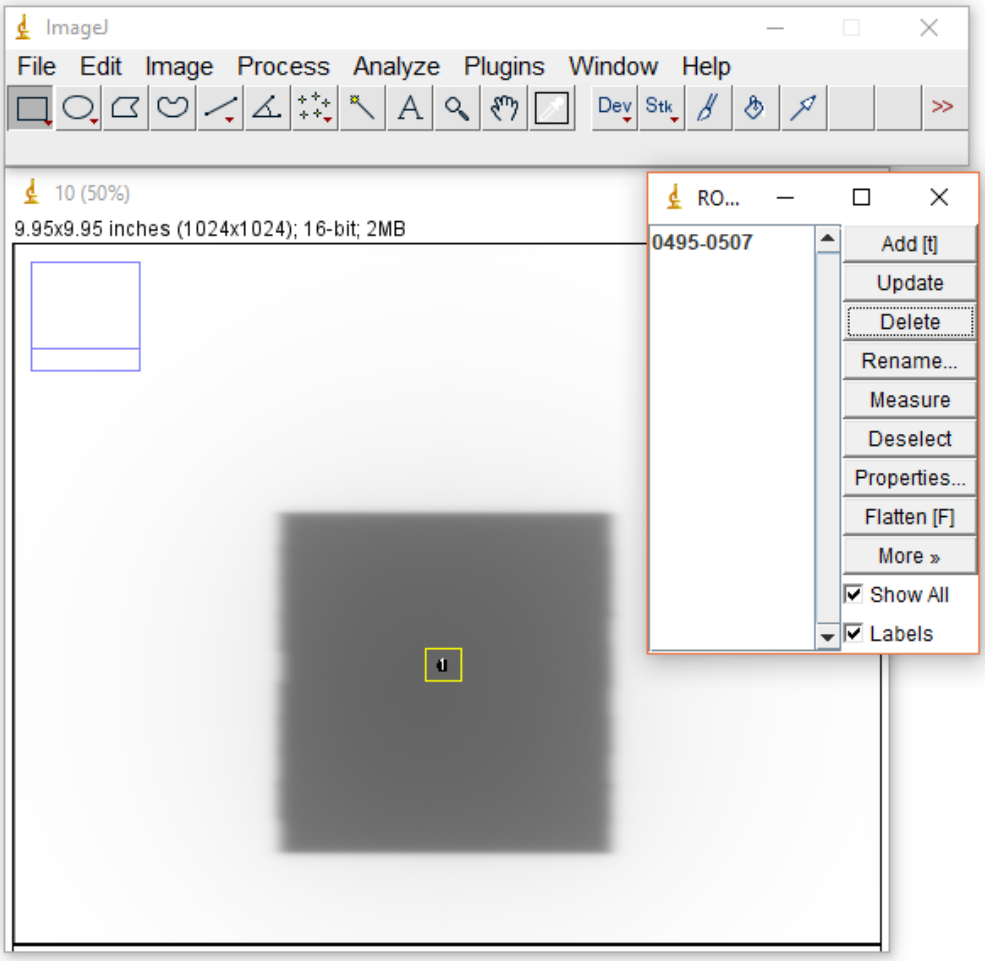


Figure 9: Image J software interface with loaded image (Field data, 2017)

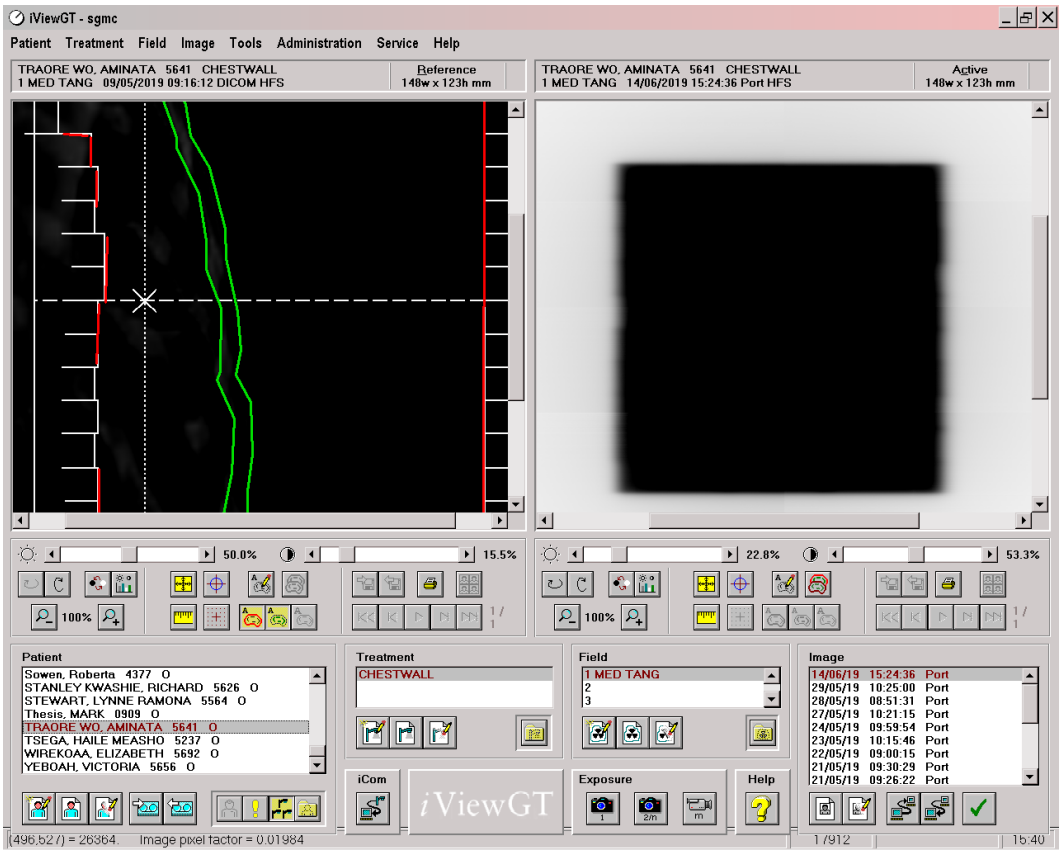


Figure 10: EPID iViewGT™ platform with loaded image at the SGMC (Field Work, 2017)

**Electrometer and IC**

All dosimetric measurements were done with the Farmer-Type PTW IC (IBA 30010). The Farmer-Type PTW IC 30010 was connected to the PTW-UNIDOS electrometer in phantom slabs made of metaplex, and all measurements were performed in photon radiation beams produced by the Elekta Synergy Platform Accelerator.

The Farmer-type IC IBA 30010 **(**Figure 11**)** used in combination with a PTW, UNIDOS electrometer (Figure 12) allows to take absolute point dose measurement. It has an active measuring volume of 0.6 $cm^3$, active length of 23.1

mm, an inner diameter of 6.2 mm, and is intended for absolute photon and electron dosimetry. It is made of a graphite wall material with a protective acrylic cover, and the electrode is made of aluminum. Its nominal photon energy range is from 30 kV to 50 MV (PTW, 2016).


Figure 11: Farmer-Type PTW IC 30010 used in this study for reference measurements of dose in the PMMA solid water phantom (Field Work, 2017)


Figure 12: PTW-UNIDOS Electrometer used in this study for reference measurements of dose in the PMMA solid water phantom (Field

**Thermoluminescent Dosimeters**

In this study, the LiF:Mg, Ti harshaw TLD ( Figure 13) was used throughout to evaluate the transit dosimetry model (developed in this study). The LiF:Mg,Ti harshaw TLD Material consists of Lithium Fluoride, LiF which has a high high sensitivity. Additionally, the TLD has an excellent energy response due to the reason that, LiF is highly tissue equivalent. The LiF:Mg, Ti harshaw TLD measures photon radiation energies > 5 keV and beta energies > 70 keV. Moreover, it

measures doses of 10 μGy – 1 Gy with linearity of 5%, and 1 Gy to 100 Gy with supralinear property above 1 Gy (Harshaw, 2007).


Figure 13: LiF:Mg, Ti TLDs used for transit dosimetry model evaluation (Field Work, 2018)

**Performance Assessment of SGMC LINAC Facility**

Prior to undertaking all measurements in this study, it was essential to test the level of performance of the systems and procedures at the SGMC cancer facility, as any systematic error would be translated into this study, if not resolved. The tests involved mechanical and safety checks. These measurements ensured that the system was working as intended. In that capacity, several QC tests were performed on the LINAC facility.

In these tests, the actual quality performance of the Elekta Synergy Platform LINAC was measured and compared with existing standards. This was to ensure and guarantee that quality requirements of the LINAC facility at the SGMC were met, and in compliance with TG 142 accepted codes of practice (Klein et al., 2009). Additionally, it was to adjust and correct performances if the prerequisites were found not to have been met.

**IC Correction for Pressure and Temperature**

The calibration factor for an IC is legitimate just for the reference conditions which apply to the calibration. Any deviation from the reference conditions when utilizing the IC in the radiation beam ought to be corrected for the suitable correction factor. This suggests the IC utilized in this work, is open to ambient air, and the mass of air in the cavity volume is liable to barometrical varieties. Hence, all dosimetric readings obtained with the Farmer-type IC IBA 30010 were corrected for temperature and pressure. The correction factor was determined by equation 7.

$$k_{TP} = \frac{(273.2 + T)}{(273.2 + T_0)} \times \frac{P_0}{P} \qquad (7)$$

Equation 7 was applied to convert the cavity air mass to the reference conditions. P and T are the cavity air pressure and temperature at the time of the measurements, and $P_0$ and $T_0$ are the reference values at the time of calibration of the Farmer-type IC IBA 30010 (101.33 kPa and 20 ˚C**).** Figure 14 and Figure *15* show the Testo 925 thermometer and GE Druck barometer PACE 1000 respectively used to measure temperature and pressure respectively in this study to

determine temperature-pressure correction factors for absolute dosimetry. The measuring range of the thermometer is from -50 to 1000 degrees C (Testo, 2017). GE Druck barometer PACE 1000 records a pressure range up to 1000 bar (14500 psi/100 MPa), with a precision choice up to 0.005% FS (Druck, 2011).


Figure 14: Testo 925 Thermometer used in this study (Field Work, 2017)


Figure 15: GE Druck Barometer PACE 1000 used in this study (Field Work, 2017)

**Slab Phantom Studies**

The PMMA solid water phantom slabs (Figure 14) were used throughout this study. The PMMA slab water phantom has dimensions of 30 cm×30 cm, and is designed for range of 70 kV to 50 MV photon energies, and electron energies of 1 MeV to 50 MeV (PTW, 2016c). Each slab has a thickness of 1 cm.

Figure 16*:* 30 cm × 30 cm PMMA phantom slabs (manufactured by PTW) used in this study. Each slab has a thickness of 1 cm (Field Work, 2017)

**Treatment planning system**

All treatment plans were done with Ocentra Masterplan TPS. CT images were taken for the specific localization of the PMMA slab water phantom and sent to the treatment planning room (TPR), and similar treatment plans were generated using the Ocentra Masterplan TPS as shown in Figure 17**.** The treatment for that plan was then delivered to the phantom, and the "*in vivo*" measurement was performed. In this study, the dose measurements were performed in the PMMA phantom along the central beam axis, at the isocentre in the phantom using an IC placed at the isocentre.

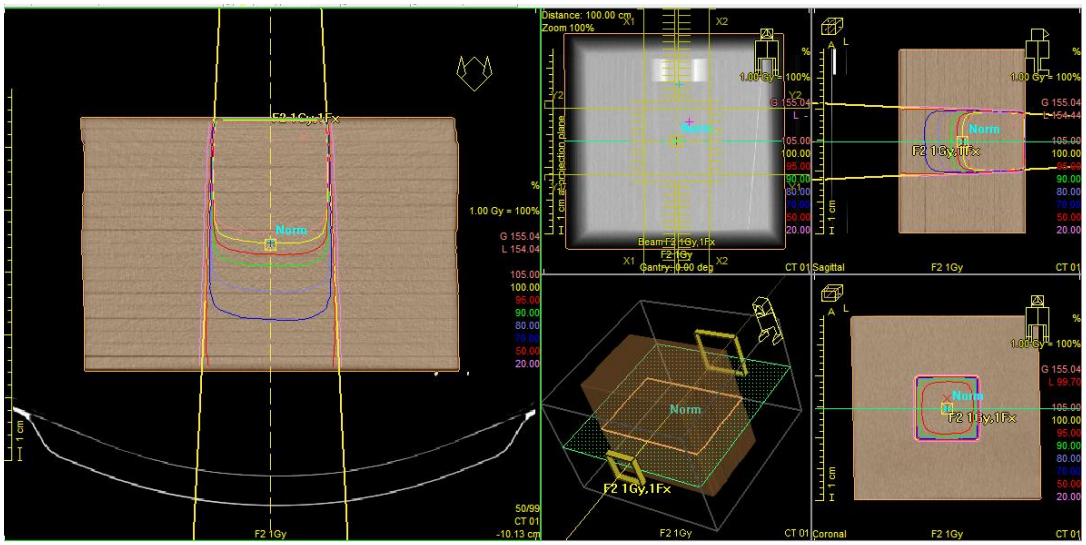


Figure 17: Treatment plan of the 20 cm thickness PMMA phantom slabs generated using the Ocentra Masterplan TPS in this study (Field Work, 2017)

**Investigation of EPID response to different doses**

Understanding the relationship between the EPID output and the actual dose delivered is key to the development of the transit dosimetry model. The relation between the dose measured in the PMMA phantom and the EPID signal registered during phantom irradiation was investigated using clinically applicable range of doses per fraction at SGMC.

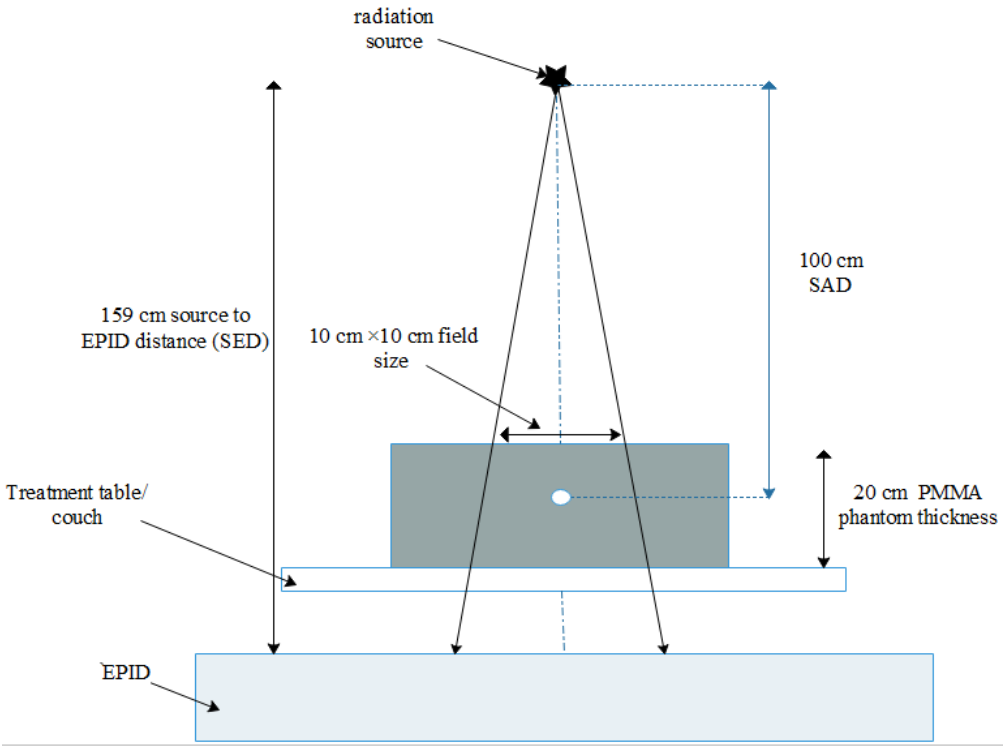


Figure 18: A schematic diagram of the experimental setup for measurements in the test of EPID response to different doses in this study (Field Work, 2017)

In this investigation, CT images were taken for the specific localization of the phantom and sent to the treatment planning room (TPR), and a treatment plan (Figure 17) was generated using the Ocentra Masterplan TPS.

The treatment for the plan was then delivered to the phantom. The plan was optimized for a 6 MV photon beam energy, and all irradiations in the treatment room were done with a photon energy of 6 MV. Figure 18 provides a schematic diagram of the experimental treatment setup in this test.

All EPID measurements were obtained at the isocentre of the beam through irradiation of a 20 cm thickness of PMMA slab water phantom with doses ranging from 50 cGy to 300 cGy for 10 cm×10 cm field size at 159 cm SED, and an isocentre depth of 10 cm. A 100 cm source to axis distance (SAD) technique was

employed in all irradiations. Mean grey scale pixel values at the centre of the field were measured and a graph of mean grey scale pixel value was plotted against delivered dose.

The experiment was repeated with the Farmer-Type PTW IC, under the same conditions as above. The IC measurements were performed at a similar depth of 10 cm in the PMMA water phantom for the same setup above. All setup conditions for the EPID measurements were maintained for all IC measurements. The effective point of measurement was at the isocentre of at 10 cm depth in the PMMA phantom.

**EPID Dependence on Different Field Sizes.**

For this test, the dependence of EPID signal as a function of radiation field size was investigated. A 100 cm SAD technique was employed, and a constant dose of 100 monitor units (MU) was delivered throughout this investigation. A 6 MV photon beam energy was used, and a varying square field size at the isocentre ranging from 5 x 5 to 25 x 25 $cm^2$ was tested. All irradiations were done at a depth of 10 cm in a 30 cm × 30 cm solid water phantom of 20 cm thickness.

The EPID panel was positioned at a fixed 159 cm position (SED) from the source, and for each irradiation, EPID mean grey scale pixel values at the beam central axis were acquired for each field size. It is worthwhile to define the grey scale pixel value as the single sample representing only an amount of light at the central axis of the beam.

All measurements were repeated for the Farmer-Type PTW IC. The IC measurements were performed at a similar depth of 10 cm in the PMMA water

phantom for the same setup above. The effective point of measurement was at the isocentre at 10 cm depth in the PMMA phantom. The IC readings were then corrected for temperature and pressure. Figure 19 shows a schematic diagram of the experimental setup used.

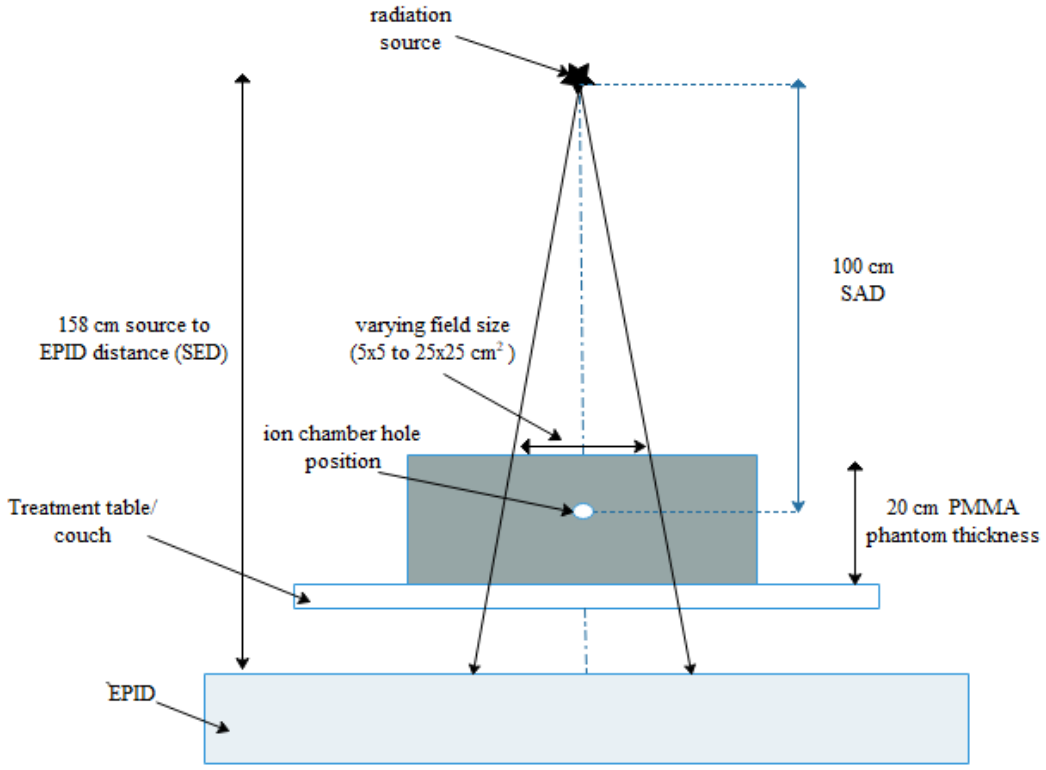


Figure 19: A schematic diagram of the experimental setup for measurements in the test of EPID response to field size (Field Work, 2017)

Both sets of measurements (IC and EPID) were normalized to the 10 cm ×10 cm field size values (at the isocentre). The normalization of measured values to 10×10 cm² was done by dividing each measured value by the referenced value obtained with 10×10 cm² radiation field size. This was to ensure traceability of measurements to the IAEA standard protocol for radiotherapy dosimetry, TRS-398 (IAEA, 2005). The normalized central axis reading of the EPID was compared to

those measured by the IC for the particular field size used. Field size correction factors of the EPID were then calculated for each field size, and a graph of radiation field size side ($FS_x$) was plotted against the corresponding field size correction factor.

**EPID dependence on different phantom/absorbent thicknesses**

According to literature, EPID signal is dependent on the patient or phantom thickness (Herman et al., 2001; Slosarek et al., 2010; van Elmpt et al., 2008). To develop the transit model of this work, it was important to investigate the extent of correlation between the radiation absorption in phantom and the corresponding EPID signal. Again, in order to employ the EPID for *in vivo* dosimetry, it is essential to investigate the dependence of EPID signal on thickness of the absorbing material.

PMMA solid water phantom slabs were placed on the therapeutic table/couch perpendicularly to the beam axis. The source to axis distance (100 cm SAD) irradiation technique was employed in this investigation. A constant dose of 10 MU and a 10×10 $cm^2$ field size set at the isocentre of the beam, were used throughout this test. Varying layers of PMMA water phantom slabs ranging from 4 cm to 20 cm water phantom thickness with an increment of 2 cm were used, as shown in Figure 20.

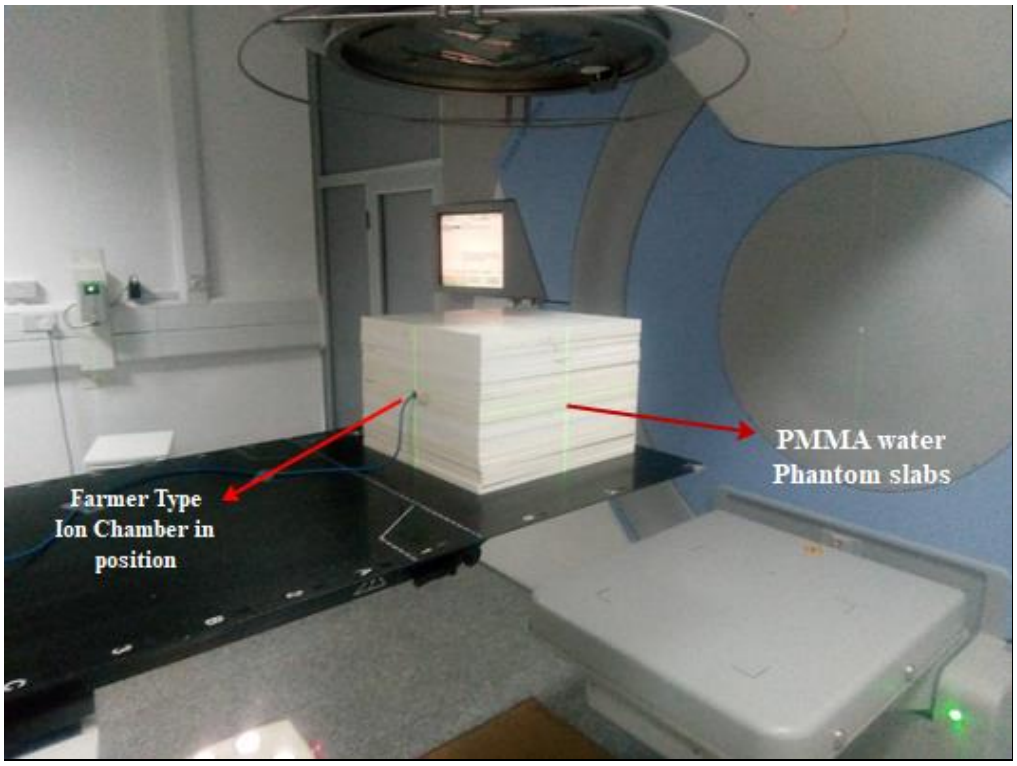


Figure 20*:* Experimental Setup of PMMA phantom slabs (with the Farmer Type IC in position) used in investigating the dependence of EPID signal on phantom thickness (Field Work, 2017)

All measurements were performed with a photon beam of 6 MV. The EPID panel was positioned at a fixed 159.0 cm position (SED) from the source, and for each patient thickness irradiated, mean EPID grey scale pixel values were acquired at the central axis of the beam.

The same setup was again repeated for the farmer type IC measurements, and for each phantom thickness (4 cm to 20 cm), corrected IC readings were compared with EPID measurement obtained. The comparison of EPID measurements with IC readings, was to ensure traceability of EPID measurements to the IAEA standard protocol for radiotherapy dosimetry, TRS 398 (IAEA, 2005) which employed the use of IC in all dosimetric calibrations.

**Therapeutic Table/ Treatment Couch Effect on EPID signal**

The purpose of this study was to understand and make corrections for the dosimetric effect of the treatment table (Figure 21) or couch on EPID signal. A study of couch attenuation was done with a photon energy of 6 MV using a 10 × 10 $cm^2$ radiation field size set at the isocentre of the radiation beam. In this study, the treatment couch was positioned perpendicularly to the beam at 110 cm source to couch distance (SCD), and the irradiation was made without a phantom in the radiation beam. EPID image was then obtained by placing EPID panel at a fixed distance of 159 cm from the source (SED) during the irradiation.

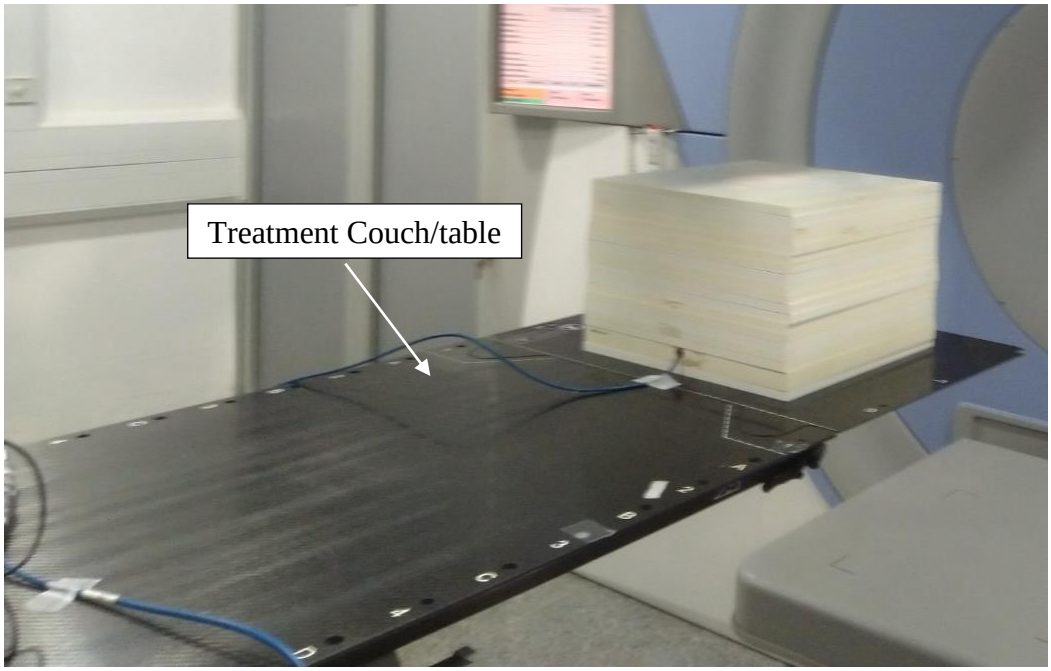


Figure 22: Treatment Couch used to support patients at the SGMC (Field Work, 2017).

The setup was repeated twice for the same reference conditions (6 MV photon beam energy and 10×10 $cm^2$ radiation field size set at the isocentre of the radiation beam). In this case, the irradiation was done without a treatment couch in

the beam. EPID image was then obtained by positioning the EPID panel at a fixed 159 cm SED. Both signals obtained with and without couch were analyzed for correction.

**Pixel Scaling Factor**

In acquiring EPID images in iViewGT™, pixel values are automatically re-normalized before saving the image data to the database (Elekta, 2010b). This implies that all EPID images will bear the same optical density (OD) for all different doses. During the acquisition period, each image has its own unique pixel scaling factor (PSF) saved in the database. Hence, the originally accumulated pixel value ($S_{EPID}$) was determined by dividing the recorded pixel value by PSF (as indicated in equation 8).

$$S_{EPID} = \frac{Raw\ EPID\ Pixel\ \ Value}{PSF} \tag{8}$$

**Statistical Modeling Process**

In this section, the statistical tools that were utilized to achieve all the essential investigations of this study are described. It additionally incorporates choices and decisions that were implemented to reach reasonable inferences. Moreover, it likewise represents different techniques that were used to obtain the transit dosimetry model.

**Basic Statistical Analysis**

All statistical analyses of data were performed utilizing Minitab 18.1 statistical tool. This included the utilization of multivariate methods for analyses of

the data. The Analysis of Variance (ANOVA) was utilized to analyze the statistically significant differences between the means of EPID signal measurements and their corresponding IC measurements. ANOVA was utilized to determine the extent of correlation between EPID signal measurements and their corresponding absorbed doses, radiation field sizes and absorbent thicknesses. Thus, both ANOVA correlation and regression analyses were performed by contrasting the mean and p-values. Correlation and major regression analyses of ANOVA were additionally completed to determine the relationship that exists among the radiotherapy parameters and their corresponding correction factors.

Statistically, the modelling process depended on linear and polynomial approaches for demonstrating the connection between scalar dependent variables and independent variables. The connections between the parameters were modeled by utilizing linear predictor functions whose model parameters were derived from the experimental data. The plots depended on residual plots to check the goodness-of-fit in the regression analysis.

The residual plots comprise four diagrams which comprised graphs that were utilized to check skewness of the experimental data. Initially, the histograms of residuals were utilized to determine whether the data are skewed, and were also used to check for any anomalies in the data.

Additionally, the plots of residuals versus fits were also used to detect non-linearity, unequal error variances, and outliers. Also, plots of residuals versus order of data was employed to check if there was any correlation between the error terms that are near each other in the sequence. Each model has elements such as the model

equation, the predictor and the p value. A small p-value (ordinarily < 0.01) shows solid proof against the null hypothesis, consequently leading to the rejection of the null hypothesis.

**Choice and Conclusion Principle**

In order to make a good conclusion on all the models of this study, the null hypothesis rule was utilized. A significance level of 0.05 was utilized during all the statistical hypothesis tests in this study. The significance level of 0.05 indicates a 5% risk of concluding that the data do not follow a normal distribution when they actually do follow a normal distribution.

The null hypothesis was rejected if the p-value was less than 5% significance level ($p < 0.05$), accepting the alternative hypothesis. However, if the significance level is above the 5% value ($p > 0.05$), the null hypothesis is not rejected, and the alternative hypothesis cannot be accepted.

In light of this standard decision rule, comparative study on EPID reliance on different radiotherapy factors such as patient thickness variations, field size variations, dose variations were acquired.

**Dose Conversion Modeling**

A dose conversion model for transit dosimetry was developed using the Microsoft Visual C++ (MSVC) and visual basics programming tool. MSVC is an integrated development environment (IDE) product from Microsoft for the C, C++, and C++/CLI programming languages. Likewise, the visual basic is a computer programming language which provides dot net framework to assist in design in graphical user interface (GUI).

The modelling was done using MSVC (version 2016) which combines the features of both high level and low level languages. It could be used for low-level programming, such as scripting for drivers and kernels and it also supports functions for high level programming languages, such as scripting for software applications etc. Globally, variables were declared to store inputs from user (Nakano et al., 2013). These variables make up the formula for calculating the measured dose. Each variable is mapped/assigned to a textbox that accepts inputs from the user. When a value is entered in any of the textboxes, the value is parsed to the variable assigned to the textbox and then used by the formula to calculate the measured dose. Figure 23 provide a pictorial view of the whole C++ MSVC modelling procedure for developing the GUI in this study.

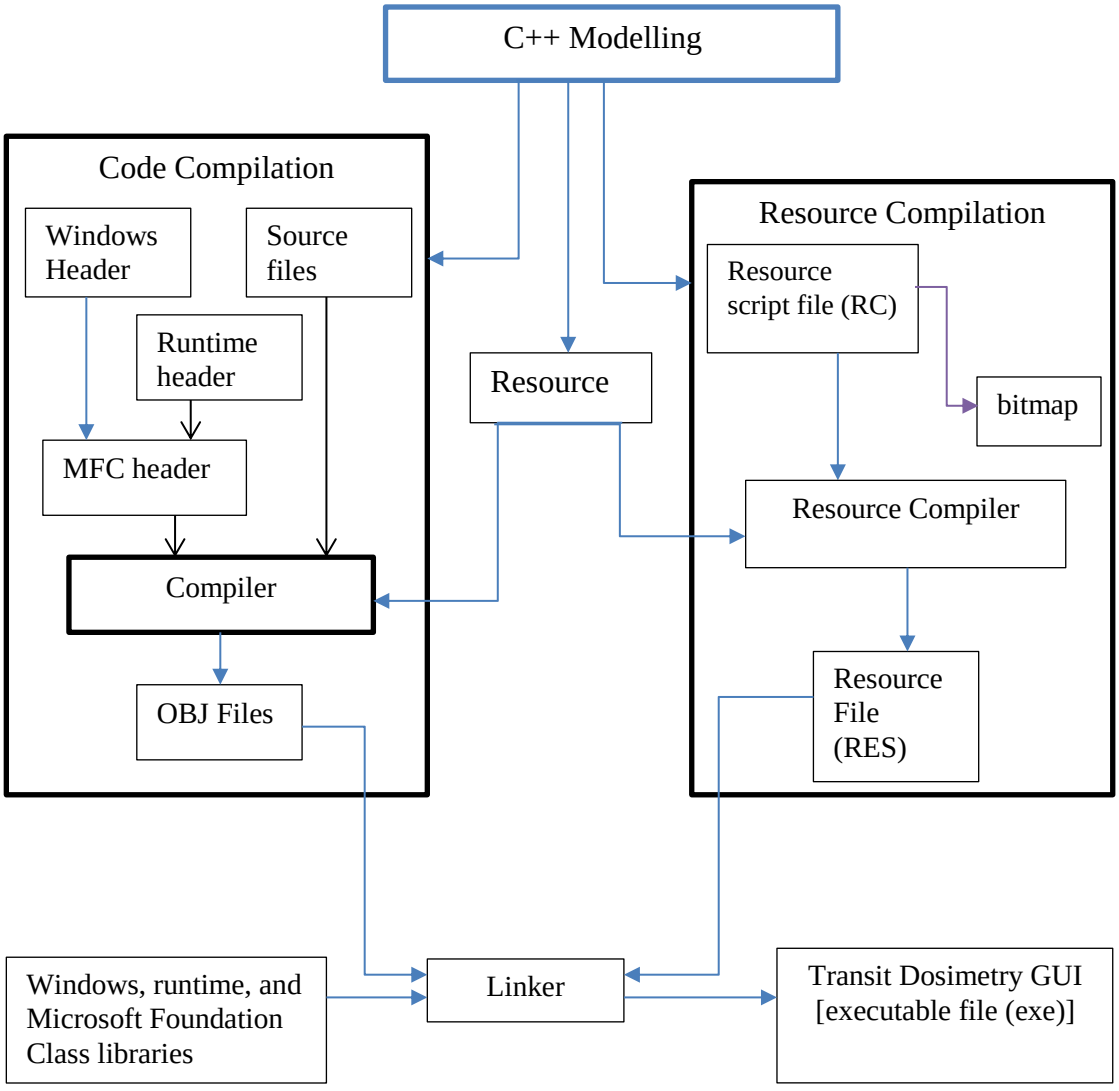


Figure 23: The Visual C++ GUI development procedure in this study (Field data, 2018).

An HP Pavilion 15-au063nr laptop was used to write the programming code, and for all modelling in this study. The HP Pavilion 15-au063nr laptop which was manufactured by HP has a display screen size of 15.6", a storage capacity of 1 terabyte, and operates on windows 10 Home 64-bit Edition operating system.

Additionally, the laptop has an inbuilt Intel Core i7-6500U Dual-Core processor 2.5 GHz with a maximum turbo speed of 3.1 GHz. Moreover the HP Pavilion 15-au063nr laptop runs on installed 12 GB random access memory (RAM) with a rated speed of 2133 MHz

The dose conversion model was developed in the form of a GUI application. The GUI is a type of UI that enables clients to connect with electronic gadgets through graphical symbols and visual indicators (Wikipedia, 2017). In the GUI, the windowing system serves as a front end of the programme to the end-user from often confusing syntax and vocabulary of the programming language. The GUI utilizes the graphics on a bitmapped video display, and becomes a source of input for the user. The user therefore interacts with the GUI, and receives output in the form of a message.

The dose conversion modeling was done through a coding process where a code was written in vb.net and C++ programming languages to develop a software for integration with the image j application platform for clinical application. This was done by converting the mathematical representation obtained through the minitab statistical tool, into a GUI based design software in a text-based user interface which is applicable in a clinical environment. This served as an input interface for radiotherapists and medical physicists to verify real-time doses to targets inside the patients. All mathematical model equations, designed as GUI based software are presented in Chapter Four.

**Evaluation of the Developed Dose Conversion model for actual treatment verification**

The dose conversion model developed in this study was evaluated using an anthropomorphic phantom (The Phantom Laboratory, NY, USA), shown in Figure 24.

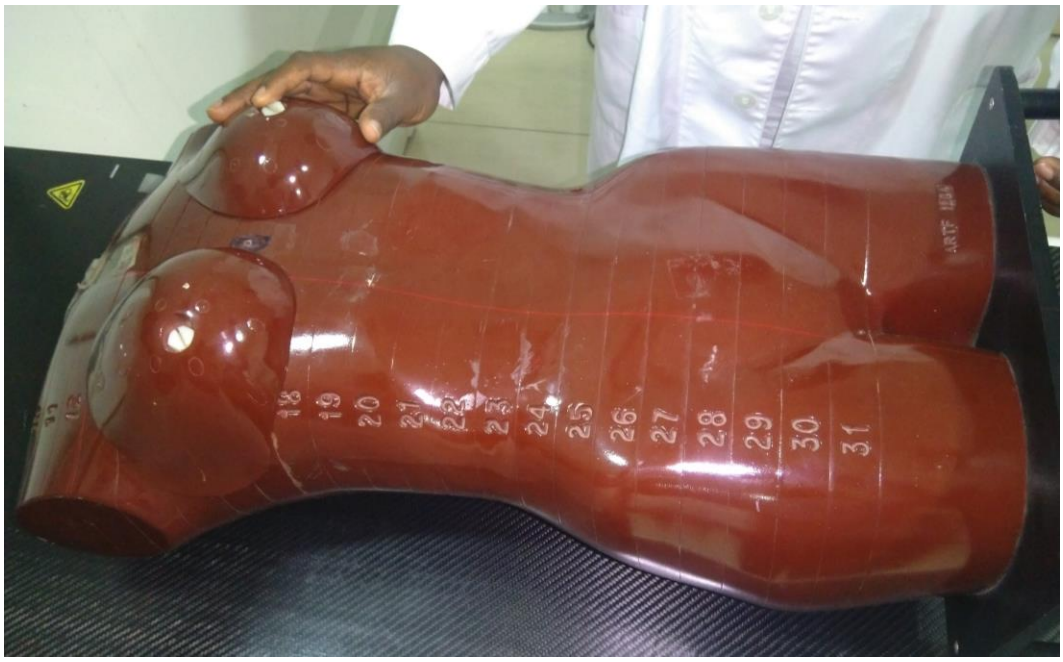


Figure 24: Anthropomorphic phantom at the SGMC used in this study (Field Work, 2018)

CT images (Figure 27) of the anthropomorphic phantom were acquired for pelvic region using Somatom Emotion CT Scanner (Figure 25). The CT images were then sent to the treatment planning room (TPR), and treatment plans (Figure 26 and Figure 28, and Appendix B) were generated using the Ocentra Masterplan TPS. Six treatment plans were prepared for the verification of the dose conversion model, the treatment for that plan was delivered to the anthropomorphic phantom in the pelvic region.


Figure 25: Somatom Emotion CT scanner used for this study at SGMC (Field Work, 2018**)**

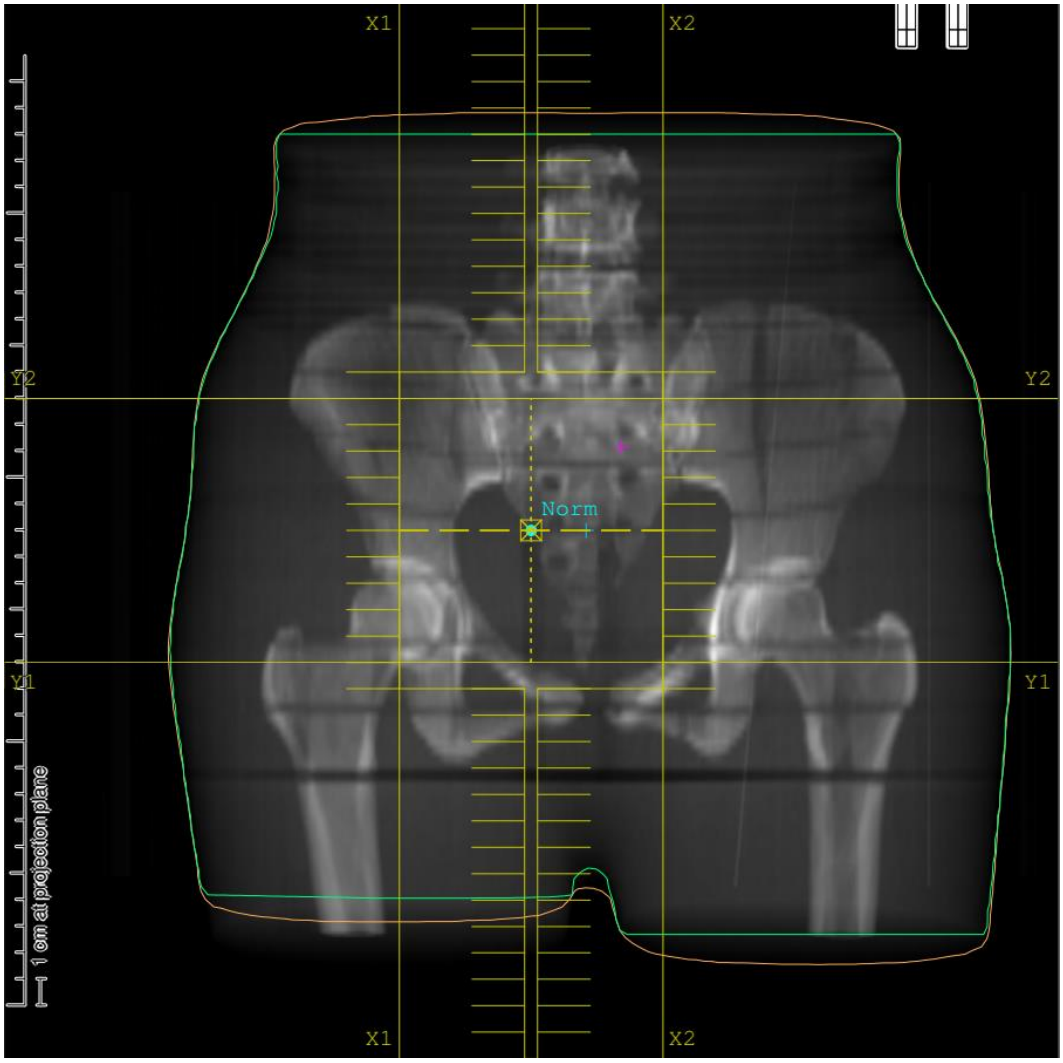


Figure 26: Pelvis treatment plan of the anthropomorphic phantom produced using Ocentra Masterplan TPS (Field Data, 2018)

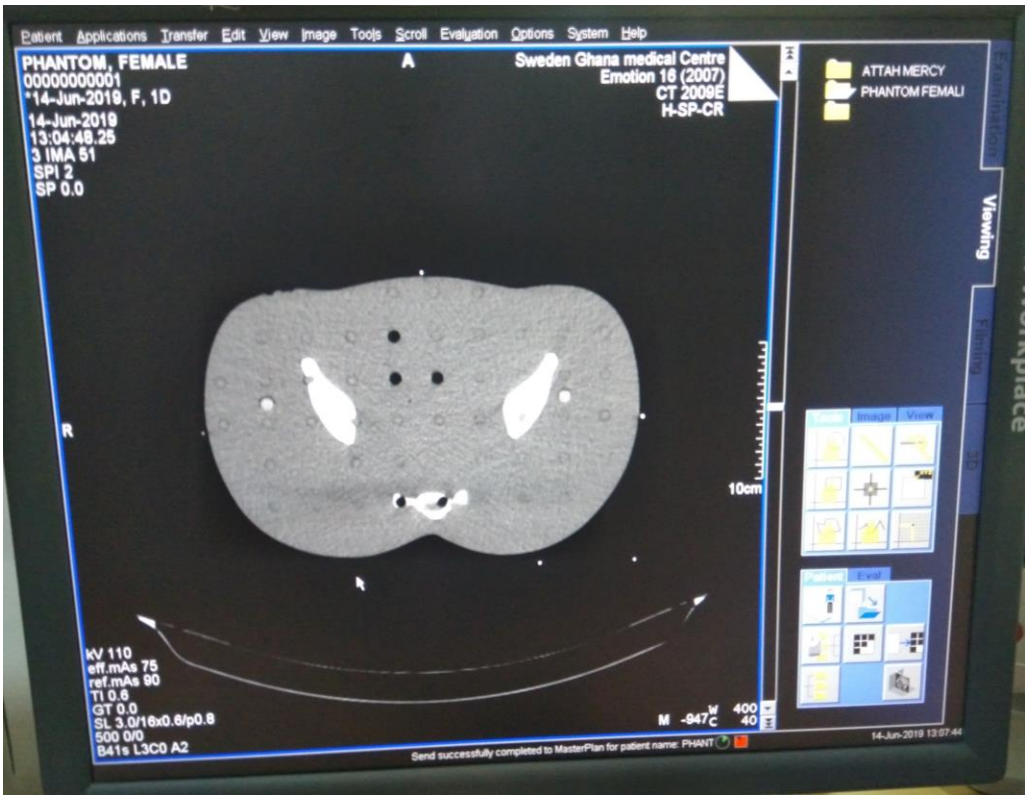


Figure 27: CT image of the pelvic region of the anthropomorphic obtained in this study, for planning (Field Data, 2018).

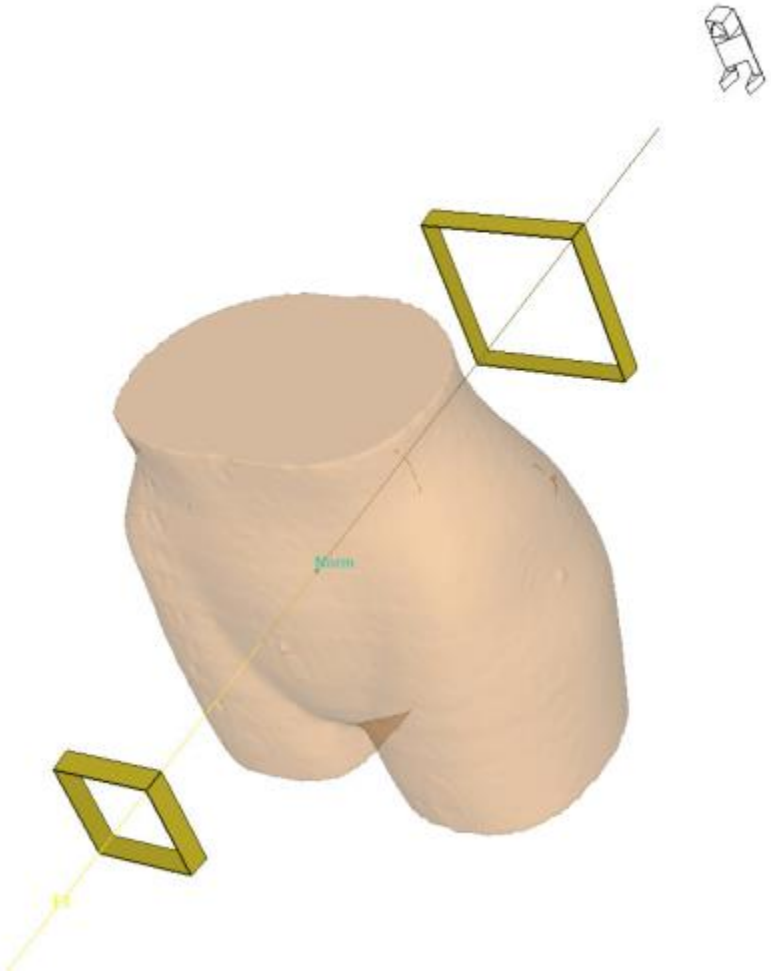

Figure 28: Anthropomorphic Pelvic Phantom Plan generated in this study, with beam arrangements (Field Data, 2018).

The SAD technique was used in all irradiations, and the dose prescription was made at the isocentre. Phantom irradiations were achieved using the Elekta synergy platform LINAC equipped with MLC to execute 3D conformal radiotherapy treatment. EPID images were taken for all irradiations made.

Additionally, dose measurements were made with TLDs simultaneously with EPID image acquisitions, for each irradiation. In this case, the LiF:Mg, Ti harshaw TLDs were used throughout the evaluation process.

For each EPID image acquired, absorbed doses to the isocentre were determined using the developed dose conversion model, and compared to corresponding TLD reading. The TLDS had been calibrated by the secondary standard dosimetry laboratory (SSDL) at the Radiation Protection Institute (RPI) of the Ghana Atomic Energy Commission (GAEC), making it traceable to the IAEA standards.

**Study Limitations**

The study conducted in this research has some limitations. First, the dosimetry model was only tested for images obtained by the EPID.

Secondly, the EPID panel was always positioned at the central position of the beam axis for all the measurements. The EPID was positioned at a fixed angle (perpendicularly) to the primary radiation beam, with the mid-plane of the phantom always coinciding with the isocentre of the beam. The effect of angular displacements of the EPID panel on the accuracy of the dosimetry model was not considered because SGMC routinely uses the EPID panel at a fixed position. Restriction in EPID panel position therefore limited the type of treatment fields that could be verified with this EPID transit dosimetry model.

Thirdly, the transmit dosimetry model assumed only radiation square field sizes. All EPID images were taken for only square isocentrically delivered fields with a fixed source to detector (SDD) distance. The validity of the EPID transit dosimetry model has therefore not been proven for non-radiation square fields.

Lastly, this study only involved absolute dosimetry measurement at the isocentre of the beam. The conversion model was therefore only tested for SAD

treatments techniques (treatment at isocentre) where tumour or targets are planned to be at the isocentre of the beam. This was due to the fact that SGMC treats routinely through SAD treatment technique.

**Chapter Summary**

In Chapter Three, dosimetric characteristics of the aSi EPI such as the dependence of the aSi EPID signal on varying doses, radiation treatment field sizes, patient thicknesses, and treatment couch, were investigated. The chapter provided in-depth description of procedures and protocols employed to achieve the results of each investigation. Additionally, Chapter Three provided a description of the method used to determine dose to the isocentre of a radiation beam in a phantom using the farmer-type IC. The chapter further described all modeling techniques employed in this work including the use of Minitab Statistical tool v18.1, vb.net and C++ programming language. Finally, the chapter provided a through description of methods used to evaluate the transit dosimetry model obtained in this work, and provided limitations for the study.

# CHAPTER FOUR

# RESULTS, ANALYSIS AND DISCUSSION

## Introduction

In this chapter, the relationship between EPID pixel values and various parameters are exhibited in tables and graphical portrayals. It additionally gives the model equations obtained in all stages of investigations, as well as the GUI application of the dose conversion model. The chapter provides graphical representations of the relationship between the various experimental data acquired from various parameters. The chapter ends with depictions and discussion of the outcomes of this study based on the objectives and scope of this work.

## Results of Performance Assessment of SGMC LINAC Facility

In Table 2, results of various QC tests performed on the Elekta Synergy Platform LINAC facility at the SGMC are provided. The tolerance level of each QC test is provided with reference to AAPM task group 142 (TG 142) (Klein et al., 2009). According to the AAPM TG 142 protocol, for any test, if the discrepancy between the measured value and the expected value is greater than the tolerance value, then an action is required to resolve the problem. It should be noted that, if mechanical or geometric parameters are out of tolerance, this would affect all measurements in this study. In this study, all measurements were found to be within the tolerance level recommended by AAPM TG 142 (Klein et al., 2009).

**Table 2: QC tests for the Elekta Synergy Platform LINAC facility at the SGMC.**

| Test | Performance | |
|---|---|---|
| | Tolerance | Test Result |
| Door interlock | Functional | Functional |
| Emergency off switches | Functional | Functional |
| Motion interlock | Functional | Functional |
| Couch brakes | Functional | Functional |
| Beam status indicators | Functional | Functional |
| Beam interrupt/counters | Functional | Functional |
| Lasers/crosswires | 2 mm | 1 mm |
| Optical distance indicator | 2 mm | 1 mm |
| Optical back pointer | 2 mm | 1 mm |
| Field size indicator | 2 mm | 2 mm |
| X-ray output constancy | 3% | 1.5% |
| Wedge transmission factor constancy | 2% | 1% |
| Gantry angle readouts | $1^0$ | $0.5^0$ |
| Collimator angle readouts | $1^0$ | $1^0$ |
| Collimator rotation isocentre | 2 mm | 1 mm |
| Couch position readouts | 1 mm | 1 mm |
| Couch rotation isocentre | 2 mm | 1 mm |
| Couch angle | $1^0$ | $0.5^0$ |
| Crosswire centering | 2 mm | 1 mm |
| Light/radiation coincidence | 2 mm | 1 mm |

In developing the dose conversion model, several steps was be taken into consideration to effectively and efficiently reconstruct doses from EPID images. Moreover, measurement of doses at the isocentre with the EPID requires knowledge of appropriate correction factors**.** Figure 29 shows an image acquired using a 6 MV beam open field size of 10 x 10 $cm^2$.

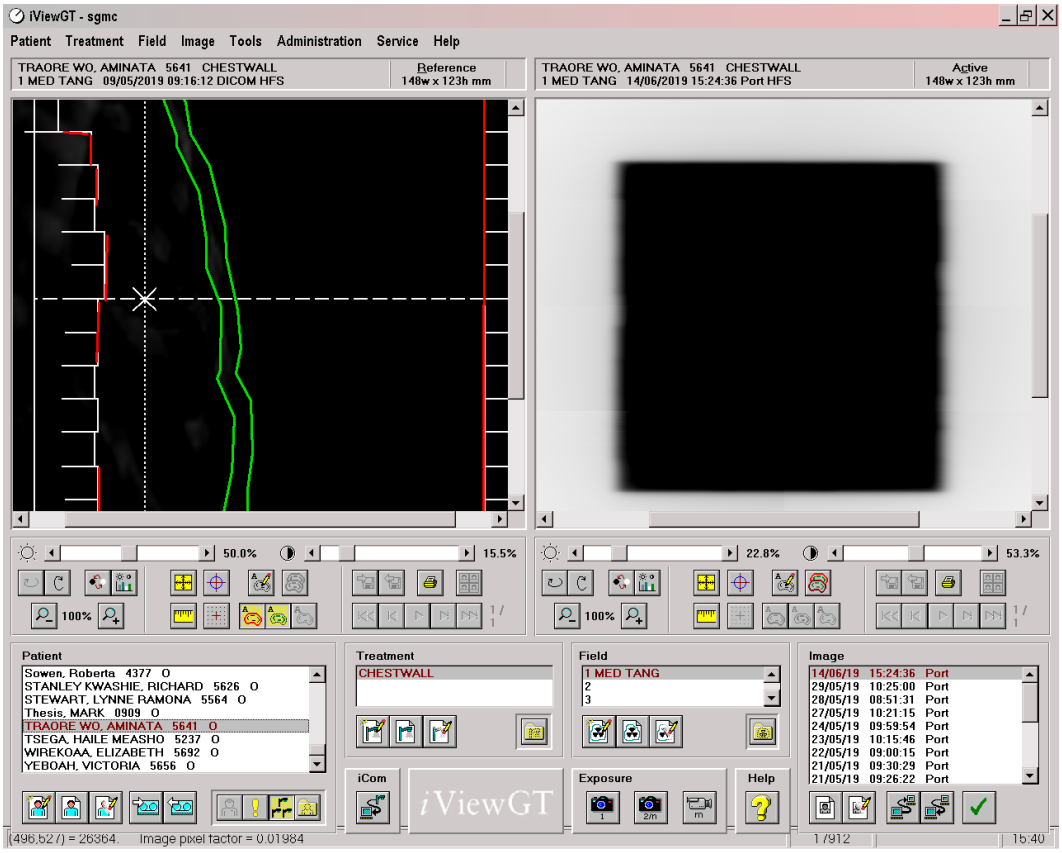


Figure 29: EPID iView System with displayed image (Field Data, 2016).

**Dose Linearity response with EPID signal ($S_{EPID}$)**

Table 3 shows the results of ion IC measurements and EPID signal readings obtained for dose response to EPID. Each IC measurement had been repeated twice, and the results averaged and corrected for temperature and pressure. In this table, EPID signal readings (pixel values) and the corrected averaged IC values (in Gy)

are provided for their corresponding delivered doses. All values are also normalized to the readings of the dose value of 1 Gy.

**Table 3: EPID signal and IC analysis for varying radiation doses**

| Delivered Dose (Gy) | Raw EPID signal (Grey Scale Pixel Value) | PSF | Corrected EPID signal $S_{EPID}$ | Normalized EPID signal ($S_{EPID\_normalized}$) | Averaged IC Reading (nC) | Corrected IC Reading (Gy) | Normalized IC values |
|---|---|---|---|---|---|---|---|
| 1.0 | 26218.542 | 0.025 | 1051648.257 | 1.000 | 18.06 | 1.00 | 1.000 |
| 1.1 | 26236.871 | 0.021 | 1269321.287 | 1.207 | 20.45 | 1.14 | 1.132 |
| 1.2 | 26294.245 | 0.020 | 1326534.125 | 1.261 | 22.04 | 1.23 | 1.221 |
| 1.3 | 26232.666 | 0.018 | 1426463.622 | 1.356 | 22.95 | 1.28 | 1.271 |
| 1.4 | 26240.758 | 0.017 | 1585544.290 | 1.508 | 25.51 | 1.42 | 1.413 |
| 1.5 | 26265.524 | 0.016 | 1612156.248 | 1.533 | 27.09 | 1.51 | 1.500 |
| 1.6 | 26225.040 | 0.015 | 1742527.575 | 1.657 | 28.05 | 1.56 | 1.553 |
| 1.7 | 26229.662 | 0.014 | 1903458.781 | 1.810 | 30.61 | 1.70 | 1.695 |
| 1.8 | 26240.053 | 0.013 | 2066145.906 | 1.965 | 33.12 | 1.84 | 1.834 |
| 1.9 | 26243.125 | 0.013 | 2095423.246 | 1.992 | 35.21 | 1.96 | 1.950 |
| 2.0 | 26238.998 | 0.012 | 2233106.213 | 2.123 | 35.78 | 1.99 | 1.982 |
| 2.1 | 26235.384 | 0.011 | 2393739.416 | 2.276 | 38.35 | 2.13 | 2.124 |
| 2.2 | 26264.453 | 0.011 | 2406240.125 | 2.288 | 39.74 | 2.21 | 2.201 |
| 2.3 | 26283.124 | 0.010 | 2536321.524 | 2.412 | 41.55 | 2.31 | 2.301 |
| 2.4 | 26292.451 | 0.010 | 2626423.124 | 2.497 | 43.35 | 2.41 | 2.401 |
| 2.5 | 26245.351 | 0.010 | 2726432.214 | 2.593 | 45.16 | 2.51 | 2.501 |
| 2.6 | 26261.215 | 0.009 | 2812325.241 | 2.674 | 46.97 | 2.61 | 2.601 |
| 2.7 | 26266.214 | 0.009 | 2945212.718 | 2.801 | 48.77 | 2.71 | 2.701 |
| 2.8 | 26279.894 | 0.009 | 3084324.214 | 2.933 | 50.58 | 2.81 | 2.801 |
| 2.9 | 26265.234 | 0.008 | 3135466.215 | 2.981 | 52.39 | 2.92 | 2.901 |
| 3.0 | 26281.569 | 0.008 | 3245231.234 | 3.086 | 54.26 | 3.02 | 3.005 |

In Figure 30, a graphical representation of EPID signal dependence on dose, indicated by a red fitted line is shown. Measurement of Elekta aSi EPID for varying range of doses from 0.5 to 3.0 Gy resulted in a strong positive correlation (correlation coefficient, r = 0.998) with EPID signal values (grey scale pixel values). For every change in the mean pixel value of the EPID signal, the fitted line rises or falls by 0.000001 Gy.

The increase in EPID signal response as a result of increment in delivered radiation dose, can be attributed to variations in attenuation of primary photon beams through the phantom. The higher the delivered radiation dose to the phantom (higher MU), more radiation is likely to reach the EPID sensitivity area due to lesser attenuation of primary photon beams of higher energies, and also as result of increase in radiation scatter reaching the EPID sensitivity area. This EPID signal – Dose response linearity agrees with those that were obtained by Wendling and his colleagues (Wendling et al., 2006) and Dina and his colleagues (Dina et al., 2015). In their work, Wendling et al. attributed these variations in EPID response to varying dose to contribution of scatter within the EPID, the contribution of scatter within the phantom, the contribution of scatter resulting from the phantom to the EPID and the attenuation of the primary photon beams through the phantom. Therefore, the mean greyscale EPID pixel value was highly dependent on radiation dose delivered.

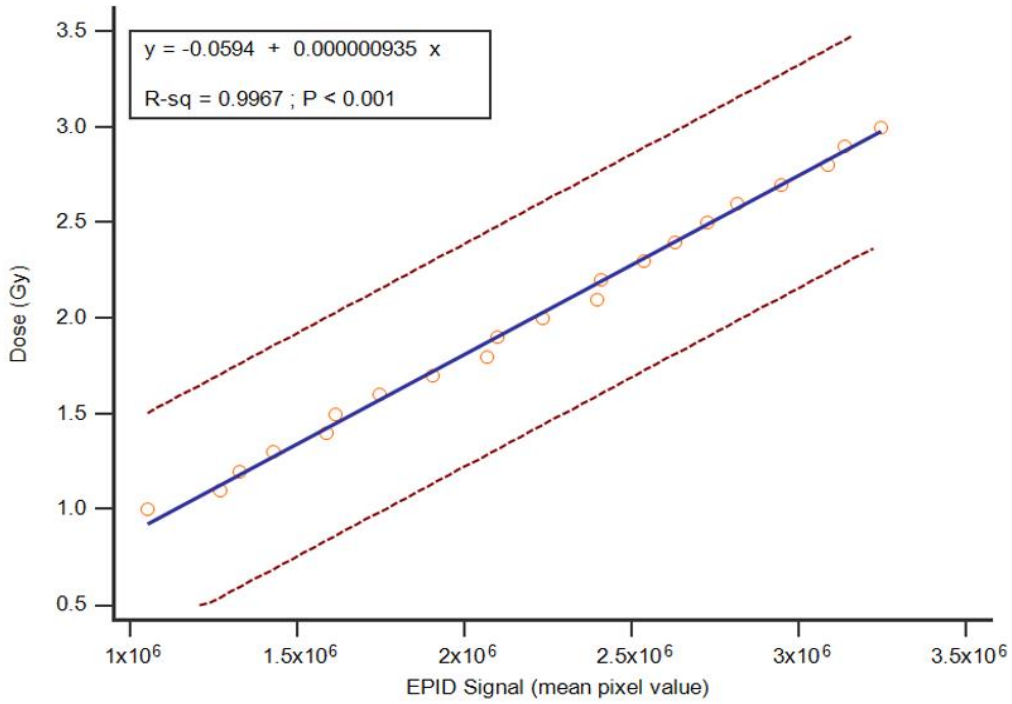


Figure 30: EPID signal response to varying delivered doses (Field Data, 2017).

In Figure 30**,** the higher linear value of coefficient of determination R-Sq (99.6 %) showed a very strong correlation between the delivered dose (Gy) and EPID signal, indicating that 99.6% of the variance in dose was accounted by EPID signal grey scale pixel values. The dataplots were all within 95% confidence interval, and hence 99% confident that the true mean was contained in the interval, thereby indicating higher precision. Moreover, the fitted line truly described the trend in the data, and EPID could be considered appropriate for measuring patient absorbed doses for radiotherapy daily QAs.

Additionally, the hypothetical output for the regression in Figure 27 is shown in Table 4. It was seen that the p-value (< 0.005) was much less than the significance level of 0.05. The null hypothesis of normality was rejected, with the conclusion that that there is a statistically significant difference among the mean of

the population. The test statistics was therefore significant at the 5% level. This was further explained by the residual plots provided for absorbed dose (Figure 31).

**Table 4: Hypothetical output for the regression from Dose-EPID signal plots**

| Term | Coef | SE Coef | T-Value | P-Value | VIF |
|---|---|---|---|---|---|
| Constant | -0.040500 | 0.029000 | -1.40 | 0.178 | - |
| EPID signal (mean pixel value) | 0.000001 | 0.000000 | 73.39 | 0.000 | 1.00 |

Source: Field Data, 2017

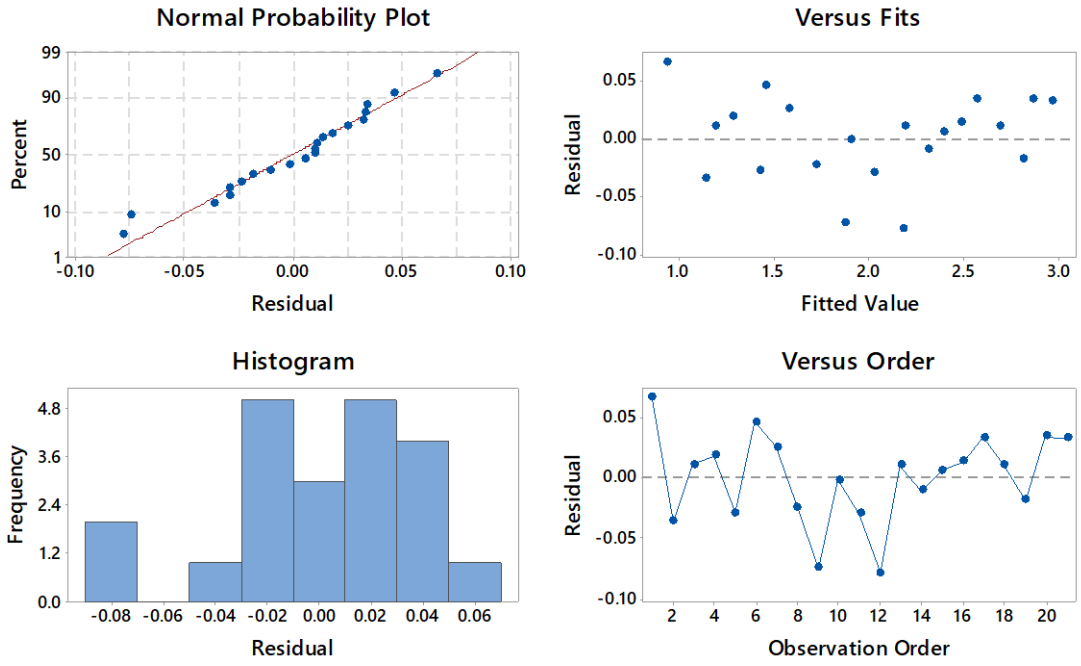


Figure 31: Various residual plots for delivered radiation doses (Field Data, 2017).

In Figure 31, the residual plots of absorbed dose are presented. The points on the normal probability plot form a nearly linear pattern, which indicates that the normal distribution was a good model for this data set. Additionally, the scatter plot

of residuals versus fitted values demonstrated a random pattern. The residuals fall randomly around the fitted values, indicating a linear relationship between EPID signals and absorbed dose. Likewise, the residual versus order plot suggests that there was a positive serial correlation among the error terms, and that a strong positive correlation was observed.

Moreover, the histogram residual plot shows the frequency of residual values, with two peaks at -0.02 and 0.02 respectively, and indicating non-symmetric properties, and hence being bimodal in nature. The histogram plots was centred at 0.00, and ranged from -0.08 to 0.06, with a gap at -0.6 without any outliers, entailing that the model meets all the assumptions of linear regression.

$$D(Gy) = -0.0594 + \left[\left(9.35\times10^{-7}\right)\times S_{EPID}\right] \quad (9)$$

In equation 9, the regression equation resulting from the plot of dose as a function of EPID signal was provided. The equation shows that the coefficient for EPID signal in pixel values was $9.35\times10^{-7}$ Gy. This coefficient indicates that for every additional EPID signal (pixel value), the dose was expected to increase by an average of $9.35\times10^{-7}$ Gy.

**Varying Doses: EPID versus IC**

Comparisons between EPID and IC scatter plots at delivered doses of 1 to 3 Gy are presented in Figure 32.

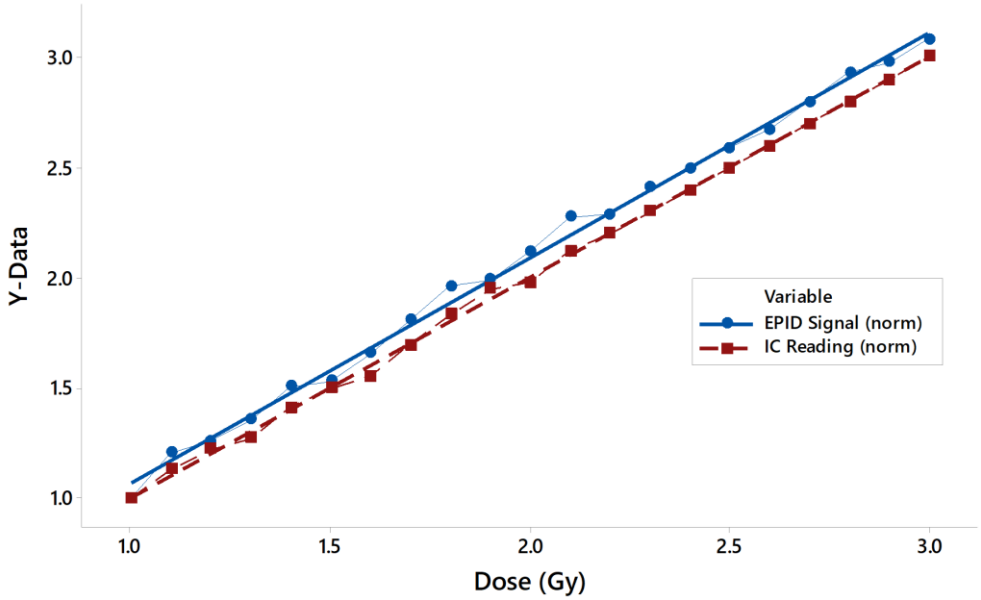


Figure 32: Comparisons between EPID and IC scatter plots at same delivered doses (Field Data, 2017).

Comparatively, results from the EPID measurements and the IC measurements showed identical response to varying doses (Figure 32). The gradient of the EPID measurements ($\nabla = 0.998$) did not vary greatly from that for the IC measurements ($\nabla = 1.022$). The IC used in this comparison was used for absolute measurements of the LINAC output. This means that the EPID was comparable and traceable to the IC which was calibrated and known to have a high accuracy (90%) in detecting deviations in LINAC output.

The test therefore proves that the EPID data points have a strong correlation (correlation coefficient, $r = 0.998$) with dose within this range of doses, and that the gradient was adequate to resolve discrepancies in LINAC output.

**Absolute Dose Correction Factor (DF) for different doses**

According to Wendling (Wendling et al., 2006), the EPID pixel value obtained was affected by several factors: The scattered radiation from EPID; the scatter within the phantom; the scatter from the phantom to the EPID, and the attenuation of the beam by the phantom. Hence it was of high importance to correct for the effect by implementing dose correction factor (DF) for each delivered dose. In this study, the DF for each delivered dose was obtained by dividing the normalized IC value for each delivered dose, by their corresponding normalized EPID signal reading. This was done to correct the EPID signal readings with a device (IC) which was traceable to IAEA protocol TRS 398 (IAEA, 2000). Table 5 shows the delivered range of doses (1 to 3 Gy) and their corresponding DF for the EPID. The average value of DF obtained was 0.957.

**Table 5: Correction factors determined for different dose**

| Dose (Gy) | Dose Correction Factor (DF) |
|---|---|
| 1.0 | 1.000 |
| 1.1 | 0.938 |
| 1.2 | 0.968 |
| 1.3 | 0.937 |
| 1.4 | 0.937 |
| 1.5 | 0.979 |
| 1.6 | 0.938 |
| 1.7 | 0.937 |
| 1.8 | 0.934 |
| 1.9 | 0.979 |
| 2.0 | 0.933 |
| 2.1 | 0.933 |
| 2.2 | 0.962 |
| 2.3 | 0.954 |
| 2.4 | 0.961 |
| 2.5 | 0.965 |
| 2.6 | 0.973 |
| 2.7 | 0.964 |
| 2.8 | 0.955 |
| 2.9 | 0.973 |
| 3.0 | 0.974 |
| Average value of DF | 0.957 |

Source: Field Data, 2016

**Field Size - EPID Response**

Table 6 shows the results of IC measurements and EPID signal readings obtained for varying radiation field sizes (5×5 to 25×25 $cm^2$) with the same delivered dose of 100 MU. Each IC measurement was repeated twice, and the

results averaged and corrected for temperature and pressure. In Table 6, EPID signal readings (pixel values) and the corrected averaged IC values (in Gy) were provided for their corresponding radiation field sizes. Both IC and EPID readings were normalized to the readings of the $10 \times 10$ $cm^2$ radiation field size.

**Table 6: EPID signal and IC analysis for varying radiation field sizes**

| Field Size ($cm^2$) | Raw EPID signal (Grey Scale Pixel Value) | PSF | Corrected EPID signal $S_{EPID}$ | Normalized EPID signal $S_{EPID\_normalized}$ | IC Mean (nC) | Corrected IC Reading (Gy) | Normalized IC Values |
|---|---|---|---|---|---|---|---|
| 5 × 5 | 26386.762 | 0.399 | 66121.427 | 0.915 | 1.087 | 0.060 | 0.916 |
| 10 × 10 | 26410.941 | 0.366 | 72232.089 | 1.000 | 1.187 | 0.066 | 1.000 |
| 15 × 15 | 26420.030 | 0.331 | 79862.251 | 1.106 | 1.238 | 0.069 | 1.043 |
| 20 × 20 | 26366.913 | 0.305 | 86417.728 | 1.196 | 1.273 | 0.071 | 1.072 |
| 25 × 25 | 26366.806 | 0.280 | 94021.152 | 1.302 | 1.293 | 0.072 | 1.089 |

Source: Field Data, 2016

Although same delivered doses were given for all the field sizes at the isocentre at 10 cm in the 20 cm thick PMMA phantom at SSD = 90 cm, there were differences in the PSF values, which is because of the diverse contributions from scatter due to varying radiation field sizes.

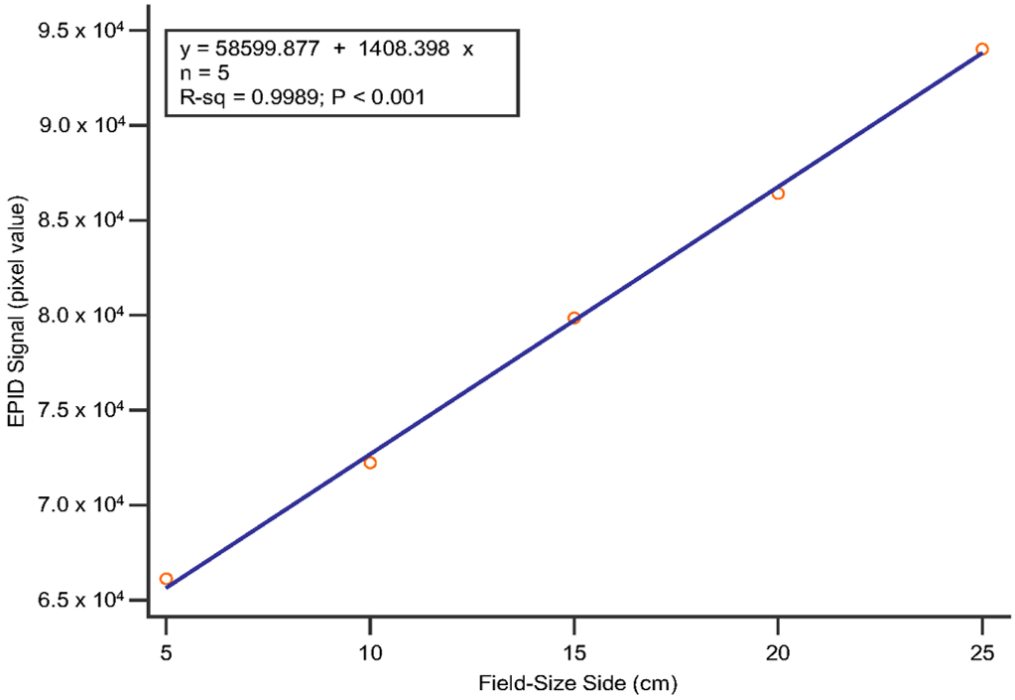


Figure 33: EPID signal response to varying radiation field sizes (Field Data, 2016).

In Figure 33, a graphical representation of radiation field size dependence on EPID signal, indicated by a red fitted line is shown. The fit showed a linear regression of EPID signal (grey scale pixel values) in response to varying radiation field sizes. The higher value of coefficient of determination R-Sq (99.9 %) showed a very strong correlation between the radiation field size and EPID signal (grey scale pixel values), indicating that 99.9% of the variance in EPID signal was contributed by changes in radiation field sizes. This significant contribution from field size was due to the enormous contribution of scatter.

As radiation field size increases, the number of electrons per gram (electron density) increases. Since the image formation is a statistical process that involves the detection of discrete X-ray quanta (Herman et al., 2001), the increase in X-ray scattering results in an increase in the number of X-ray photons exiting the patient. Consequently a higher number of X-ray quanta reaches the image receptor of the EPID. This accounts for the higher grey scale or pixel values which form the image, and hence the higher EPID signal with increasing field size.

The output results of this study is in perfect agreement with that obtained by Ibrahim et al. (Ibrahim et al., 2018). In their publication, Ibrahim and colleagues tested the signal response of EPIDs for varying field sizes of 2 × 2 to 25 × 25 $cm^2$. Results from EPID signal measurements was found to be directly proportional to changes in varying radiation field sizes. Similarly, the proportionality of EPID signal response with increasing radiation field sizes agrees with that of Aleksandra et al. (Grządziel et al., 2007) and Bozena et al. (Woźniak et al., 2005). Aleksandra et al. considered testing radiation field range of 3 × 3 to 30 × 30 $cm^2$, whereas Bozena et al. evaluated EPID signal response for field size ranges from 5 × 5 to 25 × 25 $cm^2$.

Figure 33 further indicates that all dataplots were within 95% confidence interval, and hence the true mean was contained in the interval, thereby indicating higher precision. Hence the fitted line truly describes the trend in the data, and EPID could be considered appropriate for detection of dosimetric contribution of varying radiation field sizes.

**Table 7: Hypothetical output for the regression resulting from EPID signal – Field Size plot**

| Term | Coef | SE Coef | T-Value | P-Value | VIF |
|---|---|---|---|---|---|
| Constant | 58735.0 | 469.0 | 125.13 | 0.000 | - |
| Field-Size Side (cm) | 1399.7 | 28.3 | 49.45 | 0.000 | 1.00 |

Source: Field Data, 2016

In Table 7, the hypothetical output for the regression in Figure 33 is shown. The p-value was obtained to be 0.000, and was much less than the significance level of 0.05. The null hypothesis of normality was hence rejected, and a conclusion was made that there was a significant difference among the mean of the population. The test statistics is therefore significant at the 5% level. This was further explained by the residual plots provided for EPID signal resulting from varying radiation field size (Figure 34).

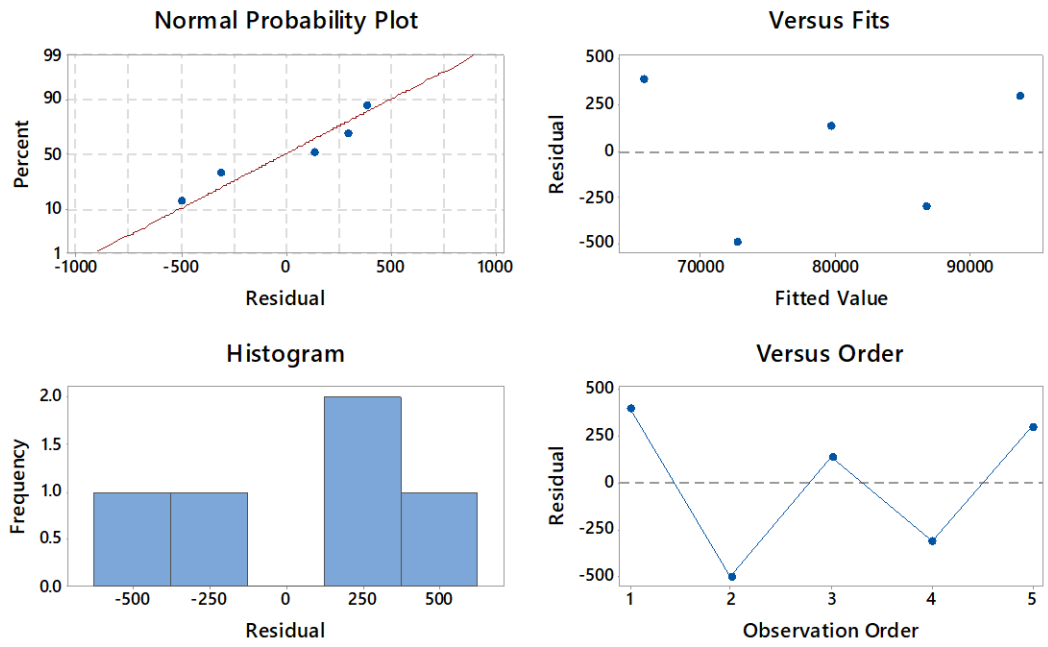


Figure 34: Various residual plots of EPID grey scale pixel values at different radiation field sizes (Field Data, 2016).

In Figure 34, the residual plots of EPID signal resulting from varying radiation field sizes is shown. The points on the normal probability plot form a linear pattern, indicating that the normal distribution was a good model for this data set. Additionally, the scatter plot of residuals versus fitted values demonstrates a positive random pattern. The residuals were distributed randomly around the fitted values, indicating a linear relationship between EPID signals and radiation field size. Similarly, the residual versus order plot suggests that there was a positive serial correlation among the error terms, and that a strong positive correlation was observed.

In addition, the histogram residual plot displayed a symmetric bell-shaped pattern centred at 0 with no outliers, had one peak at 250, and hence being unimodal in nature. The histogram plota further provided a range from -500 to 500 with a gap

at 0, and without any outliers. Hence the resulting model met all the assumptions of linear regression.

**Dose Correction for Different Field Size**

Table 8 shows various radiation field sizes used in this study, and their corresponding correction factors. Although all the field sizes were irradiated to the same dose (100 MU) at the isocentre at 10 cm depth in a 20 cm thick PMMA slab phantom and at SSD = 90 cm, there was a difference in the PSF values, which was due to the different contributions of scatter by changing the field size.

**Table 8: Correction factors determined for different radiation field sizes**

| Field size ($cm^2$) | $CF_{fs}$ |
|---|---|
| 5 × 5 | 1.0003 |
| 10 × 10 | 1.0000 |
| 15 × 15 | 0.9433 |
| 20 × 20 | 0.8964 |
| 25 × 25 | 0.8368 |

Source: Field Data, 2016

In this study, the correction factor for each radiation field size was obtained by dividing the normalized IC value for each field size, by their corresponding normalized EPID signal reading (as provided in Table 6). Again, this was done to correct the EPID signal readings with a device (IC) which was traceable to IAEA protocol TRS 398 (IAEA, 2000).

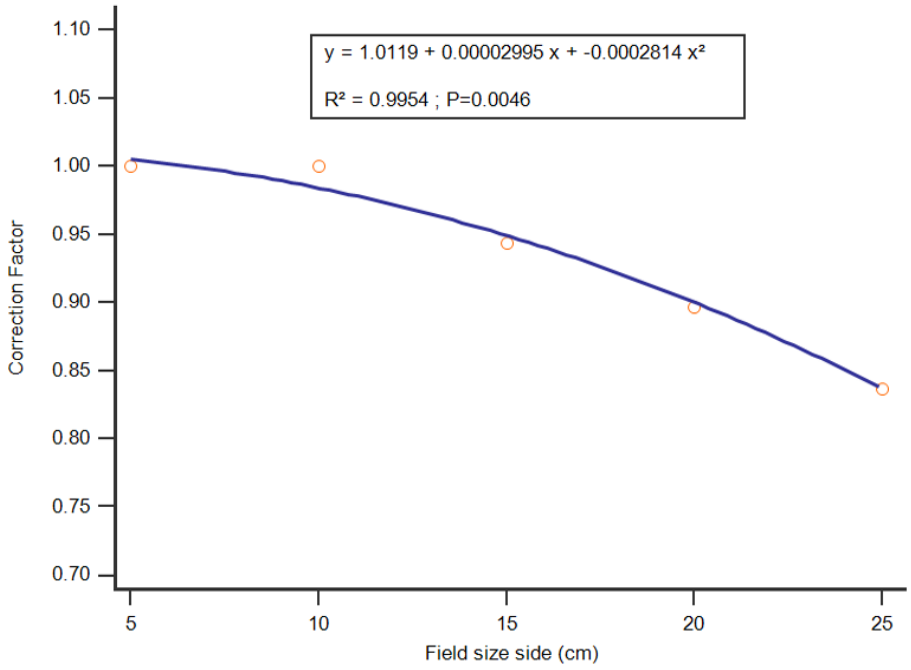


Figure 35: Correction factors for different radiation field sizes (Field Data, 2016).

In Figure 35, a graphical representation of dose correction for field size ($CF_{fs}$) as a function of radiation field size side is given, indicated by a red fitted line. The plot showed a curvilinear relationship between radiation field sizes and their corresponding correction factors.

In Equation 10 the regression equation resulting from the plot is presented. This modeled equation provided corrections for scatter as a result of varying field sizes. $FS_x$ denotes radiation field size-side, and $CF_{fs}$ represents field size correction factor.

$$CF_{fs} = 1.0119 + \left[\left(2.995\times10^{-5}\right)\times FS_x\right] - \left[\left(2.814\times10^{4}\right)\times FS_x^2\right] \qquad (10)$$

**Dependence of EPID signal on Phantom/Absorbent thickness**

In Table 9, results of IC measurements and EPID signal readings obtained for different absorbent/phantom thicknesses are shown. Each IC measurement was

repeated twice, and the results averaged and corrected for temperature and pressure. From Table 9, EPID signal readings (pixel values) and the corrected averaged IC values (in Gy) are provided for each phantom thickness size. All values were also normalized to the readings of 20 cm phantom thickness.

Figure 36 shows the dependence of EPID signal on phantom thickness. Thickness of the phantom located between the source and EPID panel influences the signal level of EPID. Signal level decreases with increasing absorbent thickness. The plot shows an exponential regression of EPID signal in response to varying phantom thicknesses (cm).

As the absorber thickness increases, the number of electrons per gram (electron density) increases. As scattering depends highly on electron density, the probability of the incident photon radiation undergoing scattering increases, and hence accounting for a greater number of X-ray scatter radiation exiting the patient. The image formation by EPID is a statistical process that involves the detection of discrete X-ray quanta (Herman et al., 2001). Hence the increase in scattered radiation as a result of increment in absorbent thickness increases the total fluence reaching the EPID image receptor. This gives rise to an increased grey scale or EPID pixel values which form the image (EPID signal). The pixel value is proportional to the amount of free charges forming in the detector as a result of interactions of the X-ray beam with EPID.

The high 99.78% R-Sq value (Figure 36) indicates that the correlation coefficient between the EPID signal and phantom thickness (cm) was 99.78%, demonstrating a very strong relationship between EPID signal and phantom or

absorbent thickness (cm). Similarly, the adjusted R-sq (R-sq (adj)) shows the coefficient of determination, which measured the goodness of fit. The high R-sq (adj) value of 99.8% further suggests that, the total variation in EPID signal was explained by 99.8% of phantom thickness size, hence emphasizing that varying phantom thicknesses had a very strong impact on EPID signal.

**Table 9: EPID signal and IC analysis for varying phantom thicknesses**

| Phantom Thickness (cm) | Raw EPID signal (Grey Scale Pixel Value) | PSF | Corrected EPID signal ($S_{EPID}$) | Normalized EPID signal ($S_{EPID\_normalized}$) | IC Mean (nC) | Corrected IC Reading (Gy) | Normalized IC Values |
|---|---|---|---|---|---|---|---|
| 4 | 25679.324 | 0.02046 | 1255098.925 | 1.802 | 1.753 | 0.098 | 1.057 |
| 6 | 25682.512 | 0.02222 | 1155828.623 | 1.660 | 1.889 | 0.105 | 1.140 |
| 8 | 25644.762 | 0.02405 | 1066310.270 | 1.531 | 1.898 | 0.106 | 1.145 |
| 10 | 25673.762 | 0.02605 | 985557.083 | 1.415 | 1.863 | 0.104 | 1.124 |
| 12 | 25634.814 | 0.02808 | 912920.727 | 1.311 | 1.823 | 0.102 | 1.099 |
| 14 | 25651.421 | 0.03027 | 847420.581 | 1.217 | 1.784 | 0.099 | 1.076 |
| 16 | 25642.974 | 0.03252 | 788529.336 | 1.132 | 1.741 | 0.097 | 1.050 |
| 18 | 25641.021 | 0.03487 | 735331.833 | 1.056 | 1.702 | 0.095 | 1.027 |
| 20 | 25638.613 | 0.03682 | 696323.004 | 1.000 | 1.658 | 0.092 | 1.000 |

Source: Field Data, 2017

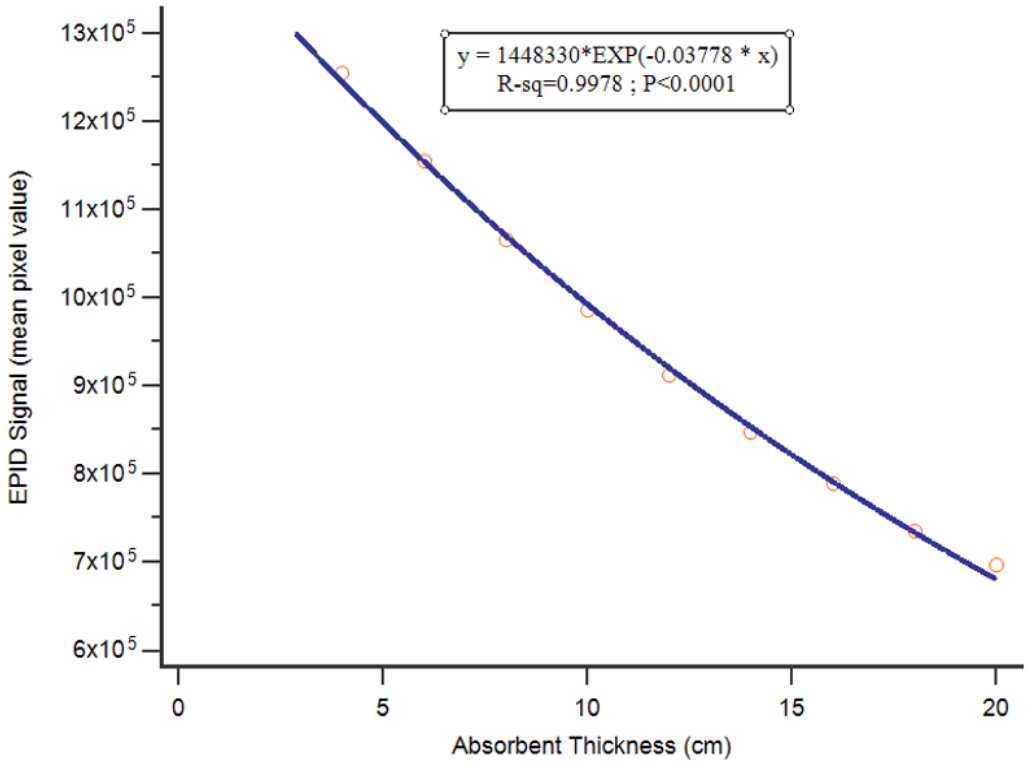


Figure 36: EPID signal response to varying absorbent phantom thicknesses (Field Data, 2017).

In Equation 11, an exponential function which expresses the dependence of EPID signal $S_{EPID}$ on absorbent thickness is provided, where the 0.0377791 value represents the linear attenuation coefficient of the PMMA phantom for the specific radiation beam energy. The radiation path length of the beam through the phantom is also denoted by (t).

$$S_{EPID} = 1.44833 \times 10^{6} e^{-0.03778t} \qquad (11)$$

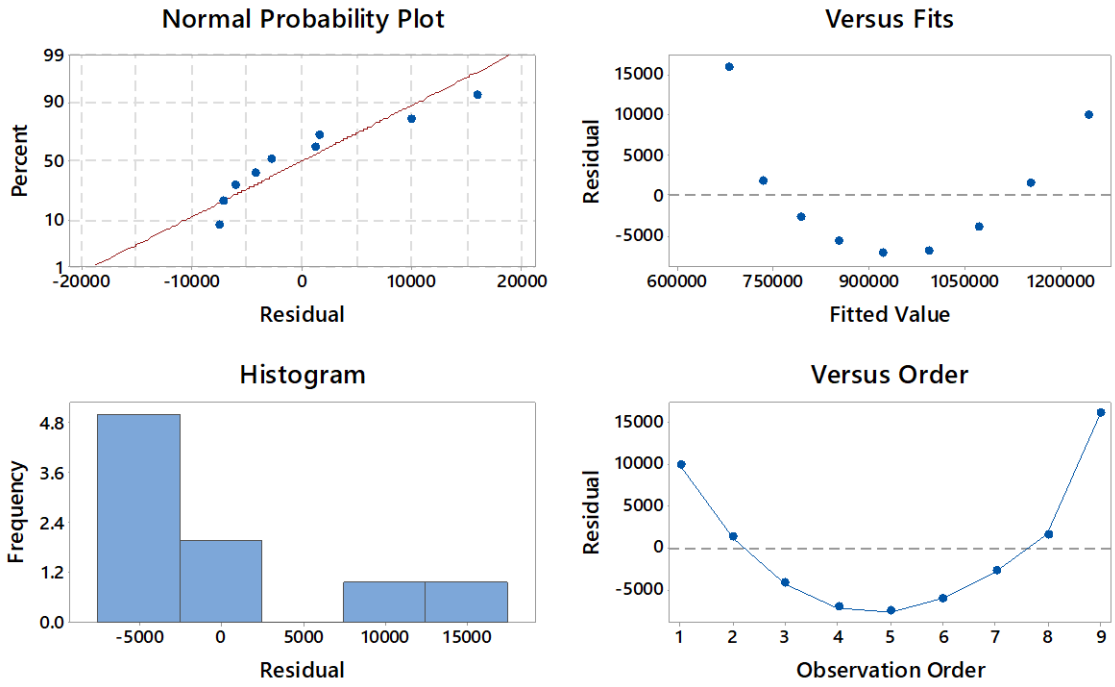


Figure 37: Various residual plots of EPID grey scale pixel values for different absorber phantom thicknesses (Field Data, 2017).

Figure 37 shows the residual plots of EPID signal resulting from varying phantom thicknesses. The model validation plot indicates that the model satisfies the assumption of homoscedasticity as there was no pattern within the residuals and fitted values plotted. Additionally, the normal Q-Q plot (normal probability plot and Histogram) satisfied the assumption of normality, and thus implied that the model meets all the assumptions of linear regression.

Additionally the coefficient of regression resulting from the plot, indicated a low p-value ($p << 0.001$), and thus further suggested that changes in the mean pixel values of EPID signal were associated with changes in phantom thicknesses.

**Dose correction for different phantom thicknesses**

Table 11 shows various phantom thicknesses used in this study, and their corresponding correction factors. Although all the field sizes were exposed to the same dose (100 MU) at the isocentre at a depth of 10 cm in a 20 cm thick PMMA solid water phantom. Variations in the PSF values were observed, which are as a result of the different contributions of scatter due to the varying radiation field sizes.

**Table 10: Correction Factors determined for different absorbent phantom thicknesses.**

| Phantom Thickness | $CF_t$ |
|---|---|
| 4 | 0.587 |
| 6 | 0.687 |
| 8 | 0.748 |
| 10 | 0.794 |
| 12 | 0.839 |
| 14 | 0.884 |
| 16 | 0.928 |
| 18 | 0.972 |
| 20 | 1.000 |

Source: Field Data, 2017

The correction factor for each radiation phantom thickness in Table 10 was obtained by dividing the normalized IC value for each thickness size, by their corresponding normalized EPID signal reading (Table 9)

This was done to correct the EPID signal readings with an IC which was traceable to IAEA protocol TRS 398 (IAEA, 2000).

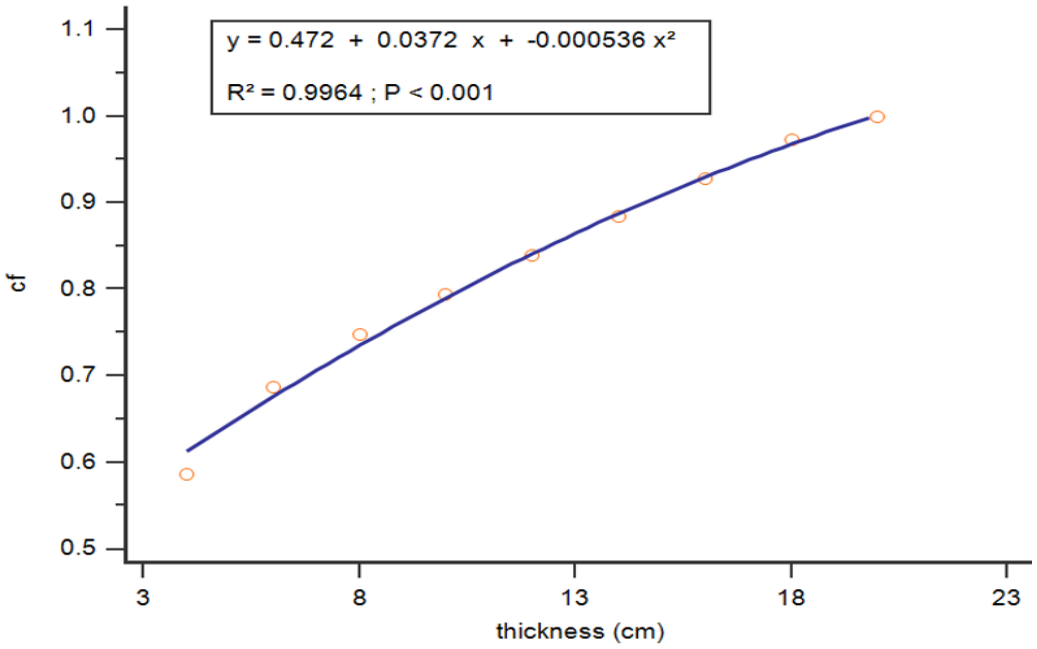


Figure 38: Correction factors for different absorbent phantom thicknesses (Field Data, 2017).

In Figure 38, a graphical representation of dose correction for phantom thickness as a function of radiation phantom or absorbent thickness was given, indicated by a red fitted line. Equation 12 shows the regression equation resulting from the plot. This modeled equation provides corrections for contributive effects of absorbent thickness on EPID signal. t denotes absorbent thickness, and $CF_t$ denotes phantom (absorbent) thickness correction factor.

$$CF_{thickness} = 0.472 + (0.0372 \times t) - \left[ (5.36 \times 10^{-4}) \times t^2 \right] \quad (12)$$

**Therapeutic Couch Correction**

Table 11 shows the results of EPID pixel measurements obtained under two conditions; with the therapeutic table placed in the beam, and with no therapeutic

table in the beam. The test was done three times under same reference conditions as stated in chapter 3.

The correction factor for each measurement was determined by dividing the EPID pixel value obtained without couch in the beam, by the corresponding EPID pixel value obtained with couch in the beam (Equation 13). An overall correction factor of 1.029 was determined for the therapeutic couch by averaging all correction factors obtained for all three (3) tests.

$$CF_{couch} = \frac{S_{EPID\_without\_couch}}{S_{EPID\_with\_couch}} \qquad (13)$$

**Table 11: EPID signal analysis for therapeutic Couch effect**

| Test | With treatment Couch | | | Without treatment Couch | | | Correction Factor $(CF_{couch})$ |
|---|---|---|---|---|---|---|---|
| | EPID signal (Grey Scale Pixel Value) | PSF | Corrected EPID signal $S_{EPID\_with\_couch}$ | EPID signal (Grey Scale Pixel Value) | PSF | Corrected EPID signal $S_{EPID\_without\_couch}$ | $\frac{S_{EPID\_without\_couch}}{S_{EPID\_with\_couch}}$ |
| Test #1 | 25905.866 | 0.31028 | 83491.898 | 25604.519 | 0.315 | 81211.999 | 1.028 |
| Test #2 | 25619.046 | 0.30823 | 83116.653 | 25634.235 | 0.318 | 80519.648 | 1.032 |
| Test #3 | 25883.871 | 0.30672 | 84389.250 | 25609.546 | 0.312 | 82166.151 | 1.0271 |
| | | | | | | | Average $CF_{couch}$=1.029 |

Source: Field Data, 2017

**Qualitative remarks on the reference measurements**

IC measurements are considered as the highest quality level in absolute dosimetry. In this study, IC measurements were taken as the reference measurements, due to the traceability of the IC to the IAEA (IAEA, 2000, 2005, 2009). In any case, they present a few vulnerabilities that could affect the comparison of IC measured doses with converted EPID signals. As discussed earlier, the dosimetric measurements from the farmer chamber was subjected to temperature and pressure and correction factors. Notwithstanding, the temperature in the treatment room was restricted, particularly when the machine was on for quite a while. The LINAC was discharging a specific measure of heat as the beam is turned on and a ventilation framework in the treatment room controls the temperature with constrained achievement. The active volume of the chamber characterizes the goals of the measurements. The measured doses at any point was an average of the active volume of the IC, and this affected the measurements.

**Converting Modelled Equations to GUI**

The modeling process involved two techniques; Minitab statistical application software and mathematical ellipsoid analysis technique. The modelling technique involved different equations using the Minitab statistical tool. The equations showed EPID signal dependence and their correction factors (Equations 10 to 13). These equations were then modelled into one equation (Equation 14), with other parameters included in the equation for onward modelling into a comprehensive GUI design using C++ and vb.net codes.

$$D = -0.0594 + \left[\left(9.35\times10^{-7}\right)\times S_{EPID}\right]\times 1.0119 + \left[\left(2.995\times10^{-5}\right)\times FS_x\right] - \left[\left(2.814\times10^{4}\right)\times FS_x^2\right]\times 0.472 + \left(0.0372\times t\right) - \left[\left(5.36\times10^{-4}\right)\times t^2\right]\times DF\times CF_{couch}\times SF \quad (14)$$

Equation 14 describes the relationship between the EPID signal and absorbed dose as a function of radiation field size and phantom thickness with appropriate correction factors applied.

The conversion model contains the DF, the pixel sensitivity correction factor (SF), radiation field size correction, the absorbent patient thickness correction, and the treatment couch correction ($CF_{couch}$).

The pixel sensitivity correction was a simple solution to correct the EPID pixel sensitivity. It was applied by dividing the EPID acquisition produced by 1 Gy photon energy by a corresponding IC reading produced by 1 Gy under reference conditions (10 ×10 $cm^2$ field size area, 100 cm SAD, and 10 cm depth). This sensitivity correction should be applied regularly.

The radiation field size correction was implemented to account for varying field size effect on dose distribution and EPID pixel values. The field size was related to the amount of primary radiation entering the patient and the subsequent dose distribution. A dose at any point resulted from both the primary and scattered radiation. Bigger field sizes lead to increased generation of scattered radiation, which led to increase dose at a specified point, and affected EPID pixel values. On the other hand, small field sizes may prompt loss of electronic equilibrium (Charles, 2014; Gonzalez-Lopez et al., 2015).

The patient thickness correction also provided a solution to correct for the effect of scatter resulting from patient thickness on EPID pixel values.

Additionally, the treatment couch correction factor was introduced to account for dose perturbation by the treatment couch. The presence of the therapeutic couch in the beam causes attenuation of beam to the EPID panel, affecting EPID pixel values.

**GUI Model**

The resulting GUI represented the relation between delivered and measured radiotherapy doses. The GUI reduced the equation to user friendly interface for clinical application. In Figure 39, the GUI of dosimetric model (named PokooDose) is shown, whereas the written C++ and vb.net codes are provided in Appendix A.

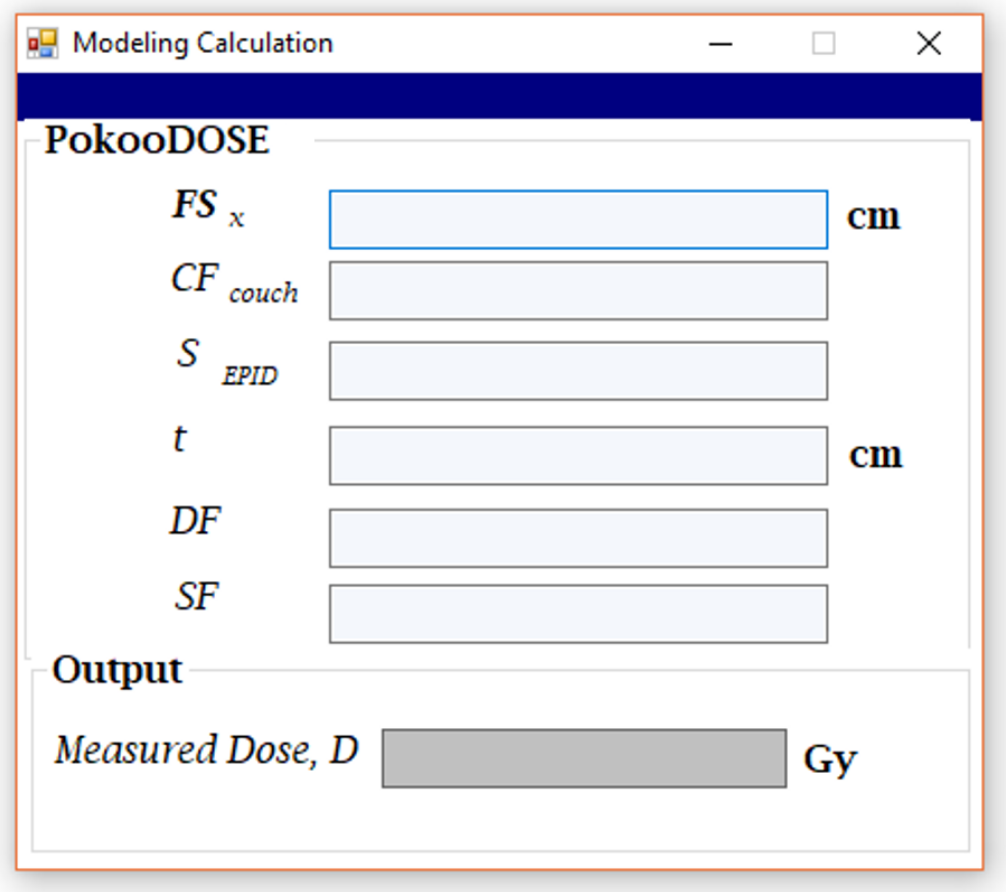


Figure 39: Design of GUI for real-time dose verification

**Clinical Evaluation of Dose Conversion Model**

The dose conversion model was evaluated with the anthropomorphic phantom. In all, a total of six (6) treatments field were used for the evaluation. The percentage deviation between the model values and the TLD measured values are summarized in Table 12. The discrepancies in model calculations was determined from equation 15.

$$Discrepancy\ (\%) = \frac{Model\ Value - TLD\ measurement}{TLD\ measurement} \times 100 \qquad (15)$$

**Table 12: Dose Conversion Model (PokooDose) evaluation with anthropomorphic phantom**

| Planned TPS (Gy) | TLD Measurements (Gy) | Model Value (Gy) | Discrepancies in Model Calculations % |
|---|---|---|---|
| 0.8 | 0.81 | 0.78 | -3.70 |
| 1.0 | 1.04 | 1.08 | 3.85 |
| 1.2 | 1.19 | 1.23 | 3.36 |
| 1.5 | 1.53 | 1.47 | -3.92 |
| 1.8 | 1.78 | 1.85 | 3.93 |
| 2.0 | 1.96 | 1.98 | 1.02 |

Source: Field Data, 2017

All doses from the dose conversion model were in agreement with TLD measurements within 5%. An accepted level of ±5% is recommended by the IAEA (IAEA, 2013). This observation led to the conclusion that EPID measurements could be used for absolute dose comparison, likewise the transit dosimetry model.

**Chapter Summary**

Chapter Four provided comprehensive discussions and analyses of data obtained from all investigations relating to dosimetric characteristics of the amorphous silicon EPID (aSi EPID). Various analysis were made for aSi EPID dependence on varying doses, radiation treatment field sizes, patient thicknesses, and treatment couch. In each investigation, good fits (higher R –sq values) were obtained for values measured using EPID and the IC. The chapter

further provided various correction factors determined in each investigation done on dosimetric characteristics of the aSi EPID. These correction factors were determined to address various dosimetric effects on EPID signal. Additionally in this chapter, all modelled equations derived in this study were presented, as well as the GUI application of the transit dosimetry model that was obtained in this study using C++ and vb.net codes. Finally, the chapter provided analysis of data obtained while evaluating the transit dosimetry model obtained in this study. The developed model proved to satisfy radiotherapy accuracy requirements, after it had been subjected to evaluations using an anthropomorphic phantom.

# CHAPTER FIVE

# SUMMARY, CONCLUSIONS AND RECOMMENDATIONS

## Introduction

This chapter presents an outline of findings relating to measured EPID pixel values, IC measurements and TLD measurements. This chapter summarizes the entire study, and reaches insightful conclusions on the development of mathematical and computer aided design models for transit dosimetry in clinical application. It also states various corrections for absolute dose measurements. It additionally states different rectifications for absolute dosimetry measurements. It ends with the conclusions and recommendations of the findings of the study.

## Summary

The wide topic of this thesis was aimed at improving QC in radiotherapy. Chapter One briefly illustrated the potential dangers in radiotherapy and the role of the QC in real-time radiotherapy treatments. QC assumes a significant role of verifying delivered doses during actual treatment delivery to patients. The role of QC was to ensure that the actually planned treatment has been precisely conveyed to the patient. Ideally, treatment verifications ought to be performed to check delivered dosages amid radiotherapy daily routine works. However, this may not be constantly achievable because of time consuming procedures required to execute these dose verifications. Thus, the challenge was to find a routinely clinically applicable, and an efficient way to carry out dose verifications. Among the

various sorts of measuring devices, EPID was favoured due to its efficiency and effectiveness. EPID was favoured because it was readily accessible by LINACs, and produces an immediate 2D digital image of higher resolution, which does not require cumbersome manual processing. EPID was initially intended for positional verification purposes, and a few techniques have been executed over the previous years to utilize the EPID as a tool to verify radiation doses. However all these techniques usually require commissioning and time consuming procedures to verify real-time radiotherapy dose, which made it difficult to use in the daily radiotherapy routine works. A technique which could be simple, adequate and accurate to be employed in clinical routine was therefore needed, and this study sought to address that.

Chapter Two provided a literature review on different strategies to overcome the dosimetric challenges encountered using EPIDs. The literature review comprised non transit and transit EPID dosimetry techniques, although the focal point of this study was on transit dosimetry, which could be utilized in real-time treatment verifications. The objective of this study was to develop an in-house transit dosimetry calculation model for verifying patient dose using aSi EPID, and which could be adequate and accurate to be employed in clinical routine.

In Chapter Three, materials and the techniques used to obtain the transit dose conversion model in this study were illustrated. It begun by writing the materials and methods that were used to study the dependence of EPID signal on varying doses, radiation treatment field sizes, patient thicknesses, and the treatment couch. Prior to undertaking all investigations, a QC test was done on

the SGMC LINAC facility which included mechanical and safety checks. This was to ensure and guarantee that quality requirements of the LINAC facility at the SGMC were met, and in compliance with TG 142 accepted codes of practice. The chapter also provided an in-depth discussion of the various processes and protocols used to obtain doses to the isocentre of a beam in a phantom utilizing the Farmer-type IC. Moreover, it included all modeling techniques using the Minitab Statistical tool v18.1, vb.net codes and C++ programming language, and provided limitations for the study. Finally, the chapter provided a description of methods used to evaluate the transit dosimetry model obtained in this study.

In Chapter Four, the relationship analysis of various parameters affecting EPID signal values were exhibited in tables and graphical representations. These parameters were seen to affect the functionality of the EPIDs by affecting the grey scale EPID signal values during image acquisition. Various correction factors were therefore implemented to address the effects. The chapter further outlined all the modelled equations obtained in this study using Minitab and MedCalc tools. These modeled equations were later remodeled into a unique equation for onward processing into a GUI application through C++ programming tool. The resulting GUI based design software portrayed the transit dosimetry model of this study. The developed model proved to satisfy radiotherapy accuracy requirements, after it had been subjected to evaluations using an anthropomorphic phantom.

## Conclusions

In conclusion, a simple transit dosimetry model which was fast, adequate and accurate to be employed in clinical routine was developed. The study comprised four investigations: dosimetric response of EPID signal with changing radiation field sizes, dosimetric response of EPID signal with varying delivered doses, dosimetric response of EPID signal with varying absorber thicknesses, and the dosimetric effect of the therapeutic table on EPID signal. For every investigation, appropriate correction factor was obtained to address certain dosimetric consequences for EPID signal.

The radiation field size correction was implemented to compensate for varying field size effect on dose distribution and EPID pixel values. The absorbent patient thickness was introduced as a solution to correct for effect of scatter resulting from patient thickness on EPID pixel values. The treatment couch correction factor was introduced to account for dose perturbation by the treatment couch.

The conversion model developed in this study offered satisfying results for square defined fields in real-time treatment of tissue–mimicking phantom (anthropomorphic phantom). A comparison of absorbed dose measurements between the developed model and TLDs indicated a maximum deviation of 3.93%. The calculated absorbed doses from the Dose Conversion Model were in concurrence with TLD measurements within ±5%, of the prescribed IAEA reference level. The model presented satisfied the accuracy requirements for clinical use. It could be concluded that the developed model was able to correctly verify doses at isocentre during real-time radiotherapy treatments.

**Recommendations**

This study had few limitations, which included the limited application of the dose conversion model to only treatments with SAD technique. Further study is recommended in other radiotherapy treatment techniques such as SSD technique.

The model is also recommended to radiation therapists and medical physicist to be employed in daily clinical routine works, as several tests were used to validate the model in order to be clinically applicable, simple and requiring less time to execute.

Radiotherapy facilities are also encouraged to acquire and implement the dose conversion software (PokooDose), so as to help verify real-time doses to patients.

## REFERENCES

Agarwal, A., Rastogi, N., Maria Das, K. J., Yoganathan, S. A., Udayakumar, D., & Kumar, S. (2017). Investigating the Electronic Portal Imaging Device for Small Radiation Field Measurements. *Journal of Medical Physics*, *42*(2), 59–64. https://doi.org/10.4103/jmp.JMP_131_16

Alaei, P. (2008). Introduction to Health Physics: Fourth Edition. In *Medical Physics* (35). https://doi.org/10.1118/1.3021454

American Cancer Society. (2007). Cancer facts and figures 2007. *American Cancer Society*, 1–52. Retrieved from http://www.cancer.org/acs/groups/content/@nho/documents/document/caff2007pwsecuredpdf.pdf

Baily, N. A., Morton, R. J., Moyer, R. F., Wootton, P., Wright, K. A., & Jones, D. (1994). Physical aspects of quality physical aspects of quality assurance in radiation therapy Consultants. Report 13. *Medical Physics*, (13).

Barbosa, J. C. (2003). What is Mathematical Modelling? *Mathematical Modelling*, 227–234. https://doi.org/10.1533/9780857099549.5.227

Barrett, A., Dobbs, J., Morris, S., & Roques, T. (2009). *Practical radiotherapy planning.* (4th Edition). Hodder Arnold company.

Baskar, R., Lee, K. A., Yeo, R., & Yeoh, K. W. (2012, February 27). Cancer and radiation therapy: Current advances and future directions. *International Journal of Medical Sciences*, *9*, 193–199. https://doi.org/10.7150/ijms.3635

Boellaard, R., van Herk, M., & Mijnheer, B. J. (1996). The dose response

relationship of a liquid-filled electronic portal imaging device. *Medical Physics*, *23*(9), 1601–1611. https://doi.org/10.1118/1.597828

Boellaard, R., van Herk, M., & Mijnheer, B. J. (1997). A convolution model to convert transmission dose images to exit dose distributions. *Medical Physics*, *24*(2), 189–199. https://doi.org/10.1118/1.598066

Bogdanich, W. (2010). Radiation Offers New Cures, and Ways to Do Harm - The New York Times. Retrieved August 19, 2017, from https://www.nytimes.com/2010/01/24/health/24radiation.html

British Broadcasting Corporation. (2016). Cancer patient given radiation overdose at Edinburgh hospital - BBC News. Retrieved May 11, 2020, from https://www.bbc.com/news/uk-scotland-edinburgh-east-fife-36748087

Charles, P. H. (2014). Very Small Field Dosimety. *Queensland University of Technology*, 84–90.

Cherry, P., & Duxbury, A. (2009). *Practical radiotherapy : physics and equipment*. Retrieved from https://www.wiley.com/en-gh/Practical+Radiotherapy:+Physics+and+Equipment,+2nd+Edition-p-9781444316186

Crook, J. M., Raymond, Y., Salhani, D., Yang, H., & Esche, B. (1995). Prostate motion during standard radiotherapy as assessed by fiducial markers. *Radiotherapy and Oncology*, *37*(1), 35–42. https://doi.org/10.1016/0167-8140(95)01613-L

Derreumaux, S., Etard, C., Huet, C., Trompier, F., Clairand, I., Bottollier-Depois, J.-F., Gourmelon, P. (2008). Lessons from recent accidents in

radiation therapy in France. *Radiation Protection Dosimetry*, *131*(1), 130–135. https://doi.org/10.1093/rpd/ncn235

Dina Abdelaziz, Wafaa Khalifa, N. E. S. (2015). Efficacy of Use of A-Si EPID as Imaging Device in IMRT QA. *IOSR Journal of Applied Physics*, *7*(1), 27–43. https://doi.org/10.9790/4861-07132743

Dokholyan, N. V, Noel, J., & Onuchic, J. (2012). Radiation Physics for Medical Physicists by Ervin B. Podgorsak 2nd Edition 2010. In *Computational Modeling of Biological Systems*. https://doi.org/10.1007/978-1-4614-2146-7{_}2

Druck. (2011). GE Druck PACE1000 Precision Pressure Indicator, I1000, I1001, I1002, I1003 on Sale at Test Equipment Depot. Retrieved May 13, 2019, from Druck Limited website: http://www.testequipmentdepot.com/druck/pressure-indicators/pace1000.htm

El-Mohri, Y., Antonuk, L. E., Yorkston, J., Jee, K.-W., Maolinbay, M., Lam, K. L., & Siewerdsen, J. H. (1999). Relative dosimetry using active matrix flat-panel imager (AMFPI) technology. *Medical Physics*, *26*(8), 1530–1541. https://doi.org/10.1118/1.598649

Elekta. (2010a). iViewGT$^{TM}$ Manual. Retrieved August 17, 2018, from https://www.elekta.com/radiotherapy/treatment-solutions/imaging/iviewgt.html

Elekta. (2010b). *iViewGT$^{TM}$ R3.02 - R3.4 Manual*.

Ferlay, J., Colombet, M., Soerjomataram, I., Dyba, T., Randi, G., Bettio, M., Bray, F. (2018). Cancer incidence and mortality patterns in Europe:

Estimates for 40 countries and 25 major cancers in 2018. *European Journal of Cancer (Oxford, England : 1990)*, *0*(0). https://doi.org/10.1016/j.ejca.2018.07.005

Gantchew, M. (2010). Radiotherapy risk profile. *Rentgenologiya i Radiologiya*, *49*(4), 282–285.

Glide-Hurst, C. K., & Chetty, I. J. (2014). Improving radiotherapy planning, delivery accuracy, and normal tissue sparing using cutting edge technologies. *Journal of Thoracic Disease*, *6*, 303–318. https://doi.org/10.3978/j.issn.2072-1439.2013.11.10

Gonzalez-Lopez, A., Vera-Sanchez, J.-A., & Lago-Martin, J.-D. (2015). Small fields measurements with radiochromic films. *Journal of Medical Physics*, *40*(2), 61–67. https://doi.org/10.4103/0971-6203.158667

Greer, P. B., & Popescu, C. C. (2003). Dosimetric properties of an amorphous silicon electronic portal imaging device for verification of dynamic intensity modulated radiation therapy. *Medical Physics*, *30*(7), 1618–1627. https://doi.org/10.1118/1.1582469

Grządziel, A., Smolińska, B., Rutkowski, R., & Ślosarek, K. (2007). EPID dosimetry - Configuration and pre-treatment IMRT verification. *Reports of Practical Oncology and Radiotherapy*, *12*(6), 307–312. https://doi.org/10.1016/S1507-1367(10)60069-7

Hansen, V. N., Evans, P. M., & Swindell, W. (1996). The application of transit dosimetry to precision radiotherapy. *Medical Physics*, *23*(5), 713–721. https://doi.org/10.1118/1.597719

Harshaw. (2007). *Harshaw TLD Model 6600 Plus Automated TLD Reader*

*system for whole body , extremity , neutron Harshaw TLD Model 6600 Plus Features and Benefits • Based on proven worldwide*.

Herman, M. G., Balter, J. M., Jaffray, D. A., Mcgee, K. P., Munro, P., Shalev, S., Wong, J. W. (2001). Clinical Use of Electronic Portal Imaging : Report of AAPM Radiation Therapy Committee Task Group 58 AAPM Refresher Course – Salt Lake City July 2001. *Medical Physics*, *28*(5), 712–737. https://doi.org/10.1118/1.1368128

Herman, M. G., Balter, J. M., Jaffray, D. A., McGee, K. P., Munro, P., Shalev, S., Wong, J. W. (2001). Clinical use of electronic portal imaging: Report of AAPM Radiation Therapy Committee Task Group 58. *Medical Physics*, *28*(5), 712–737. https://doi.org/10.1118/1.1368128

Huq, M. S., Fraass, B. A., Dunscombe, P. B., Gibbons, J. P., Ibbott, G. S., Mundt, A. J., Yorke, E. D. (2016, July 1). The report of Task Group 100 of the AAPM: Application of risk analysis methods to radiation therapy quality management. *Medical Physics*, *43(2)*, 4209–4262. https://doi.org/10.1118/1.4947547

Ibrahim, A. G., Mohamed, I. E., & Zidan, H. M. (2018). *Dosimetric Comparison of Amorphous Silicon EPID and 2D Array Detector for Pre-Treatment Verification of Intensity Modulated Radiation Therapy*. 438–452. https://doi.org/10.4236/ijmpcero.2018.74037

International Agency for Research on Cancer. (2014). World cancer report 2014. *World Health Organization*, 1–2. https://doi.org/9283204298

International Atomic Energy Agency. (2000). TRS 398: Absorbed Dose Determination in External Beam Radiotherapy. *International Atomic*

*Energy Agency*, 1–229. https://doi.org/10.1097/00004032-200111000-00017

International Atomic Energy Agency. (2001). Investigation Of An Accidental Exposue Of Radiotherapy Patients In Panama. *IAEA*, (June). Retrieved from http://www-pub.iaea.org/books/IAEABooks/6391/Investigation-of-an-Accidental-Exposure-of-Radiotherapy-Patients-in-Panama

International Atomic Energy Agency. (2005). IAEA-TECDOC-1455 "Implementation of the International Code of Practice on Dosimetry in Radiotherapy ( TRS 398 ): Review of testing" results. *International Atomic Energy Agency*, (June), 101.

International Atomic Energy Agency. (2009). Technical Reports Series No. 469 - Calibration of Reference Dosimeters for External Beam Radiotherapy. *Technical Reports Series No. 469 - Calibration of Reference Dosimeters for External Beam Radiotherapy*, (469), 1–86. Retrieved from http://www.iaea.org/books

International Atomic Energy Agency. (2013). *Development of procedures for in vivo dosimetry in radiotherapy.IAEA Human Health Reports No. 8* (IAEA Human). Retrieved from http://www-pub.iaea.org/MTCD/publications/PDF/Pub1606_web.pdf;http://www.iaea.org/books

Ion Beam Applications. (2013). *Phantoms for Absolute Dosimetry - IBA Dosimetry*. Retrieved from https://www.iba-dosimetry.com/media/1372/rt-br-e-phantoms-for-ad_rev2_0813.pdf

Khan, F. M. (2010). *The physics of radiation therapy*. Lippincott Williams &

Wilkins.

Klein, E. E., Hanley, J., Bayouth, J., Carolina, N., Simon, W., Dresser, S., Holmes, T. (2009). *Task Group 142 report : Quality assurance of medical accelerators* (September), 4197–4212. https://doi.org/10.1118/1.3190392

Kondo M, Y. T. (2018). *How does radiation work to treat cancer ?* 3–9.

Larry, E. A. (2002). *Electronic portal imaging devices : a review and historical perspective of contemporary technologies and research*. *31*.

Lemoigne, Y., & Caner, A. (2007). Radiotherapy and Brachytherapy. In *Igarss 2014*. https://doi.org/10.1017/CBO9781107415324.004

Liauw, S. L., Connell, P. P., & Weichselbaum, R. R. (2013, February 20). New paradigms and future challenges in radiation oncology: An update of biological targets and technology. *Science Translational Medicine*, 5, 173. https://doi.org/10.1126/scitranslmed.3005148

Louwe, R. J. W., Tielenburg, R., Van Ingen, K. M., Mijnheer, B. J., & Van Herk, M. B. (2004). The stability of liquid-filled matrix ionization chamber electronic portal imaging devices for dosimetry purposes. *Medical Physics*, *31*(4), 819–827. https://doi.org/10.1118/1.1668411

Mahmoud Hamdy Abaza, A. (2019). New Trend in Radiation Dosimeters. *American Journal of Modern Physics*, *7*(1), 21. https://doi.org/10.11648/j.ajmp.20180701.13

Malicki, J. (2012). The importance of accurate treatment planning, delivery, and dose verification. *Reports of Practical Oncology and Radiotherapy*, 1*7(2)*, 63–65. https://doi.org/10.1016/j.rpor.2012.02.001

Mans, A., Wendling, M., McDermott, L. N., Sonke, J.-J., Tielenburg, R., Vijlbrief, R., Stroom, J. C. (2010). Catching errors with *in vivo* EPID dosimetry. *Medical Physics*, *37*(6Part2), 2638–2644. https://doi.org/10.1118/1.3397807

Marion, G., Scotland, S., Lawson, D., & Marion, G. (2008). *MathModeling_book*.

Mayles, P., Nahum, A., & Rosenwald, J. C. (2007). *Handbook of Radiotherapy Physics: Theory and Practice*. https://doi.org/10.15713/ins.mmj.3

Mayo. (2018). Intensity-modulated radiation therapy (IMRT) - Mayo Clinic. Retrieved July 1, 2019, from https://www.mayoclinic.org/tests-procedures/intensity-modulated-radiation-therapy/about/pac-20385147

MediTron. (2012). *Virtually Human Male Pelvis Phantom*. 800–801.

Mehta, S. R., Suhag, V., Semwal, M., & Sharma, N. (2010). Radiotherapy: Basic Concepts and Recent Advances. *Medical Journal, Armed Forces India*, *66*(2), 158–162. https://doi.org/10.1016/S0377-1237(10)80132-7

Menzel, H. G. (2010). The international commission on radiation units and measurements. *Journal of the ICRU*, *10*(2), 1–35. https://doi.org/10.1093/jicru/ndq025

Ministy of Health. (2016). National Strategy for Cancer. *Ministry of Health, Ghana*, 1–8.

Mohammadi, M., & Bezak, E. (2005). The physical characteristics of a SLIC-EPID for transmitted dosimetry. *Iranian Journal of Radiation Research*, *2*(4), 175–183.

Morton, E. J., Swindell, W., Lewis, D. G., & Evans, P. M. (1991). A linear array, scintillation crystal-photodiode detector for megavoltage imaging. *Medical Physics*, *18*(4), 681–691. https://doi.org/10.1118/1.596661

Mould, R. F. (Richard F. (1993). *A century of x-rays and radioactivity in medicine : with emphasis on photographic records of the early years*. Institute of Physics Pub.

Munro, P., & Bouius, D. C. (1998). X-ray quantum limited portal imaging using amorphous silicon flat-panel arrays. *Medical Physics*, *25*(5), 689–702. https://doi.org/10.1118/1.598252

Nakano, T., Eckford, A. W., & Haraguchi, T. (2013). Mathematical modeling and simulation. *Molecular Communication*, 71–96. https://doi.org/10.1017/cbo9781139149693.006

Nijsten, S. (2009). Portal Dosimetry in Radiotherapy. *Economic Journal - ECON J*, 172–178. https://doi.org/10.1016/S0167-8140(12)72719-6

OzRadOnc. (2017a). Phantoms. Retrieved July 7, 2019, from http://ozradonc.wikidot.com/phantoms

OzRadOnc. (2017b). Thermoluminescent Dosimeters - OzRadOnc. Retrieved July 7, 2019, from http://ozradonc.wikidot.com/thermoluminescent-dosimeters

Pai, S., Das, I. J., Dempsey, J. F., Lam, K. L., LoSasso, T. J., Olch, A. J., Wilcox, E. E. (2007). TG-69: Radiographic film for megavoltage beam dosimetry. *Medical Physics*, 34, 2228–2258. https://doi.org/10.1118/1.2736779

Pasma, K. L., Dirkx, M. L. P., Kroonwijk, M., Visser, A. G., & Heijmen, B. J.

M. (1999). Dosimetric verification of intensity modulated beams produced with dynamic multileaf collimation using an electronic portal imaging device. *Medical Physics*, *26*(11), 2373–2378. https://doi.org/10.1118/1.598752

Physikalisch - Technische Werkstätten. (2016a). PTW: Acrylic and RW3 Slab Phantoms. Retrieved August 18, 2018, from https://www.ptw.de/acrylic_and_rw3_slab_phantoms0.html

Physikalisch - Technische Werkstätten. (2016b). *User Manual Farmer Chamber Ionization Chamber*. 1–42.

Plummer, M., de Martel, C., Vignat, J., Ferlay, J., Bray, F., & Franceschi, S. (2016). Global burden of cancers attributable to infections in 2012: a synthetic analysis. *The Lancet Global Health*, *4*(9), e609–e616. https://doi.org/10.1016/S2214-109X(16)30143-7

Podgorsak, E. B. (2005). *Review of Radiation Oncology Physics: A Handbook for Teachers and Students*. 133–178. Retrieved from https://pdfs.semanticscholar.org/23f7/64a7b034c008830eb0a9c4e362d4ef58a678.pdf

Reynolds, L. A., & Tansey, E. M. (2006). *Development of physics applied to medicine in the UK, 1945-1990 : the transcript of a Witness Seminar held by the Wellcome Trust Centre for the History of Medicine at UCL, London, on 5 July 2005*. Wellcome Trust Centre for the History of Medicine at UCL.

Rottmann, J., Morf, D., Fueglistaller, R., Zentai, G., Star-Lack, J., & Berbeco, R. (2016). A novel EPID design for enhanced contrast and detective

quantum efficiency. *Physics in Medicine and Biology*, *61*(17), 6297–6306. https://doi.org/10.1088/0031-9155/61/17/6297

Rush, S. C. (2014). Practical Radiotherapy Planning. 2nd ed. *Radiology*, *185*(1), 52–52. https://doi.org/10.1148/radiology.185.1.52

Seng, B. L. (2008). *2-D Dose Measurement Using a Flat Panel Epid*. University of British Columbia.

Slosarek, K., Szlag, M., Bekman, B., & Grzadziel, A. (2010). EPID in vivo dosimetry in RapidArc technique. *Reports of Practical Oncology and Radiotherapy*, *15*(1), 8–14. https://doi.org/10.1016/j.rpor.2010.01.003

Smallwood, R. H., Lawford, P. V, & Hose, D. R. (1999). Medical Physics and Biomedical Engineering. *IOP Publishing Ltd*.

Tateoka, K., Ouchi, A., Waka, M., Nakata, K., Nagase, D., Shimizume, K., Hareyama, M. (2006). Dosimetric properties of the liquid ionization chamber electronic portal imaging device (EPID). *Igaku Butsuri : Nihon Igaku Butsuri Gakkai Kikanshi = Japanese Journal of Medical Physics : An Official Journal of Japan Society of Medical Physics*, *26*(1), 28–38. Retrieved from http://www.ncbi.nlm.nih.gov/pubmed/16788287

Taylor, A., & Powell, M. E. B. (2004). Intensity-modulated radiotherapy--what is it? *Cancer Imaging : The Official Publication of the International Cancer Imaging Society*, *4*(2), 68–73. https://doi.org/10.1102/1470-7330.2004.0003

Testo. (2017). Testo 925 (0560 9250) 1-Channel Type K Thermometer - at the Test Equipment Depot. Retrieved May 14, 2019, from http://www.testequipmentdepot.com/testo/thermometers-and-humidity-

meters/temperature-meters/1-channel-type-k-thermometer-925.htm

Thwaites, D. I., & Tuohy, J. B. (2006). Back to the future: the history and development of the clinical linear accelerator. *Physics in Medicine and Biology*, *51*(13), R343–R362. https://doi.org/10.1088/0031-9155/51/13/R20

Torre, L. A., Bray, F., Siegel, R. L., Ferlay, J., Lortet-Tieulent, J., & Jemal, A. (2015). Global cancer statistics, 2012. *CA: A Cancer Journal for Clinicians*, *65*(2), 87–108. https://doi.org/10.3322/caac.21262

van Elmpt, W., McDermott, L., Nijsten, S., Wendling, M., Lambin, P., & Mijnheer, B. (2008). A literature review of electronic portal imaging for radiotherapy dosimetry. *Radiotherapy and Oncology*, *88*(3), 289–309. https://doi.org/10.1016/j.radonc.2008.07.008

van Herk, M. (1991). Physical aspects of a liquid-filled ionization chamber with pulsed polarizing voltage. *Medical Physics*, *18*(4), 692–702. https://doi.org/10.1118/1.596662

Wambersie, A., Zoetelief, J., Menzel, H. G., & Paretzke, H. (2005). The ICRU (International Commission on Radiation Units and Measurements): its contribution to dosimetry in diagnostic and interventional radiology. *Radiation Protection Dosimetry*, *117*(1–3), 7–12. https://doi.org/10.1093/rpd/nci701

Wendling, M., Louwe, R. J. W., McDermott, L. N., Sonke, J. J., Van Herk, M., & Mijnheer, B. J. (2006). Accurate two-dimensional IMRT verification using a back-projection EPID dosimetry method. *Medical Physics*, *33*(2), 259–273. https://doi.org/10.1118/1.2147744

Wikipedia. (2017). Graphical user interface. *ScienceDaily*. Retrieved from https://www.sciencedaily.com/terms/graphical_user_interface.htm

Williams, J. R. (Jerry R. ., & Thwaites, D. I. (2000). *Radiotherapy physics-in practice*. Oxford University Press.

Williamson, G. F. (2014). *Intraoral_Radiography_Positioning_and_Radiation_Pr.pdf.crdownload*. *PennWell*, (January 2006), 3–9.

World Health Organization. (2008). *Radiotherapy Risk Profile: Technical Manual*.

Woźniak, B., Ganowicz, M., Bekman, A., & Maniakowski, Z. (2005). *A comparison of the dosimetric properties of The Electronic Portal Imaging Devices ( EPIDs ) LC250 and aS500*. *10*(5), 249–254. https://doi.org/10.1016/S1507-1367(05)71097-X

# APPENDICES

## APPENDIX A: C++ AND VB.NET CODES USED FOR GUI GENERATION IN THIS STUDY.

```
Public Class modelling

    Private Sub modelling_Load(ByVal sender As System.Object, ByVal e As
System.EventArgs) Handles MyBase.Load

    End Sub

    Private Sub txtdplanned_KeyPress(ByVal sender As Object, ByVal e As
System.Windows.Forms.KeyPressEventArgs) Handles txtdplanned.KeyPress

    End Sub

    Private Sub txtdplanned_TextChanged(ByVal sender As System.Object,
ByVal e As System.EventArgs) Handles txtdplanned.TextChanged

        Dim d_planned
        Dim fs
        Dim d_measured
        Dim cf_couch
        Dim cf_epid_sensitivity
        Dim T_patient
        Dim S_epid

        d_planned = Val(txtdplanned.Text)
        fs = Val(txtfs.Text)
        cf_couch = Val(txtcfcouch.Text)
        cf_epid_sensitivity = Val(txtcfepidsensitivity.Text)
```

```
        T_patient = Val(txttpatient.Text)
        S_epid = Val(txtsepid.Text)

        d_measured = (-8794 + (0.3356 * S_epid)) * (0.7362 + (0.03604 * fs) - (0.000977 * fs ^ 2)) * (0.9652 + (0.00647 * T_patient)) * (0.3168 + (0.1881 * d_planned) - (0.01803 * d_planned ^ 2) + (0.000457 * d_planned ^ 3)) * cf_epid_sensitivity * cf_couch
        txtdmeasured.Text = d_measured
    End Sub
    Private Sub txtfs_KeyPress(ByVal sender As Object, ByVal e As System.Windows.Forms.KeyPressEventArgs) Handles txtfs.KeyPress
     End Sub
    Private Sub txtfs_TextChanged(ByVal sender As System.Object, ByVal e As System.EventArgs) Handles txtfs.TextChanged
        Dim d_planned
        Dim fs
        Dim d_measured
        Dim cf_couch
        Dim cf_epid_sensitivity
        Dim T_patient
        Dim S_epid
        d_planned = Val(txtdplanned.Text)
        fs = Val(txtfs.Text)
        cf_couch = Val(txtcfcouch.Text)
        cf_epid_sensitivity = Val(txtcfepidsensitivity.Text)
        T_patient = Val(txttpatient.Text)
        S_epid = Val(txtsepid.Text)
        d_measured = (-8794 + (0.3356 * S_epid)) * (0.7362 + (0.03604 * fs) - (0.000977 * fs ^ 2)) * (0.9652 + (0.00647 * T_patient)) * (0.3168 + (0.1881 * d_planned) - (0.01803 * d_planned ^ 2) + (0.000457 * d_planned ^ 3)) * cf_epid_sensitivity * cf_couch
```

```
        txtdmeasured.Text = d_measured
    End Sub
    Private Sub txtcfcouch_KeyPress(ByVal sender As Object, ByVal e As
System.Windows.Forms.KeyPressEventArgs) Handles txtcfcouch.KeyPress
     End Sub
    Private Sub txtcouch_TextChanged(ByVal sender As System.Object, ByVal
e As System.EventArgs) Handles txtcfcouch.TextChanged
        Dim d_planned
        Dim fs
        Dim d_measured
        Dim cf_couch
        Dim cf_epid_sensitivity
        Dim T_patient
        Dim S_epid
        d_planned = Val(txtdplanned.Text)
        fs = Val(txtfs.Text)
        cf_couch = Val(txtcfcouch.Text)
        cf_epid_sensitivity = Val(txtcfepidsensitivity.Text)
        T_patient = Val(txttpatient.Text)
        S_epid = Val(txtsepid.Text)
        d_measured = (-8794 + (0.3356 * S_epid)) * (0.7362 + (0.03604 * fs) -
(0.000977 * fs ^ 2)) * (0.9652 + (0.00647 * T_patient)) * (0.3168 + (0.1881 *
d_planned) - (0.01803 * d_planned ^ 2) + (0.000457 * d_planned ^ 3)) *
cf_epid_sensitivity * cf_couch
        txtdmeasured.Text = d_measured
    End Sub
    Private Sub txtsepid_KeyPress(ByVal sender As Object, ByVal e As
System.Windows.Forms.KeyPressEventArgs) Handles txtsepid.KeyPress

    End Sub
```

```
    Private Sub txtsepid_TextChanged(ByVal sender As System.Object, ByVal
e As System.EventArgs) Handles txtsepid.TextChanged
        Dim d_planned
        Dim fs
        Dim d_measured
        Dim cf_couch
        Dim cf_epid_sensitivity
        Dim T_patient
        Dim S_epid

        d_planned = Val(txtdplanned.Text)
        fs = Val(txtfs.Text)
        cf_couch = Val(txtcfcouch.Text)
        cf_epid_sensitivity = Val(txtcfepidsensitivity.Text)
        T_patient = Val(txttpatient.Text)
        S_epid = Val(txtsepid.Text)

        d_measured = (-8794 + (0.3356 * S_epid)) * (0.7362 + (0.03604 * fs) -
(0.000977 * fs ^ 2)) * (0.9652 + (0.00647 * T_patient)) * (0.3168 + (0.1881 *
d_planned) - (0.01803 * d_planned ^ 2) + (0.000457 * d_planned ^ 3)) *
cf_epid_sensitivity * cf_couch
        txtdmeasured.Text = d_measured

    End Sub

    Private Sub txttpatient_KeyPress(ByVal sender As Object, ByVal e As
System.Windows.Forms.KeyPressEventArgs) Handles txttpatient.KeyPress

    End Sub
```

```
    Private Sub txttpatient_TextChanged(ByVal sender As System.Object,
ByVal e As System.EventArgs) Handles txttpatient.TextChanged
        Dim d_planned
        Dim fs
        Dim d_measured
        Dim cf_couch
        Dim cf_epid_sensitivity
        Dim T_patient
        Dim S_epid

        d_planned = Val(txtdplanned.Text)
        fs = Val(txtfs.Text)
        cf_couch = Val(txtcfcouch.Text)
        cf_epid_sensitivity = Val(txtcfepidsensitivity.Text)
        T_patient = Val(txttpatient.Text)
        S_epid = Val(txtsepid.Text)

        d_measured = (-8794 + (0.3356 * S_epid)) * (0.7362 + (0.03604 * fs) -
(0.000977 * fs ^ 2)) * (0.9652 + (0.00647 * T_patient)) * (0.3168 + (0.1881 *
d_planned) - (0.01803 * d_planned ^ 2) + (0.000457 * d_planned ^ 3)) *
cf_epid_sensitivity * cf_couch
        txtdmeasured.Text = d_measured

    End Sub

    Private Sub txtcfepidsensitivity_KeyPress(ByVal sender As Object, ByVal
e As System.Windows.Forms.KeyPressEventArgs) Handles
txtcfepidsensitivity.KeyPress

    End Sub
```

```
    Private Sub txtcfepidsensitivity_TextChanged(ByVal sender As
System.Object, ByVal e As System.EventArgs) Handles
txtcfepidsensitivity.TextChanged
        Dim d_planned
        Dim fs
        Dim d_measured
        Dim cf_couch
        Dim cf_epid_sensitivity
        Dim T_patient
        Dim S_epid
        d_planned = Val(txtdplanned.Text)
        fs = Val(txtfs.Text)
        cf_couch = Val(txtcfcouch.Text)
        cf_epid_sensitivity = Val(txtcfepidsensitivity.Text)
        T_patient = Val(txttpatient.Text)
        S_epid = Val(txtsepid.Text)

        d_measured = (-8794 + (0.3356 * S_epid)) * (0.7362 + (0.03604 * fs) -
(0.000977 * fs ^ 2)) * (0.9652 + (0.00647 * T_patient)) * (0.3168 + (0.1881 *
d_planned) - (0.01803 * d_planned ^ 2) + (0.000457 * d_planned ^ 3)) *
cf_epid_sensitivity * cf_couch
        txtdmeasured.Text = d_measured

    End Sub

    Private Sub GroupBox1_Enter(ByVal sender As System.Object, ByVal e
As System.EventArgs) Handles GroupBox1.Enter

    End Sub
End Class
```

# APPENDIX B

## APPENDIX B-1: TREATMENT PLAN WITH BEAM ARRANGEMENTS AND DOSE DISTRIBUTIONS TO DELIVER A DOSE OF 1.8 GY AT THE ISOCENTRE OF THE BEAM.

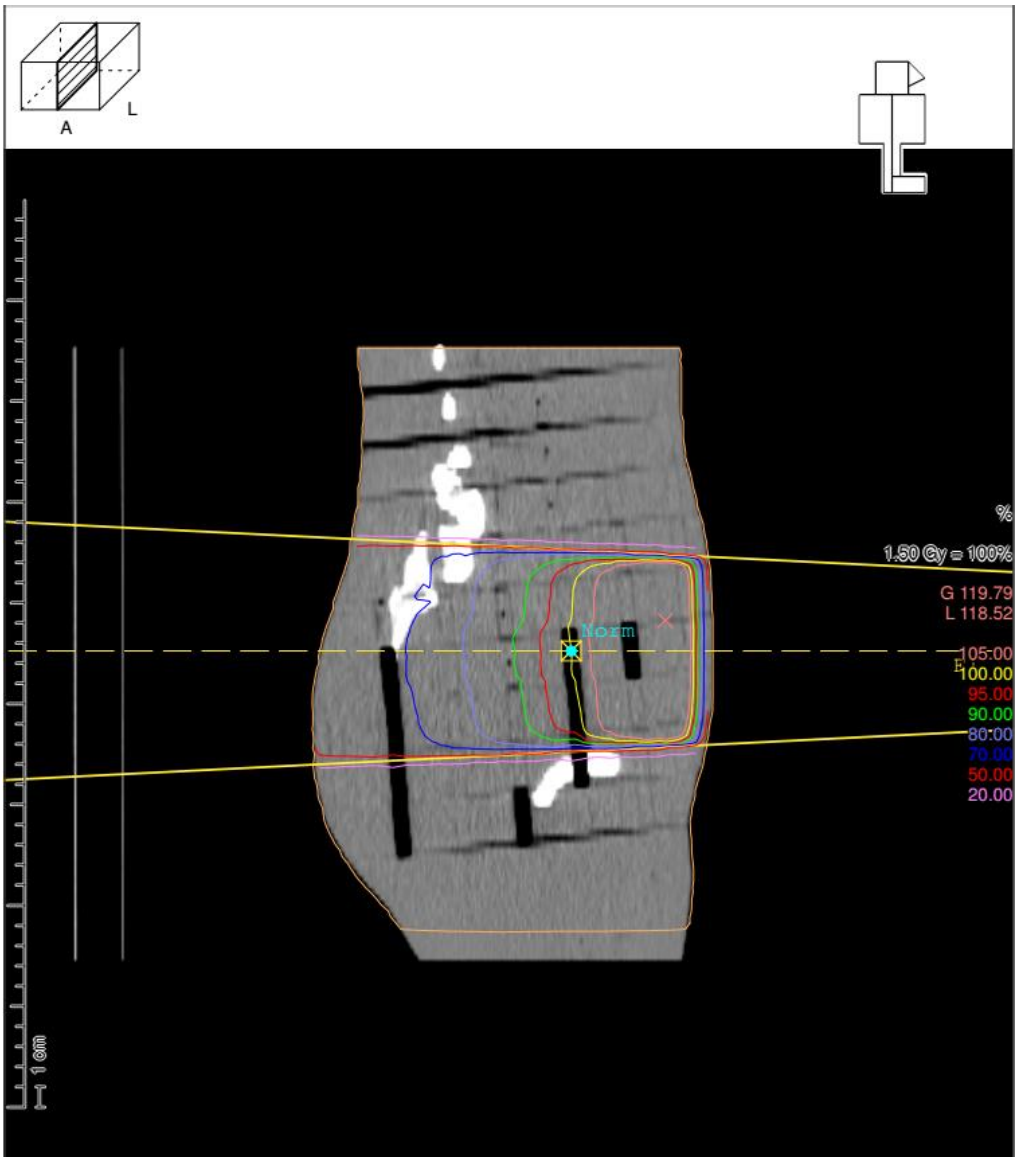

APPENDIX B-2: TREATMENT PLAN WITH BEAM ARRANGEMENTS AND DOSE DISTRIBUTIONS TO DELIVER A DOSE OF 1.2 GY AT THE ISOCENTRE OF THE BEAM.

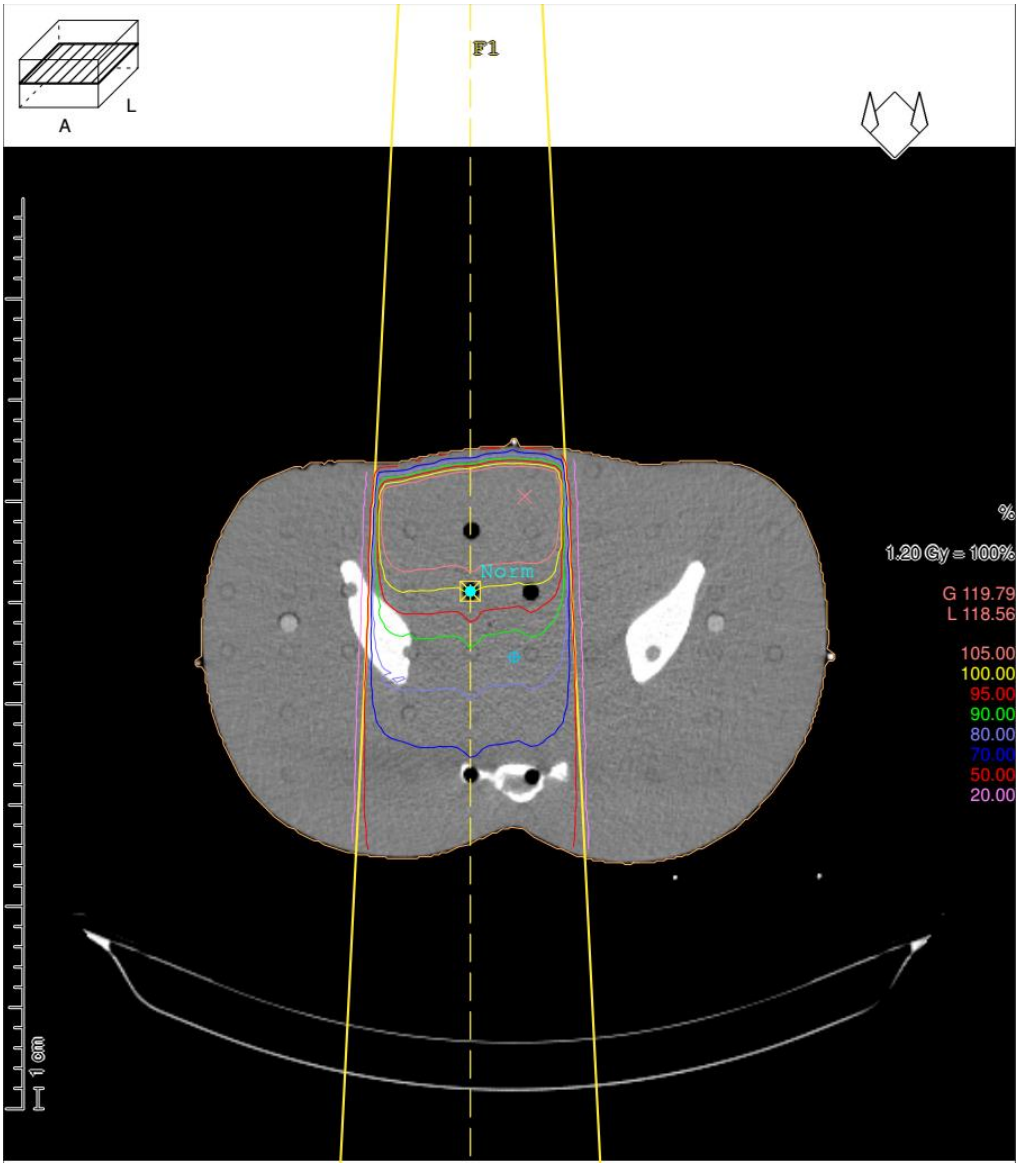

APPENDIX B-3: TREATMENT PLAN WITH BEAM ARRANGEMENTS AND DOSE DISTRIBUTIONS TO DELIVER A DOSE OF 1.0 GY AT THE ISOCENTRE OF THE BEAM.

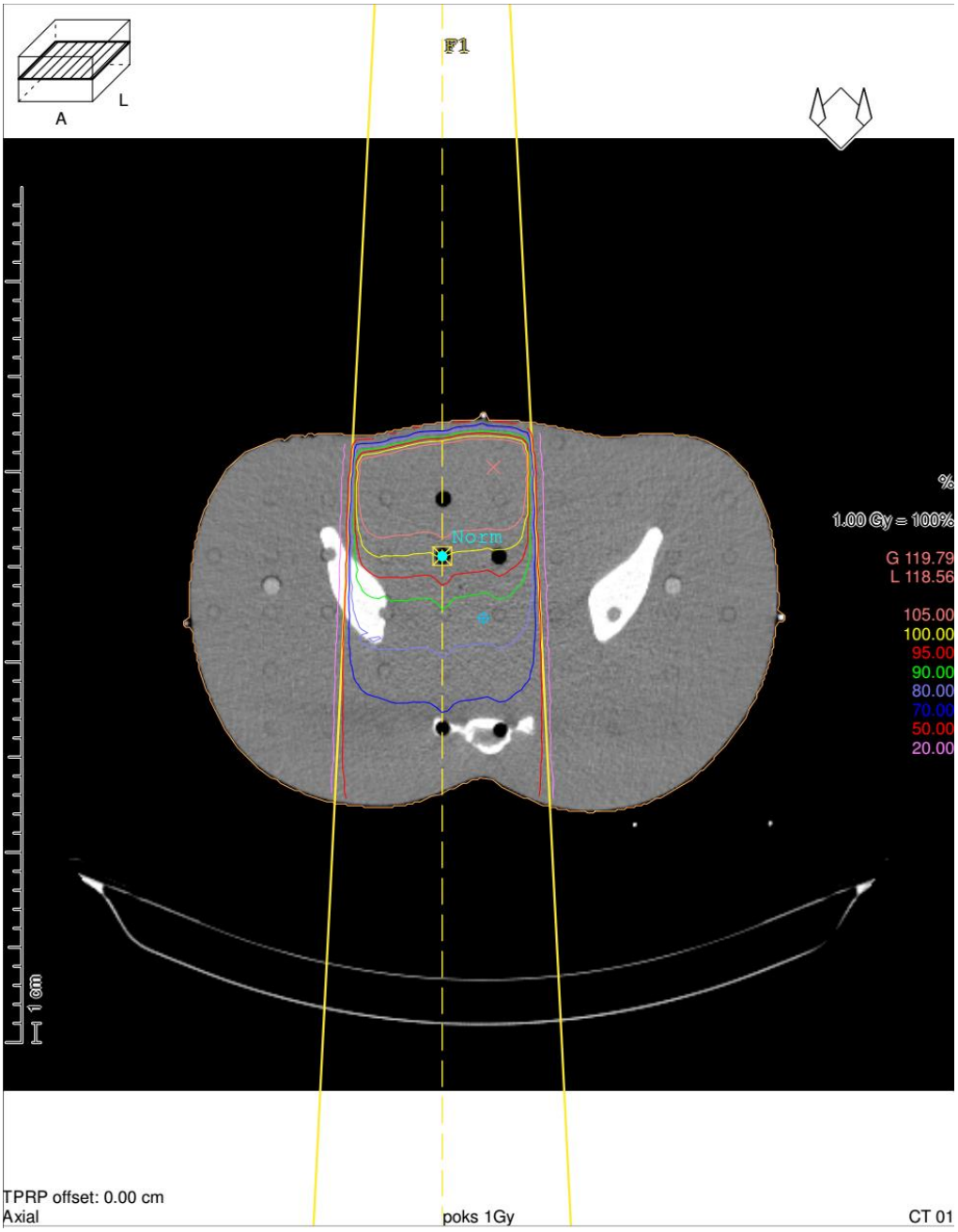

APPENDIX B-4: TREATMENT PLAN WITH BEAM ARRANGEMENTS AND DOSE DISTRIBUTIONS TO DELIVER A DOSE OF 2.0 GY AT THE ISOCENTRE OF THE BEAM.

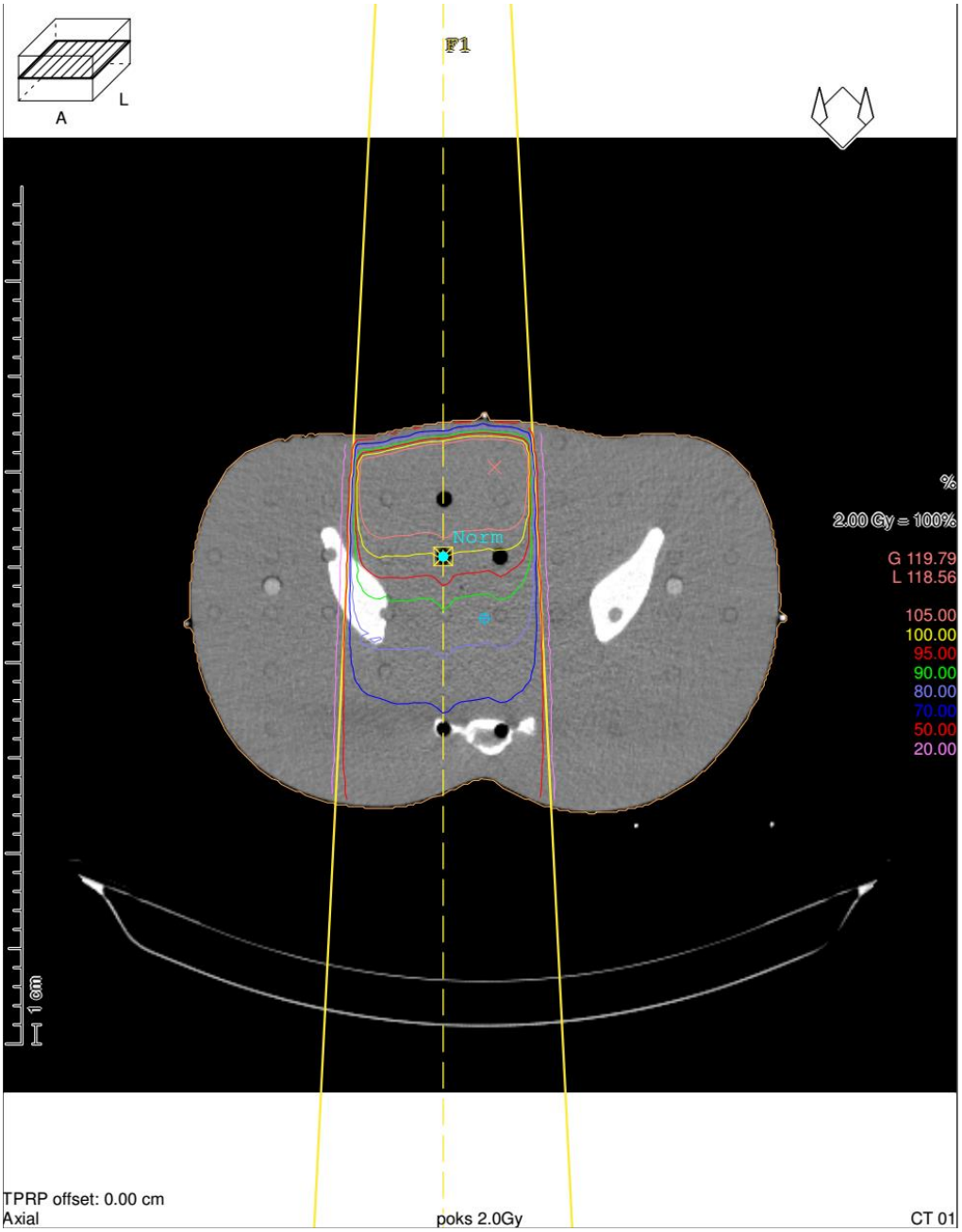

APPENDIX C: TREATMENT PLAN OBTAINED IN THIS STUDY WITH BEAM ARRANGEMENTS TO DELIVER A DOSE AT THE ISOCENTRE OF THE BEAM IN THE PMMA PHANTOM SLABS.

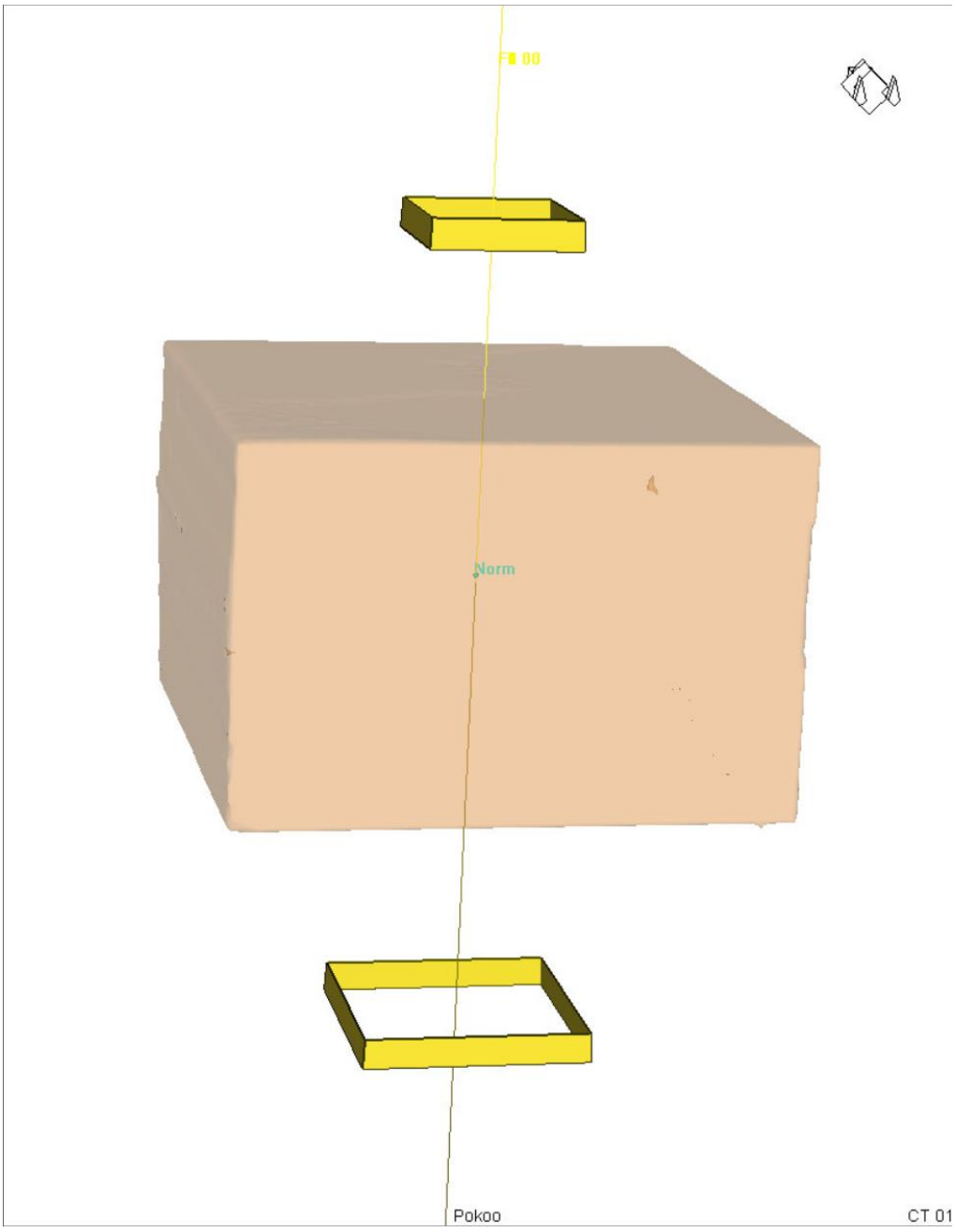

PEER REVIEWED ARTICLE FROM THESIS

Pokoo-Aikins, M., Kyere, A. K., Eghan, M. J., Samuel, N., Kyeremeh, P. O., Acquah, G. F., & Hasford, F. (2019). A Study on Amorphous Silicon Electronic Portal Imaging Device (ASi EPID) Response to Delivered Radiation Doses. *International Journal of Sciences: Basic and Applied Research (IJSBAR) ISSN*, *48*(4), 66–73.